Scholars' Mine

Spring 2019

Techno-economic optimization and environmental life cycle assessment of microgrids using genetic algorithm and artificial neural networks

Prashant Nagapurkar

Follow this and additional works at: https://scholarsmine.mst.edu/doctoral_dissertations

Part of the Chemical Engineering Commons

Department: Chemical and Biochemical Engineering

TECHNO-ECONOMIC OPTIMIZATION AND ENVIRONMENTAL LIFE

CYCLE ASSESSMENT OF MICROGRIDS USING GENETIC ALGORITHM

AND

ARTIFICIAL NEURAL NETWORKS

by

PRASHANT SURESH NAGAPURKAR

A DISSERTATION

Presented to the Faculty of the Graduate School of the

MISSOURI UNIVERSITY OF SCIENCE AND TECHNOLOGY

In Partial Fulfillment of the Requirements for the Degree

DOCTOR OF PHILOSOPHY

in

CHEMICAL ENGINEERING

2019

Approved by:

Joseph Smith, Advisor
Douglas Ludlow
Christi Luks
Dipak Barua
Gregory Gelles

PUBLICATION DISSERTATION OPTION

This dissertation consists of following four manuscripts, formatted in the style used by Missouri University of Science and Technology

Paper I: Pages 4-60 have been published in 'Energy Conversion and Management', an Elsevier Publication.

Paper II: Pages 61-117 have been submitted to 'Journal of Cleaner Production', an Elsevier Publication.

Paper III: Pages 118-169 are intended for submission to 'Journal of Supercritical fluids', an Elsevier Publication.

Paper IV: Pages 170-191 have been published in '2015 International System Dynamics Conference Proceedings'.

Paper V: Pages 192-211 have been published in '2017 International Conference on Environmental Impacts of the Oil and Gas Industries: Kurdistan Region of Iraq as a Case Study (EIOGI)', IEEE Explore Publication.

ABSTRACT

This dissertation focuses primarily on techno-economic optimization and environmental life cycle assessment (LCA) of sustainable energy generation technologies. This work is divided into five papers. The first paper discusses the techno-economic optimization and environmental life cycle assessment of microgrids located in the USA using genetic algorithm. In this paper, a methodology was developed that assessed the techno-economic and environmental performance of a small scale microgrid located in US cities of Tucson, Lubbock and Dickinson. Providing uninterrupted power the microgrid was composed of seven components - solar photovoltaics, wind-turbines, lead acid batteries, biodiesel generators, fuel cells, electrolyzers and H_2 tanks. The second paper is an extension of first paper and utilizes Artificial Neural Networks to predict energy demand while also incorporating social costs. With an aim to incorporate LCA methodology, the third paper discusses the upstream biodiesel production process which is a vital fuel source for the microgrid. In this paper, a supercritical biodiesel production process from waste cooking oil (WCO) using methanol in the presence of propane as a co-solvent was technically analyzed using Aspen Plus software. In the fourth paper, a system dynamics model of the cast iron foundry process was developed and validated with the actual energy consumption data based on which recommendations were made to reduce energy consumption by 26% or $2.6 million. In the fifth paper, an assessment of the threats to the aquatic resources due to rapid growth in the extraction of Shale gas in the US was performed with an application to the Kurdistan region of Iraq.

ACKNOWLEDGMENTS

First and foremost, I would like to express my deepest gratitude to my advisor Dr. Joseph Smith for his research guidance throughout my PhD studies. I am also thankful to my committee members for their valuable research inputs that has helped me shape my work. I appreciate the financial support provided by department of Chemical and Biochemical Engineering, Wayne and Gayle Laufer endowment fund and Caterpillar Inc.

I will be eternally grateful to my family. Without their support and encouragement, this work would not have been possible. My mom, dad, brother and my wife have always provided me with unwavering and unconditional moral support. This dissertation has been wholeheartedly dedicated to them.

My friends also played a vital role in the completion of this work. Specifically, Anand, Vivek, Shyam, Haider, Hassan, Jia, Aso, Jeremy, Ashish and Ajinkya. I am also grateful to Eileen and Frieda for assisting me with preparation of manuscripts. Finally, I would like to thank Chemical Engineering department's staff members – Emily, Marlene and Krista for their administrative assistance.

TABLE OF CONTENTS

LIST OF ILLUSTRATIONS

PAPER III

PAPER IV

PAPER V

LIST OF TABLES

PAPER III

NOMENCLATURE

Symbol   Description

LCOE   Levelized cost of electricity ($/kWh)

LCA   Life cycle assessment (LCA)

1. INTRODUCTION

The world is heavily reliant on conventional fossil fuel sources such as coal, natural gas, etc. to fulfill its energy demand. 80% of the total energy demand in 2015 has been met through fossils fuels [1]. They have been historically utilized to generated energy due to their high density and cheap cost. In the recent decades, fossil fuels have also assisted in the rapid industrialization and improvement in the human quality of life. Despite these advantages, there are also some downsides of utilizing fossil fuels. For instance, combustion of fossil fuels results in emission of greenhouse gases such as carbon dioxide and methane that negatively affect the environment. Furthermore, these fuels are finite in nature and have been one of the main reasons behind the geopolitical tensions caused between exporting and importing countries.

Harnessing energy from renewable energy sources such as solar, wind, hydro, etc. have been proposed as one of the solutions to the above problems caused due to fossil fuels. Renewable energy sources can produce power without adversely affecting the environment. The dependence on foreign countries in order to meet the domestic energy demand can also be reduced by utilizing these renewable sources.

1.1. RESEARCH MOTIVATION

Despite their clean method of power generation, one of the main challenges of renewable energy sources which hinders their widespread acceptance and commercialization is their intermittent nature of power production. For instance, solar photovoltaics cannot provide power during night time. This challenge can be addressed by integrating together different renewable sources in an entity called as 'microgrid'.

Prior studies have showed this approach to be effective as it increases the system reliability and efficiency [2]. Microgrids have also been shown to generate power at a cheaper cost than those systems which employ only a single renewable source [3]. Furthermore, for remote and off grid communities, microgrids can also serve as an economically superior option than procuring power from a conventional electric grid [4].

The key driver of the widespread implementation of microgrids is its economic feasibility. An environmental friendly technology which has low carbon footprint would be difficult to finance. Therefore, in this work a methodology has been developed that tackles mono-optimization problem that identifies a microgrid configuration (solar photovoltaic capacity, wind turbine capacity, etc.) that has the lowest generation cost of electricity, LCOE ($/kWh). Realizing that the evaluation of carbon footprint is also a vital task, this study also conducts an environmental assessment of these electricity generation technologies from a life cycle standpoint (LCA) which not only takes into account their steady state emissions (if any), but also the upstream manufacturing related emissions caused during the fabrication or production of their respective equipments. The economic and environmental assessment results of this work are compared with those of conventional fossil fuel energy generation technologies. With this context, this study will allow researchers, investors or public policy makers to make informed decisions from an economic and environmental standpoint.

1.2. RESEARCH OBJECTIVES

The aim of this dissertation is to develop a methodology that conducts a techno-economic and environmental life cycle analysis of a renewable energy microgrid. There are three specific objectives of this dissertation:

1. Develop a methodology that assesses the technical, economic and environmental performance of a small scale microgrid composed of seven components, namely, solar photovoltaics, wind turbine, lead acid battery, biodiesel generator, fuel cell, electrolyzer and H_2 cylinders. Test this methodology for US cities of Tucson, Lubbock and Texas.

2. Utilize Artificial Neural Networks to predict the energy consumption of two US cities and extend the methodology provided in step I by incorporating carbon taxes to analyze its effect on electricity costs for microgrid as well as conventional grid.

3. As the microgrid comprises of a biodiesel generator, analyze the upstream production process of biodiesel production. More specifically, conduct a techno-economic assessment of a novel supercritical biodiesel production process from waste cooking oil.

PAPER

I. TECHNO-ECONOMIC OPTIMIZATION AND ENVIRONMENTAL LIFE CYCLE ASSESSMENT OF MICROGRIDS LOCATED IN THE US USING GENETIC ALGORITHM

Prashant Nagapurkar[a], Joseph D. Smith[a]

[a]Chemical and Biochemical Engineering department, Missouri University of

Science and Technology, Rolla-65401,MO, USA

ABSTRACT

A methodology was developed that assessed the techno-economic and environmental performance of a small scale microgrid located in US cities of Tucson, Lubbock and Dickinson. Providing uninterrupted power the microgrid was composed of seven components - solar photovoltaics, wind-turbines, lead acid batteries, biodiesel generators, fuel cells, electrolyzers and H2 tanks. Firstly, detailed mathematical models that predicted the hourly energy generation for each of the components were developed and validated. Secondly, based on an electricity dispatch strategy, configurations having lowest LCOE (Levelized Cost of Energy) were determined using an evolutionary optimization technique - Genetic Algorithm (GA). Results for a single home microgrid were verified using an exhaustive search technique that scanned the entire design space to find the lowest LCOE configuration. The microgrid size was subsequently increased to satisfy power requirements for 10 and 50 homes and new lowest LCOE configurations were determined using GA to examine the economies of scale effect on sustainability.

The LCOEs obtained were in the range of \$0.32-0.42/kWh and were also compared with similar economic analyses available in the literature. The carbon footprint (LCA GHG emissions – CO2 eq.) was extremely low and was approximately 1/10th as that of an equivalent conventional electric grid.

Keywords

Hybrid systems; Microgrid; Techno-economic assessment; Environmental assessment (LCA); Genetic Algorithm; Optimization

Highlights

- Techno-economic optimization & environmental analysis (LCA) of microgrid was done.
- Found optimum configurations that had lowest LCOE (\$/kWh) using Genetic algorithm.
- Analyses were done for 1, 10, 50 homes capacity microgrid in 3 different US cities.
- Varying capacity revealed LCOE fell by 7-12% depicting economies of scale effect.
- LCOE (no subsidies) was \$0.32-0.42/kWh & CO_2 emissions 1/10th of conventional grid.

1. INTRODUCTION

The world is heavily reliant on fossil fuel sources to meet its energy demand. In 2015, approximately 80% of the total demand was met by combusting fossil fuels. Furthermore, relative to 1973 levels, the carbon dioxide (CO2) emissions attributed to

fossil fuel combustion doubled in quantity to about 32,294 metric tons [1]. Therefore, to decrease the reliance on fossil fuels and mitigate CO_2 emissions, transition should be made towards generation of power from renewable sources. The outlook for this energy transition seems positive as it is estimated that by 2022, power generation via renewables is going to increase globally by over 33% with solar and wind sources together expected to account for over 80% of the total growth in generation capacity [1]. However, one of the main challenges towards widespread implementation of renewable sources is that they are intermittent in nature. This problem can be tackled by bringing together different renewable sources in an entity known as 'microgrid'. Studies have shown such an approach can increase the overall system efficiency and reliability [2]. Microgrids can be defined as a group of interconnected loads and electricity generation units that possess the capability to connect with the main grid or operate in a standalone mode [2]. Researchers have shown them to be an economically viable option than those systems which rely only on a single source of renewable energy [3]. Specifically, for remote islands and off-grid communities, microgrids have proven to be an economically superior option than conventional electric grid [4]. However, designing a right combination of renewable sources in a microgrid is crucial to overcoming intermittency and ensuring economic feasibility. Recent studies have focused on finding the optimum design and size of a microgrid by taking into the local account electricity load profiles and the availability of renewable resources. The optimization sizing problem is non-convex and non-linear in nature as there can be multiple solutions, and also due to the sheer number of input variables (capacities of solar PV, wind turbines, batteries, etc.) present [5]. As a result, this sizing task can be very time consuming. Thus, stochastic solution techniques

such as evolutionary algorithms have been used to tackle it. Maleki et al. adopted an artificial bee swarm optimization (ABSO) algorithm to design and size a lowest cost microgrid that was composed of solar photovoltaic panels (PV), wind turbine (WT) and fuel cell (FC) systems [5]. Shang et al. used an improved particle swarm optimization (PSO) technique to size batteries for a hybrid energy system composed of PV, WT and diesel generator (DG) systems. A cost minimizing objective function was employed in this study to analyze scenarios with different penetration levels of renewable energy in the microgrid [6]. For a remote area in Iran, Maleki et al. designed a PV, WT and battery based hybrid energy system that had the least cost by using a PSO based Monte Carlo method [7]. A similar techno-economic study for four different regions in Iran was conducted in which a hybrid energy system of PV, WT, FC and battery banks were optimally sized. The hybrid systems were found to have lower costs than those systems that had only one renewable component [8]. Ramli et al used a self-adaptive differential evolution algorithm with multiple optimization objectives such as minimization of cost, minimization of loss of power supply probability (LPSP) and maximization of renewable fraction to design a hybrid energy system in Yanbu, Saudi Arabia. This system was composed of PV, WT, batteries and DGs [9]. Using HOMER software, Phurailatpam et al. sized a microgrid for rural and urban applications in India that had lowest net present cost while also evaluating CO_2 emissions [10]. To size a microgrid, another study performed a triple multi-objective optimization analysis using genetic algorithm to minimize cost, CO_2 emissions and unmet load [11]. Some other studies also used multi-objective optimization techniques to size a microgrid while simultaneously minimizing LCOE and CO_2 emissions [12,13]. Somma et al. [14] and Rezvani et al. [15] utilized

multi-objective optimization method that considered economic and environmental aspects for operation scheduling in microgrids. A similar study was done by Elsied et al. in which the authors used a binary particle swarm multi-objective optimization method to minimize cost and emissions [16].

Previously mentioned studies were mainly focused on finding an optimal size of a microgrid that had the lowest levelized cost of energy (LCOE) and LPSP value [5-9]. There were some studies that also evaluated the carbon footprint of the microgrid [10-16]. Researchers also used commercial software tools such as Hybrid Optimization of Multiple Energy Resources (HOMER), Distributed Energy Resources Customer Adoption Model (DER-CAM) and TRNSYS to perform techno-economic and environmental assessment based on location, load and renewable sources [10, 17]. Even though a quick assessment of the microgrid can be made using these tools, they operate in a black box manner. The ability to view, modify or add new individual mathematical models of renewable energy generation technologies is not possible in these tools. Realizing that the entire microgrid model is only as accurate as its individual component models, there is a need to validate these individual components against experimental data or with similar software tools. However, none of the above mentioned studies made an effort to validate the results of their software tools. In addition to this, the comparison of final results with similar microgrid analyses were also not made by these studies. Another research gap in these studies was that they did compare their results with those of an equivalent conventional electric grid [7-17]. Such a comparison is important because the microgrid is competing with the conventional electric grid. Therefore, it is imperative that the techno-economic and environmental results of its analysis should be compared with

those of conventional electric grid. Aforementioned studies also did not evaluate the effect of scaling up of microgrid on cost and emissions. Addressing all these gaps, there are four novel contributions of the current study which are as follows:

1. Develop techno-economic and environmental assessment models of a microgrid that is composed of PV, WT, LB, FC, BDG, EM and H2 tanks and validate the technical models (PV, WT, FC) with experimental data and other software tools.

2. Optimally size a lowest cost microgrid using GA and verify its solution using an exhaustive search (brute force) method for a single home in 3 US cities.

3. Scale up the microgrid size to 10 and 50 homes to examine its effect on cost ($/kWh) and CO2 emissions.

4. Compare the cost and emissions of microgrid with conventional electric grid and with other studies in literature to assess its economic feasibility and environmental sustainability.

The methodology in this work was implemented for a residential community situated in three US cities, namely, Tucson in Arizona state, Lubbock in Texas state and Dickinson in North Dakota state. The schematic diagram of the microgrid is shown in Figure 1.

The technical, economic and environmental assessment metrics evaluated for the microgrid were, LPSP, LCOE ($/kWh) and CO2 emissions (kg eq. emitted/year) respectively. The entire work was carried out in three steps. In the first step, electricity generated by primary sources such as PV and WT was calculated based on location and individual module generating capacity. In the second step, based on hourly load and electricity generated, an electricity dispatch strategy was adopted.
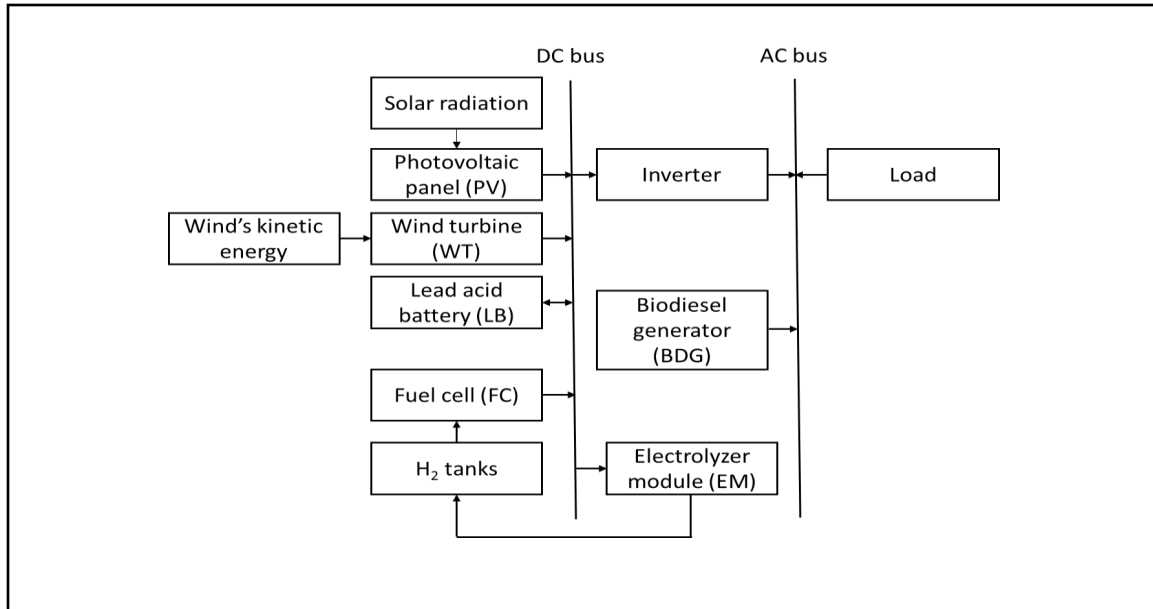
Figure 1 Schematic diagram of proposed microgrid configuration

Through this dispatch strategy, the power generated by secondary sources as LB, BDG, FC and EM was estimated. In the last step, using a sizing algorithm, an optimum configuration of microgrid was found out which provided uninterrupted power at lowest annual LCOE. This solution was found out by a genetic optimization algorithm (GA) and then the solution was verified by an exhaustive search algorithm (ESA) for a single home. As simulation became more computationally intensive and time consuming (for 10 and 50 homes), only GA was used to find optimum microgrid configurations due to its accuracy and rapid convergence time. The LCOE and CO_2 emissions of the electricity generated by the microgrid were then compared with those of a conventional electric grid.

This paper is organized as follows: Section 2 describes the renewable energy potential of the cities considered in this study. Section 3 develops the mathematical models of individual components in the microgrid and formulates the optimization

problem. Section 4 deals with the optimization algorithm utilized to find the desired

microgrid configuration. Section 5 and section 6 deal with results and conclusions

respectively.

2. RENEWABLE ENERGY POTENTIAL OF CONSIDERED CITIES

The solar and wind energy potentials of the three US cities are depicted in Figure

2. The hourly solar radiation (direct normal irradiance) averaged for the entire year in

case of Tucson is 0.29 kWh/m2. This value is 20% and 64% higher than that of Lubbock

and Dickinson respectively. However, the wind potential, in terms of yearly averaged

wind speed (m/s) for Tucson is 3.58 m/s it is 59% and 44% less than of Lubbock and

Dickinson respectively. These values indicate that, amongst all cities, Dickinson has

highest wind potential but lowest solar potential while Tucson has highest solar potential

but lowest wind potential.
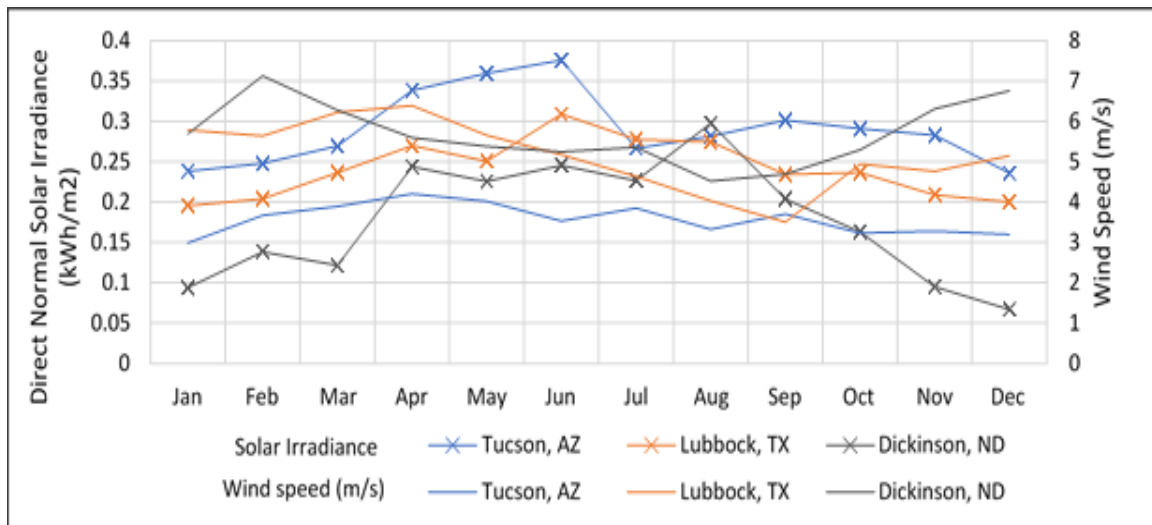
Figure 2 Solar and Wind energy potential of all three US cities

The solar and wind potential of Lubbock lies in between the other two cities. The location specific hourly values for solar radiation and wind speed were procured from typical meteorological year (TMY3) data set which is available online at National Renewable Energy Laboratory's (NREL) website [18].

3. MODEL DEVELOPMENT

This section deals with the mathematical modeling of individual components in a microgrid from systems perspective. The technical model is presented first, followed by economic and environmental emissions' models.

3.1. TECHNICAL MODEL DEVELOPMENT

The following section describes the models of individual components such as PV, WT, LB, BDG, FC, EM and H_2 tanks.

3.1.1. Solar Photovoltaic Model. The solar photovoltaic model is divided into two parts, namely, solar radiation model and PV panel model.

3.1.1.1. Solar radiation model. The solar radiation model shown here estimates the amount of solar radiation that is incident on a tilted solar panel, $G\beta$ (W/m2) and was given by [19]:

$$G_\beta(t) = G_{b,\beta}(t) + G_{r,\beta}(t) + G_{d,\beta}(t) \tag{1}$$

Here, $G_{b,\beta}$, $G_{r,\beta}$, $G_{d,\beta}$ are the hourly beam (or direct), reflected and the sky diffuse components of solar radiation respectively. To calculate these components, measured hourly solar radiation data for extraterrestrial radiation on a horizontal surface

(ETR) and the global horizontal irradiance (GHI) were procured from the TMY3 data set [18].

3.1.1.2. Tilted beam component ($G_{b,\beta}$). To calculate Gb,β, the value of clearness index (k) was computed in the first step using the below equation [20]:

$$k(t) = \frac{GHI(t)}{ETR(t)} \tag{2}$$

Diffuse fraction (f) was then calculated using the following correlations [20]:

$$f(t) = 0.995 - 0.081k(t) \; for \; k(t) \le 0.21 \tag{3}$$

$$f(t) = 0.724 + 2.738k(t) - 8.321k^2(t) + 4.967k^3(t) for \; 0.21 < k(t) \le 0.76 \tag{4}$$

$$f(t) = 0.18 \; for \; k(t) > 0.76 \tag{5}$$

The value of horizontal diffuse component (Gdh) was computed using the following equation [20]:

$$G_{dh}(t) = f(t) \; GHI(t) \tag{6}$$

Finally, Gb,β can be calculated using the Klucher model [21]:

$$G_{b,\beta}(t) = (GHI \; (t) - G_{dh}(t))\frac{\cos\theta(t)}{\cos\theta_z \; (t)} \tag{7}$$

Here θ and θz are incidence and zenith angles respectively.

3.1.1.3. Reflected beam component ($G_{r,\beta}$). Gr,β was estimated assuming that the diffuse and reflected components of solar radiation were isotropic in nature. Gr,β was computed by [21]:

$$G_{r,\beta}(t) = \frac{\rho}{2} GHI(t)(1 - \cos\beta) \tag{8}$$

Here β is the tilt of the solar panel (taken as 20^0) and ρ is the albedo (taken as 0.2).

3.1.1.4. Tilted diffuse component (Gd,β). Gd,β was estimated by incorporating a factor 'fk', which takes into account the effect of cloudy conditions on solar irradiance. This factor 'fk' was calculated by [21]:

$$f_k(t) = 1 - \left(\frac{G_{dh}(t)}{GHI(t)}\right)^2 \tag{9}$$

The expression used for Gd,β was given by [21]:

$$G_{d,\beta}(t) = G_{dh}(t)\left[0.5\left(1 + \cos\frac{\beta}{2}\right)\right]\left[1 + f_k(t)\left(\sin\frac{\beta}{2}\right)^3\right][1 + f_k(t)(\cos\theta(t))^2(\sin\theta_z(t))^3] \tag{10}$$

Finally, Gβ was calculated from the values of Gb,β , Gr,β and Gd,β using equation 1.

For all the three cities, the monthly Gβ values of solar radiation using the above were validated with the corresponding values estimated by National Renewable Laboratory's (NREL) software tool known as System Advisor Model (SAM) [22].

3.1.1.5. PV panel model (PV). The PV panel model predicts the hourly power (DC) generated primarily based on the values of Gβ. It was assumed that the PV module always operates at the maximum power point. The maximum power point current (Imp) and voltage (Vmp) values for every hour were found by simultaneously solving the two non-linear equations in Matlab which were as follows [23]:

$$\frac{I_{mp}(t)}{V_{mp}(t)} = \left[\frac{\frac{I_o(t)}{a(t)}\exp\left(\frac{Vmp(t)+I_{mp}(t)R_S(t)}{a(t)}\right) + \frac{1}{R_{sh}(t)}}{1 + \frac{R_S(t)}{R_{sh}(t)} + \frac{I_o(t)R_S(t)}{a(t)}\exp\left(\frac{Vmp(t)+I_{mp}(t)R_S(t)}{a(t)}\right)}\right] \tag{11}$$

$$I_{mp}(t) = I_L(t) - I_o(t)\left[\exp\left(\frac{Vmp(t)+I_{mp}(t)R_S(t)}{a(t)}\right) - 1\right] - \left[\frac{Vmp(t)+I_{mp}(t)R_S(t)}{R_{sh}(t)}\right] \tag{12}$$

However, in order to solve the above two equations, five parameters were needed, namely, light current (IL), diode reverse saturation current (Io), modified ideality factor (a), series resistance (Rs) and shunt resistance (Rsh). These parameters were calculated

for every hour from their own reference condition values (T_c,ref = 25 ^{0}C and G_β,ref =

1000 W/m2). For BP4175B (power capacity 175W) module, parameter values at

reference conditions for IL,ref, Io,ref, aref, Rs,ref, Rsh,ref were taken to be 5.467A, 1.452

x 10^{-9}A, 1.982V, 0.495Ω and 155Ω respectively [22]. The expressions to compute hourly

values of five parameters are provided in the following sections.

3.1.1.6. Module (cell) temperature (T_c). The hourly value of Tc (^{0}C) depends on

two factors, namely, the temperature of the surroundings (Tamb, ^{0}C) and the amount of

incident solar radiation, Gβ (W/m2) and was given by [23]:

$$T_c(t) = T_{amb}(t) + (T_{NOCT} - 20)\frac{G_\beta(t)}{800}\left(1 - \frac{\eta_c}{0.9}\right) \tag{13}$$

Here, Tamb was obtained from TMY3 file [20], TNOCT (46.5 ^{0}C) is the nominal

operating cell temperature, and η_c is the module or cell efficiency (13.9%) [22, 23].

3.1.1.7. Light current (I_L). I_L (A) depends linearly on Gβ and T$_c$ and was

calculated by [23]:

$$I_L(t) = \frac{G_\beta(t)}{G_{\beta,ref}}\left[I_{L,ref} + \mu_{I,sc}(T_c(t) - T_{c,ref})\right] \tag{14}$$

Here, $\mu_{I,sc}$ (0.005 A/^{0}C) was the short circuit temperature coefficient of the solar

module [22].

3.1.1.8. Modified ideality factor (a). a (V) depends linearly on the cell

temperature (expressed in K) and was computed by [23]:

$$\frac{a}{a_{ref}} = \frac{T_c}{T_{c,ref}} \tag{15}$$

3.1.1.9. Shunt resistance (R_{sh}). R$_{sh}$ (Ω) was assumed to be dependent on Gβ and

was estimated by [23]:

$$\frac{R_{sh}(t)}{R_{sh,ref}} = \frac{G_{\beta,ref}}{G_\beta(t)} \tag{16}$$

3.1.1.10. Reverse diode saturation current (I_o). I_o (A) was assumed to be dependent on T_c, material bandgap for Silicon (E_g, J) and was computed by [23]:

$$\frac{I_o\,(t)}{I_{o,ref}} = \left(\frac{T_c\,(t)}{T_{c,ref}}\right)^3 exp\left[\frac{1}{k}\left(\frac{E_{g,ref}}{T_{c,ref}} - \frac{E_g\,(t)}{T_c\,(t)}\right)\right] \tag{17}$$

Here, k was the Boltzmann constant (1.38 x 10^{-23} J/K). The value of E_g was estimated by [23]:

$$\frac{E_g\,(t)}{E_{g,ref}} = 1 - 0.000267\left(T_c\,(t) - T_{c,ref}\right) \tag{18}$$

The value for $E_{g,ref}$ was taken as 1.794 x 10^{-19} J [23].

Using equations 13 - 18, hourly values for I_L, a, R_{sh} I_o were estimated and were plugged into equations - 11 and 12 to find I_{mp} and V_{mp}. Subsequently, hourly power, $P_{gen,PV}$ (W) produced by the module was computed by [23]:

$$P_{gen,PV}(t) = V_{mp}(t)I_{mp}(t) \tag{19}$$

Above equation computes the energy generated by a single PV module of 175W capacity. 5.7 modules were connected in series to increase the capacity to 1kW. The monthly power generated by these modules was validated with the corresponding values estimated by SAM software. [22]

3.1.2. Wind Turbine (WT) Model. The instantaneous power generated by the wind turbine depends on three types of wind velocities.

These velocities are the cut-in wind speed v_C (m/s), the rated wind speed v_R (m/s) and the cut-off speed v_F (m/s). These wind speeds in turn depend on the type and model of wind turbine deployed. There are numerous models that are available in the literature that predict power output of a wind turbine. Tina et al. used a linear model [24], while

Diaf et al. [25] and Mohammadi et al. [26] utilized a quadratic and cubic model

respectively.

In this work, a quadratic equation was employed as it was shown to better predict

values when validated with values calculated by SAM software.

For WT model, a Bergey BWC XL wind turbine of 1 kW rated capacity (P_R) was

chosen and the values assumed for v_C, v_R and v_F were 3 m/s, 12 m/s and 23 m/s

respectively [22].

Based on these wind speed values, the hourly power generated by the wind

turbine, $P_{gen,WT}$ (kW), as a function of wind speed (v) was calculated using the following

equation [25]:

$$P_{gen,WT}(t) = \begin{cases} P_R \left(\frac{v^2(t) - v_c^2(t)}{v_R^2(t) - v_c^2(t)} \right) \ for \ v_c \leq v(t) \leq v_R \\ P_R \ for \ v_R < v(t) < v_F \\ 0 \ for \ v(t) < v_c \ and \ v(t) > v_F \end{cases} \tag{20}$$

Location specific hourly wind speed data at 100m was procured from NREL's

database [27]. The corresponding wind speeds (v), adjusted to 30m hub height (H) were

calculated using the following equation [25]:

$$v(t) = v_{ref}(t) \left(\frac{H}{H_{ref}} \right)^{\alpha} \tag{21}$$

Here α is the wind speed power law coefficient and can its value can be taken as

(1/7) assuming well exposed sites [25].

The power generated by wind turbine was computed using the above

methodology and was validated with the values generated by SAM software.

3.1.3. Lead Acid Battery (LB) Model. Electrochemical energy storage are widely used in microgrids via lead batteries due to their low capital and maintenance costs as compared to Lithium ion batteries [28]. In this work, a normalized and generalized LB model was used as it had shown excellent ability to represent a wide range of lead acid batteries [29,30].

In the studies that focus on microgrid analyses, most of them employed a simple energy balance to compute the energy stored in the battery and its state of charge [3,4,6,11]. The simplified battery model used in these studies did not take into account the transient behavior of battery variables which is depicted by current, voltage, capacity and charging efficiency. Therefore in this work, transient modeling of such variables was carried out and their values were computed for every hour in a year.

For simulation purposes, the nominal values of voltage (V_{nom}), current (I_{nom}) and capacity (C_{nom}, at 10 hours discharge rate) for a single electrochemical accumulator were assumed to be 2V, 55A and 550 Ah respectively [29,30]. A single battery unit was assumed to be composed of 20 such accumulator connected in series amounting to a total energy capacity of 22 kWh.

3.1.3.1. Instantaneous state of charge (ISOC). C_{batt} denotes the amount of energy (Ah) that the battery can restore. Its transient behavior depends on the amount of current flowing through it (I_{batt} (t)), ambient temperature condition (T_{amb}) and was expressed by the following equation [29,30]:

$$C_{batt}(t) = \frac{1.67\, C_{nom}[1+0.005\,(T_{amb}(t)-25)]}{\left[1+0.67\left(\frac{|I_{batt}(t)|}{I_{nom}}\right)^{0.9}\right]} \tag{24}$$

3.1.3.2. Charging and discharging efficiency. A coulombic charging and discharging efficiency model is adopted in this work which neglects any losses associated

due to battery's internal resistances. The battery's discharging efficiency was assumed to be 100%. However, C_{eff} is a function of ISOC and I_{batt} and was given by [29,30]:

$$C_{eff}(t) = 1 - exp\left[\frac{20.73\ (ISOC(t)-1)}{\frac{I_{batt}(t)}{I_{nom}}+0.55}\right] \tag{25}$$

3.1.3.3. Instantaneous battery voltage (V_{batt}). V_{batt} depends on its internal elements, namely, the electromotive force and the internal resistance and is also affected by T_{amb}. V_{batt} during charging regime of battery was given by [29,30]:

$$V_{batt}(t) = N_b\left[2 + 0.16\ ISOC(t)\right] + N_b\frac{I_{batt}\ (t)}{C_{nom}}\left[\frac{6}{1+I_{batt}(t)^{0.86}} + \frac{0.48}{(1-ISOC(t))^{1.2}} + 0.036\right]\left(1 - 0.025\ (T_{amb}(t) - 25)\right)$$

(26)

V_{batt} during discharging regime was expressed by the following equation [29,30]:

$$V_{batt}(t) = N_b\left[1.965 + 0.12\ ISOC(t)\right] - N_b\frac{|I_{batt}\ (t)|}{C_{nom}}\left[\frac{4}{1+|I_{batt}(t)|^{1.3}} + \frac{0.27}{ISOC(t)^{1.5}} + 0.02\right]\left(1 - 0.007\ (T_{amb}(t) - 25)\right)$$

(27)

In the above equations, N_b is the number of battery units.

3.1.4. Biodiesel Powered Electric Generator (BDG). Microgrids have been frequently designed with the inclusion of a conventional diesel powered generator [3,4,9,11,13].

Few techno-economic studies incorporate a biodiesel powered generator [10,12]. On a life cycle basis, biodiesel emits 66-72% less greenhouse gas (GHGs) emissions than conventional diesel [31]. Therefore, in this work, with an objective to enhance sustainability and reduce the overall carbon footprint, a biodiesel powered generator was chosen to provide electric power to the microgrid. To generate the same amount of power in an electric generator, the specific fuel consumption (kg/kWh) of biodiesel is higher than that of conventional diesel and the relative increase in fuel consumption varies

between 4.6% and 11.9% [32]. Assuming an average value of 8%, the biodiesel

consumption, C_{BD} (lit/h) of the electric generator was given by [11]:

$$C_{BD} = 1.08 \left(0.08145 \, P_{NG} + 0.2476 \, P_{gen} \right) \tag{28}$$

Here P_{NG} (kWh) is the nominal power rating of the generator and P_{gen} (kWh) is the

power generated by it.

3.1.5. Fuel Cell (FC). Fuel cells (FC) are characterized by their ability to generate

clean power at low operating temperatures [33].

Proton exchange membrane fuel cells (PEMFC), a type of FCs, have been widely

used for power generation purposes in automobiles as well as in stationary and portable

electricity generation units. They are widely used due to their capability of generating

power with efficiencies of 40-60% which are higher than most of the other energy

conversion pathways [33].

A PEMFC consists of a cathode and an anode separated by a polymer electrolyte

membrane. Pure H_2 is fed to anode where it is oxidized, while oxygen (mostly via air) is

supplied to cathode where it is reduced, subsequently producing water and heat.

The voltage (E_{cell}) of the FC was computed using the following expression [34]:

$$E_{cell} = E_{oc} - E_{act} - E_{con} - E_{ohm} \tag{29}$$

Where E_{oc}, E_{act}, E_{con}, E_{ohm} denote the values for open circuit voltage, activation

overpotential, concentration overpotential and ohmic overpotential respectively. E_{cell} was

calculated by implementing the one dimensional mathematical model developed by

Abdin et al [34] in Matlab. For modeling a single PEMFC, an active area of 51.84 cm^2

[34] and an electrical efficiency of 42% was assumed [35]. The model consisted of four

parts, namely, anode (9 equations), cathode (8 equations), membrane (8 equations) and voltage (22 equations). The complete mathematical model was sequentially solved.

The information with regards to FC's mathematical model, its physical parameters and its validation with experimental data is provided in the SID.

By referring power-current density curve, the power generated by a single PEMFC was estimated to be approximately 25W.

Forty such PEMFCs (N_{FC}) were then assumed to be connected in series to scale up the capacity to 1kW. H_2 consumption (N_{H2}) in moles per hour by the entire unit was calculated using the following expression [34]:

$$N_{H2} = \frac{S_{H2}IN_{FCs}}{2F} \; x \; 3600 \tag{30}$$
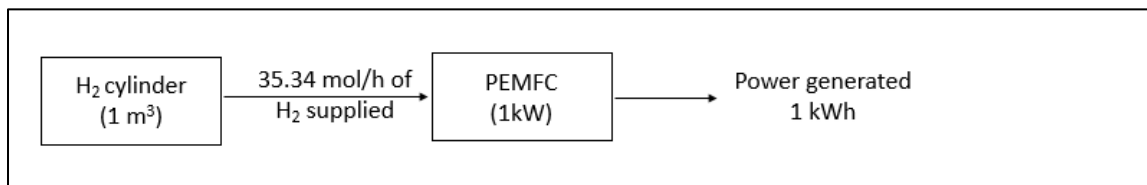
Figure 3 Systems level interaction and energy balance between H2 cylinder and PEMFC

Here, the stoichiometry molar ratio of H_2 at anode (S_{H2}) and Faraday's constant was taken to be 1.2 and 96,485 C/mol respectively [34]. The value of current (I) was estimated to be 39.47 A.

Inserting all these values in the equation - 30 , the H_2 consumption rate of a 1kW PEMFC capacity was computed to be 35.34 mol/hr.

The systems level interaction and energy balance between H_2 cylinder and PEMFC is shown in Figure 3.

3.1.6. Electrolyzer Module (EM). An electrolyzer is a FC operating in a reverse direction splitting water molecules into H_2 and O_2 by consuming electrical energy.

It consists of two electrodes (cathode and anode) separated by a PEM [36]. Protons from anode diffuse through the PEM while electrons travel through the external circuit to reach cathode, where they combine together to produce H_2 gas. For modeling purposes, current (η_i) and voltage efficiencies (η_v) were assumed to be 100% and 74% respectively [37]. The operating voltage (V_{elec}) of the EM was calculated using the following equation [37]:

$$\eta_v = \left(\frac{1.48}{V_{elec}}\right) x100 \tag{31}$$

The H_2 produced in moles per hour (N_{H2}) by the EM was computed using the Faraday's law of electrolysis as follows [37]:

$$N_{H2} = \left(\frac{P_{EM}}{V_{elec}\ 2F}\right) x3600 \tag{32}$$

Where P_{EM} (W) is power consumption of the EM. For an EM of 1kW rated capacity, N_{H2} was determined to be 9.33 moles per hour. The discharge pressure of the EM was 0.6 MPa based on experimental studies reported in the literature [37].

3.1.7. Compressor and H_2 Cylinders. The H_2 discharged from the EM was pumped to 13.5 MPa through a compressor and was stored in the cylinder. The power requirement of the compressor was given by [37]:

$$W_c = \frac{C_p T_1 m_c}{\eta_c}\left[\left(\frac{P_2}{P_1}\right)^{\frac{r-1}{r}} - 1\right] \tag{33}$$

The values for all the parameters in the above equation are provided in the SID. The total energy consumed by the EM and compressor to inject 9.33 moles of H_2 in the

cylinder was 1.045 kWh. The systems level energy balance and the interaction between

the EM, compressor and the H_2 cylinder is shown in Figure 4.
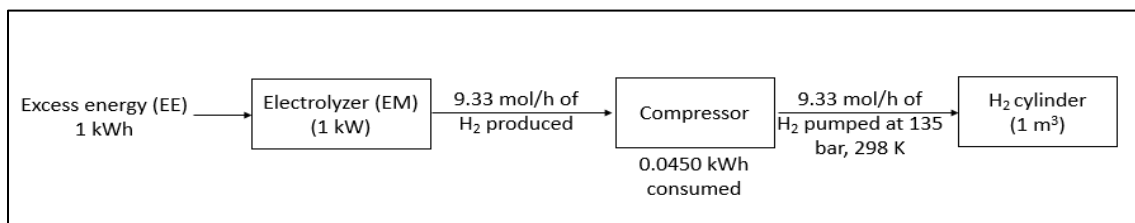
Figure 4 Systems level interaction and energy balance between electrolyzer (EM),
compressor and H2 cylinder

3.1.8. Electricity Consumption Model. For all the cities, the average hourly

electricity usage for a single home was procured from NREL's database [38].

For a single home, the average hourly electricity load for the all the three cities

are depicted in Figure 5. The usage for 10 and 50 homes were linearly extrapolated by

assuming that every home in a specific location used equal amounts of electricity.
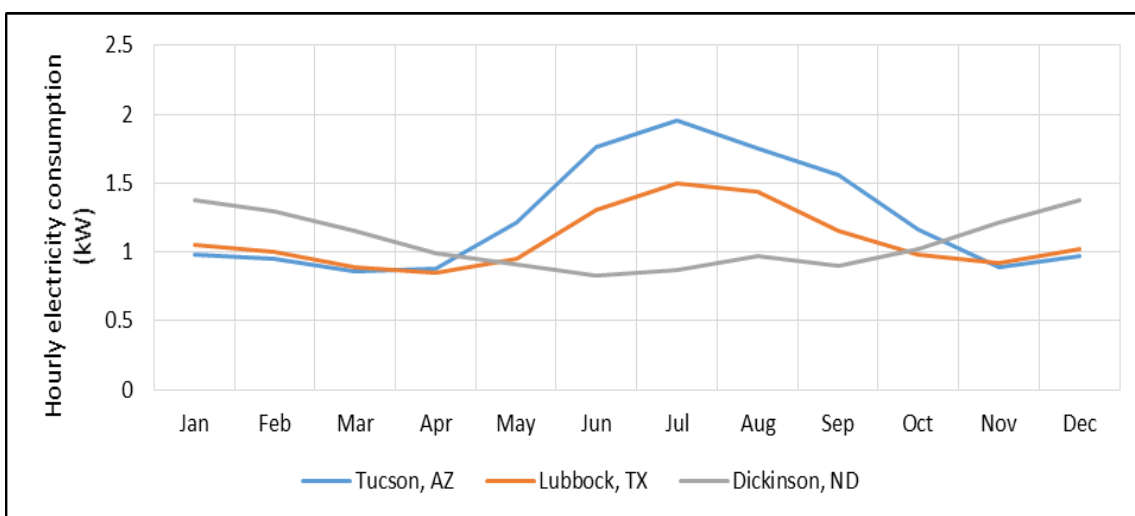
Figure 5 Average hourly electricity load for a single home in all the three cities [35]

3.2. ECONOMIC AND ENVIRONMENTAL ASSESSMENT

Prior studies on microgrid have included the minimization of CO_2 emissions in their main optimization objectives [11-16]. Even though the minimization of carbon emissions is a vital objective, however, the only way to accelerate the widespread public acceptance and implementation of microgrids is to devise solutions that possess the least cost. An environmentally friendly solution would be difficult to finance if it is an expensive one. Therefore, in this work, the sole objective was to determine microgrid configurations which possess the lowest cost of energy. The carbon footprint of these configurations was later assessed.

3.2.1. Economic Assessment.

3.2.1.1. Objective function. The expression to calculate LCOE ($/kWh), and the objective (minimization) function was given by [9,37]:

$$LCOE = \frac{TAC}{P_{L,an}} \tag{34}$$

Here $P_{L,an}$ was the annual electricity demand (kWh). TAC ($) wass the total annualized cost of the microgrid and was given by the following equation [25]:

$$TAC = PVC\ CRF \tag{35}$$

Here, PVC is the present value of costs for acquisition, installation, maintenance and replacement of microgrid components. CRF is the capital recovery factor and was expressed by [25]:

$$CRF = \frac{d\ (1+d)^T}{(1+d)^T - 1} \tag{36}$$

Here, d was the discount factor (8%) and T was the lifetime of microgrid (20 years).

3.2.1.2. Effect of inflation and technology maturation on costs. Prior microgrid analyses utilized simple cost estimation models to perform economic assessments. For instance, the effect of inflation on capital and maintenance costs was neglected in some analyses [4,5-10,12]. The typical lifetime of microgrid is 20-25 years and during that time some components (LB, FC, EM) may need replacement every 5 years. Therefore, neglecting the effect of inflation on capital cost of such components may result in an inaccurate cost estimation. Furthermore, these studies also neglected the fall in costs due to technology maturation. It was therefore assumed that in this work, the acquisition costs for these components fall 10% (g_k=-0.1) every year until they reach they reach 50% (Lg_k=-0.5) of their initial acquisition value (at the time of initial investment, t = 0 years). This time (Y_{mat}, in years) for reaching 50% reduction was calculated by [39]:

$$Y_{mat} = \frac{\log(1+Lg_k)}{\log(1+g_k)} \tag{37}$$

For components such as LB, FC and EM, the annual inflation (i) rate of 3% was applied only after the maturation period ended (Y_{mat}=7 years).

For inverters, the inflation rate was applicable from the beginning (time, t=0).

3.2.1.3. Acquisition costs and installation costs. The present values, C_k (per unit) for every component (k) comprised of installation ($Inst_k$) and acquisition costs (P_k, shown in Table 1) were calculated based on the following equations [39]:

For PV, WT, BDG and H_2 the equations were given by [39]:

$$C_k = P_k(1 + Inst_k) \tag{38}$$

For LB, FC and EM components, equations were [39]:

$$C_k = P_k(1 + Inst_k) \left[1 + \left(\frac{1+g_k}{1+d}\right)^5 + \frac{(1+g_k)^7(1+i)^3}{(1+d)^{10}} + \frac{(1+g_k)^7(1+i)^8}{(1+d)^{15}}\right] \tag{39}$$

For inverter the costs were computed by [39]:

$$C_{Inv} = P_{Inv}(1 + Inst_{Inv})\left[1 + \left(\frac{1+i}{1+d}\right)^{10}\right] \qquad (40)$$

The acquisition, installation and maintenance costs of components for a small scale microgrid (up to 50 homes) are shown in Table 1 and were assumed to be the same for all the cities.

The biodiesel consumption costs were assumed to be \$0.91/lit [40].

Table 1 Acquisition, installation, maintenance costs of components and their life spans

Module name	Acquisition costs, P_k ($/W)	Installation costs, $Inst_k$ (%)	Maintenance costs, Mtn_k (%)	Life span (yrs)
Solar PVs (PV) [41]	1.11	40	1	20
Wind turbines (WT) [41]	1.23	20	2	20
Lead acid battery (LB), $/Wh [41]	0.3	20	0	5
Biodiesel generator (BDG) [42]	0.84	10	2	20
Fuel cell (FC) [43]	5.19	10	2	5
Electrolyzer with compressor [5,11,37]	7.6	10	2	5
H$_2$ cylinder, $/cylinder [44]	300	10	0	20
Inverter (Inv) [41]	0.71	10	1	10

3.2.1.4. Maintenance costs. The maintenance costs (CMtn$_k$) were estimated as a direct percentage of initial cost of component (k) in its first year and can be given by [25,39]:

$$CMtn_k = \sum_{T=1}^{T=20} P_k \, Mtn_k \left(\frac{1+i}{1+d}\right)^T \tag{41}$$

Here, Mtn$_k$ is the percentage of the component's acquisition cost and for all the components their respective values were shown in Table 1.

Finally, TAC for the entire microgrid was calculated by [25,39]:

$$TAC = CRF \sum_{k=1}^{k=7}(C_k + CMtn_k) \, N_k \tag{42}$$

Here N$_k$ denotes the number of units of a single type of component (k).

3.2.1.5. Constraints. The seven variables (components) are integer constrained. All these variables are bounded as follows:

$$0 \le N_k \le N_{k,max} \tag{43}$$

Here N$_k$ not only denotes the number of components of a specific component (k) but it also denotes the capacity of that component in kW. For instance, 5 PV components indicates that their net generation capacity is 5 kW. This is true for all components except LB and H$_2$ cylinder. Each LB denotes a storage capacity of 22 kW and each H$_2$ cylinder indicates a volumetric capacity of 1m^3.

The value of N$_{k,max}$ was chosen in such a way that every power generating component (PV, WT, BDG, FC) can comfortably fulfil the peak electricity demand. The maximum value for battery capacity (22 kWh) was chosen in such a way that it can alone fulfil the mean power demand for 10-12 hours. Similarly, the capacity of H$_2$ cylinder (1m^3) was chosen so that it can meet power demand (via FCs) for 2-3 days.

The LB model employed in this work is only operational when the state of charge (ISOC) lies between 20% and 80% which can be given by:

$$0.2 \leq ISOC(t) \leq 0.8 \tag{44}$$

The probability of power supply failure (LPSP) was calculated at every hour in a year by using the following formula [5]:

$$LPSP = \sum_{t=1}^{8760} \left(\frac{P_L(t) - P_{gen}(t)}{P_L(t)} \right) \tag{45}$$

Here, P_L (t) and P_{gen} (t) are the residential load and power generated in the microgrid respectively.

The maximum and minimum pressure rating of the hydrogen cylinders were chosen to be 135 bar and 27 bar [45]. The cylinder model was only operational if the pressure lied between these limits.

$$27 \; bar \leq Pressure \; (t) \leq 135 \; bar \tag{46}$$

3.2.2. Environmental Assessment. The GHG emissions (kg CO_2 equivalent) are estimated based on the amount of energy produced (or stored in case of batteries) by each component.

A life cycle approach (LCA) was adopted to compute the emissions.

The emissions (kg CO_2 eq./kWh generated) for every component are shown in Table 2.

The total annual emissions (TE) of the microgrid was computed using the following equation:

$$TE = \sum_{k=1}^{k=7} (p_k e_k) \tag{47}$$

Here p_i (kWh) is the annual power generated by the component 'k' and e_k is the amount of CO_2 emitted for every unit of electricity (kWh) generated.

Table 2 LCA GHG emissions (kg CO2 equivalents/kWh) [12]

Component	LCA GHG emissions (kg CO_2 eq./kWh), e_k
PV module (mono- Si)	0.045
WT (at speed 6.5 m/s)	0.011
Lead acid battery (per kWh stored)	0.028
Biodiesel generator	0.191
Fuel cell	0.664
Electrolyzer and H_2 tanks	0.011
US conventional electric grid [43]	0.51

4. METHODOLOGY

In this section, initially an energy management strategy (EMS) for the microgrid was proposed.

The EMS was implemented through GA and ESA techniques.

The simulations have been carried out using Matlab software and a computer having a dual core processor (i5-3230M) with 4GB of memory.

4.1. ENERGY MANAGEMENT STRATEGY (EMS)

The hourly EMS of the microgrid was identical for both the algorithms and is depicted in Figure 6.

In the first step, based on meteorological data, electricity generation by PV and WT units (if available) was calculated for a time instant (t).

In the next step, based on the difference between electricity generated and demand, either the amount of excess electricity (EE) or the deficit (ED) was calculated.

At this point, the main EMS diverges into two paths.One for EE and the other for ED.

In case of EE path, the battery (if available) model runs in a charging mode while in case of ED route, the battery runs in a discharging mode.

After discharging mode ends, if more energy is needed (ED>0), then BDG and FC units (if available) are run in sequential order.

After the LB has run in charging mode, if excess energy is still available (EE>0), then EM (if available) unit was operated to generate H_2 gas. This H_2 gas is then compressed and stored in cylinders.

If storage space was not available then H_2 was not generated.

Any EE available after this step was sold back to the conventional grid at wholesale rate (assumed to be 50% of retail price in respective states).

It was also assumed that the infrastructure required for transmitting and distributing electricity back to the conventional grid already exists.Therefore costs related to that were neglected.

The retail cost of electricity per kWh for Tucson, Lubbock and Dickinson were taken to be $0.1033, $0.0843 and $0.0894 respectively [44].

In the final step, LPSP was calculated.
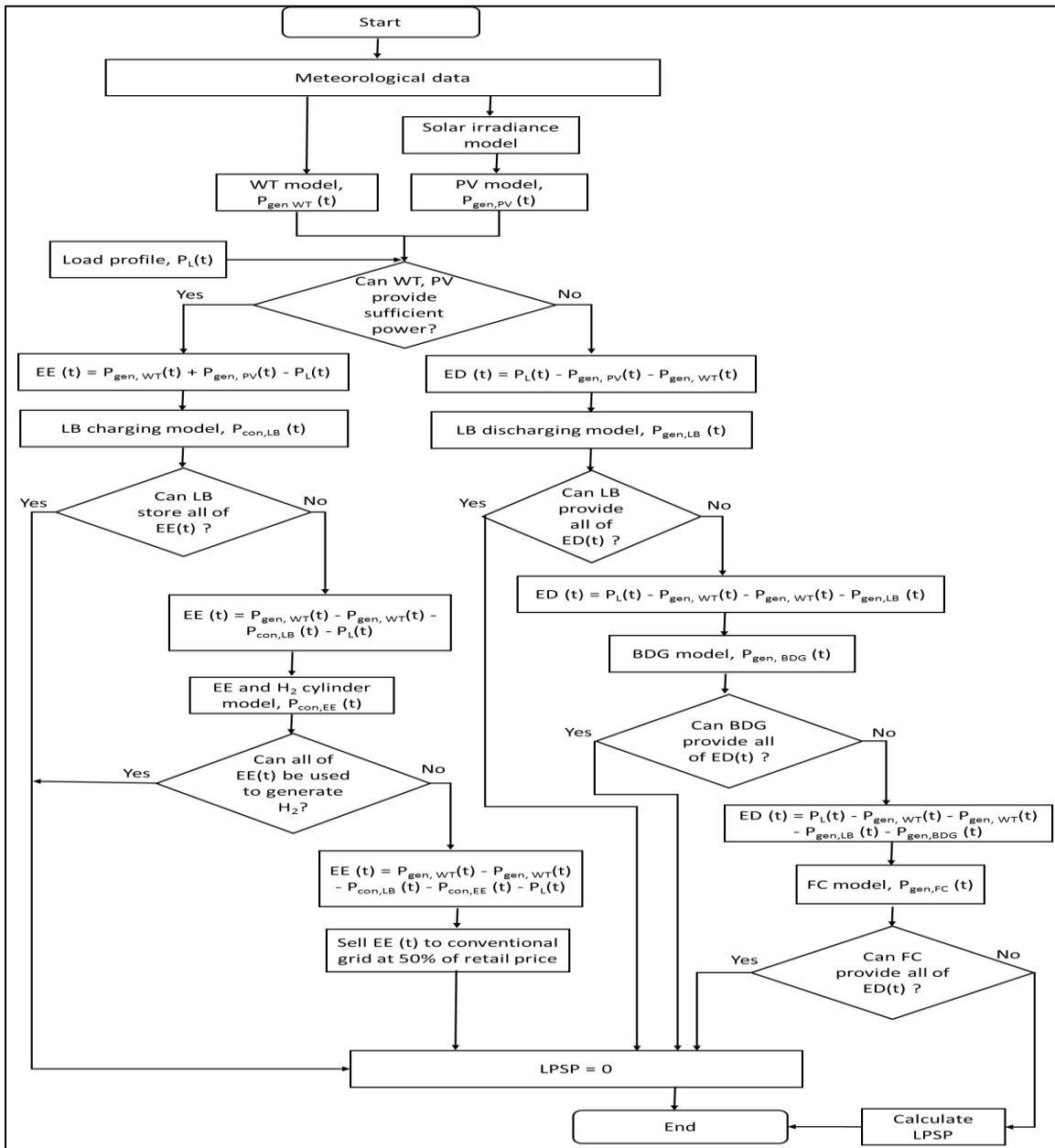
Figure 6 Energy management strategy (EMS) in a microgrid

4.2. GENETIC ALGORITHM (GA)

GA was utilized to find optimum microgrid configurations that were able to provide uninterrupted power (LPSP=0) and which possessed the lowest cost of energy (LCOE). The flowchart for GA is depicted in Figure 7.
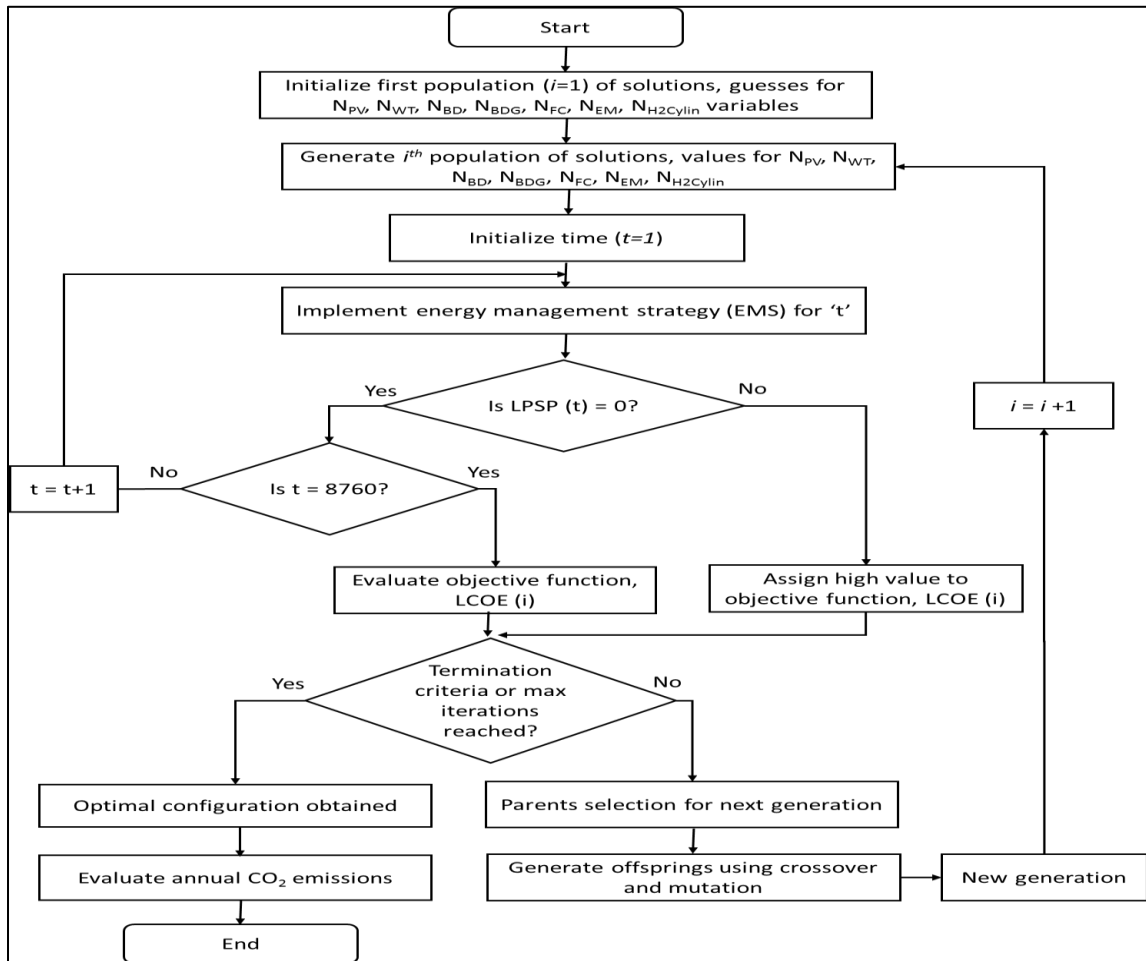
Figure 7 Genetic algorithm (GA) flowchart

Initially, as a first population, a random set of integer combinations (solutions), each one consisting of seven variables was generated. A solution (N_{PV} N_{WT} N_{LB} N_{BDG} N_{FC} N_{EM} N_{H2}) represented a single microgrid configuration. The LCOE (objective function) was computed after implementing the EMS for the entire year. At the end of any hour, if the value of LPSP was determined to be non-zero, then the implementation of EMS was stopped and a high numerical value is assigned to objective function LCOE ($100 /kWh). This was done to steer the GA away from undesirable solutions (microgrid configurations that fail to provide continuous power). The value of LCOE is a measure of

fitness of a solution in the GA. Lower the value of LCOE, higher is the fitness function value. After the LCOEs were determined for every solution in the population, the solutions were ranked according to their fitness value. Then new populations (of solutions) were generated via selection, crossover and mutation of individuals (solutions) within the current population. These newer populations (microgrid configurations) in the new generation were more fitter (lower LCOE) than the ones in the previous generation. Such a procedure was repeated until the maximum number of generations was reached. The optimal solution (microgrid configuration) was the fittest individual in the current generation. The values used for genetic operators are presented in Table 3.

Table 3 Genetic operators values used for GA [48]

Parameter	Population size	Maximum generations	Crossover probability	Mutation probability	Elitism probability
Value	200	700	0.8	0.01	0.05

4.3. EXHAUSTIVE SEARCH ALGORITHM (ESA)

Being a stochastic optimization routine, GA cannot guarantee an exact optimal solution but can converge to a near optimum solution which is close to the global minimum [49]. Therefore, in this work the results of the GA were verified by an ESA (brute force method) that scanned the entire design space, and recorded all the possible microgrid configurations that were able to provide uninterrupted power. The solution which had the least value of LCOE was extracted from these solutions. This entire

process was done only for the case of single home. For 10 and 50 homes only GA was

utilized.
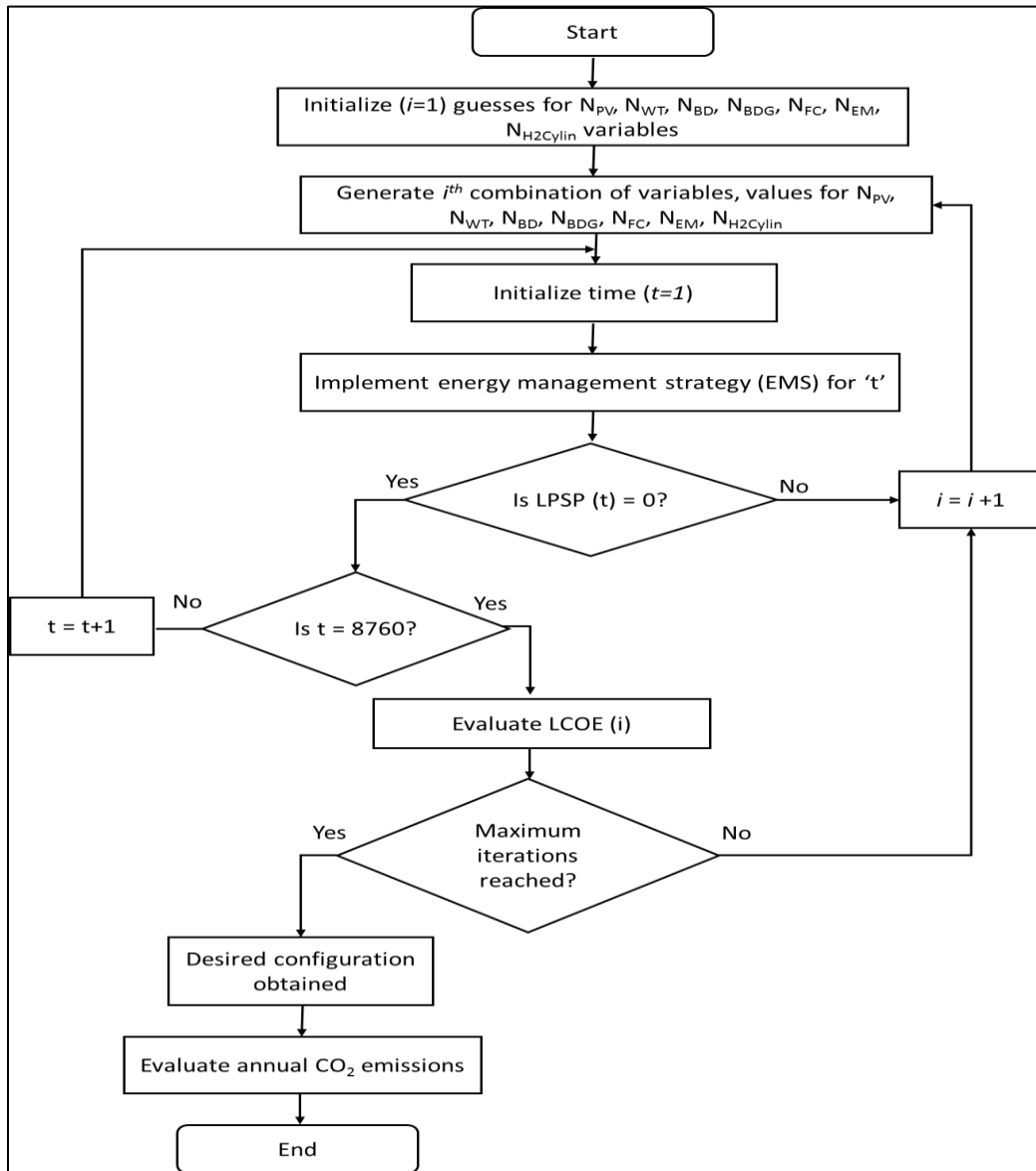
Figure 8 ESA flowchart

The ESA is portrayed in Figure 8. In this procedure, the EMS was implemented

for every time hour of a typical year for all the possible microgrid combinations within

the design space. If at any instant for a given solution (microgrid configuration), LPSP is not zero then that solution was discarded. For all other solutions, LCOE and GHG emissions were computed and recorded.

5. RESULTS AND DISCUSSION

5.1. SCENARIO I: SINGLE HOME ANALYSIS

For a single home, the performance of ESA and GA techniques were compared with each other and the results are depicted in Table 4.

The upper and lower bound of variables for both the techniques (N_{PV} N_{WT} N_{LB} N_{BDG} N_{FC} N_{EM} N_{H2}) were set at (6 6 1 6 6 6 1) and (0 0 0 0 0 0 0) respectively.

The ESA evaluated each of these combinations (total of 67,228) before converging to the optimum (lowest cost) solution, while the GA evaluated only 7% of them.

Owing to this difference, the approximate run time for ESA was 60 minutes while that for GA was 3 minutes.

Both the ESA and the GA converged to the same set of solutions. The three lowest cost microgrid configurations for all the three cities are shown in Table 4.

The optimum configurations for Tucson and Lubbock show a greater preference towards PVs than WTs since the energy potential for solar is higher than that of wind (Figure 2) in those locations.

The converse is true for the case of Dickinson. Because the energy potential of wind is significantly higher than that of solar (Figure 2), the solutions show a greater preference towards WTs than PVs.

The configurations in all the cities show a same level of preference to BDGs which are in the range of 3-4 kW.

Furthermore, they also show a disinclination towards FCs and EMs due to their high costs.

Table 4 Performance analysis of ESA and GA for a single home

	Tucson, AZ	Lubbock, TX	Dickinson, ND
Maximum number of possible combinations	67,228	67,228	67,228
ESA performance statistics			
Number of combinations evaluated	67,228	67,228	67,228
Number of final set of solutions obtained	25,273	34,679	37,954
Run time (mins)	51	62	67
GA performance statistics			
Number of combinations evaluated	4481	4761	4271
Number of final set of solutions obtained	70	70	70
Number of generations of population	63	67	60
Run time (mins)	3.25	3.09	1.8

The analysis of monthly energy generated for the lowest cost microgrid configuration (solution no 1) for Tucson, Lubbock and Dickinson are shown in Figures 9, 10 and 11 respectively.

Table 5 Lowest cost microgrid configurations for all the three cities as predicted by ESA and GA

Solution Number	N_{PV} (kW)	N_{WT} (kW)	N_{LB} (of 22 kW each)	N_{BDG} (kW)	N_{FC} (kW)	N_{EM} (kW)	N_{H2} (kW)	LCOE ($/kWh)	GHG (kg CO_2 eq./year)
Tucson, AZ									
1	6	3	1	4	0	0	0	0.427	773
2	6	4	1	4	0	0	0	0.432	749
3	5	5	1	4	0	0	0	0.435	690
Lubbock, TX									
1	5	2	1	3	0	0	0	0.407	600
2	5	3	1	3	0	0	0	0.413	586
3	6	1	1	3	0	0	0	0.414	685
Dickinson, ND									
1	1	5	0	4	0	0	0	0.373	683
2	0	6	0	4	0	0	0	0.374	666
3	1	6	0	4	0	0	0	0.374	674

As shown in Table 5, the PV generation capacity of Tucson and Lubbock is 5-6 times as that of Dickinson, while their WT generation capacity is approximately half as that of Dickinson.

As a result the microgrids in Tucson (Figure 9) and Lubbock (Figure 10) were shown to generate about 65% and 35% of their energy via their PV and WT units respectively while in the case of Dickinson (Figure 11), the corresponding energy generation amounts were 7% and 82% respectively. For Tucson and Lubbock, the energy analyses also reveal that as a result of energy demand increase (from June to September), less energy is sold to the conventional grid and more energy is generated via backup sources (LB, BDG).
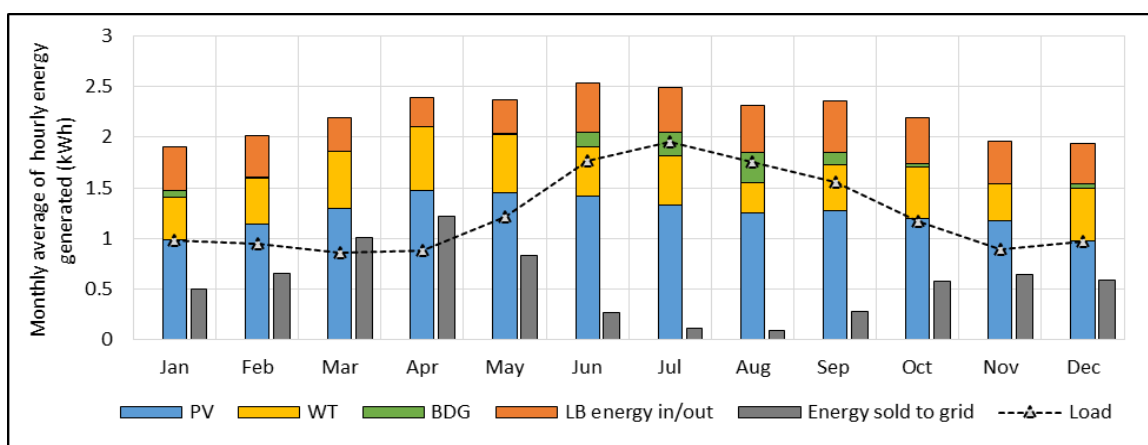
Figure 9 Analysis of monthly energy generated for the lowest cost microgrid configuration (solution #1) in Tucson, AZ

The amount of energy generated by individual component cannot be solely predicted from the value of its name plate capacity as it is also dependent on the EMS. For instance in the case of Tucson, even though the installed capacity of WT (3kW) was

lower than BDG (4kW), the total annual energy generated by WT was 6 times as that generated by BDG. This is because according to the EMS, WT is a primary source of power while BDG is an emergency source. For primary sources of energy (WT and PV), the energy produced is mainly dependent on the installed capacity while in case of emergency sources it is dependent on the difference in the values between energy generated by primary sources and the energy demand (energy deficit, ED).
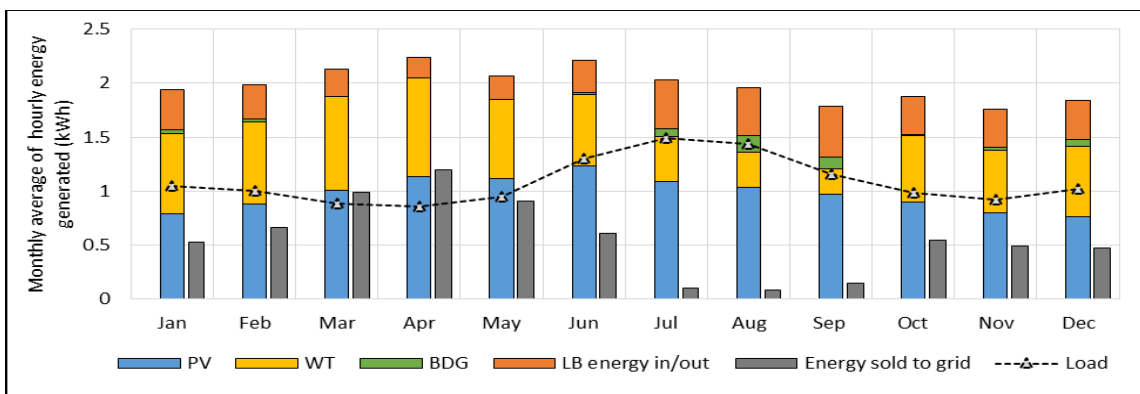
Figure 10 Analysis of monthly energy generated for the lowest cost microgrid configuration (solution #1) in Lubbock, TX
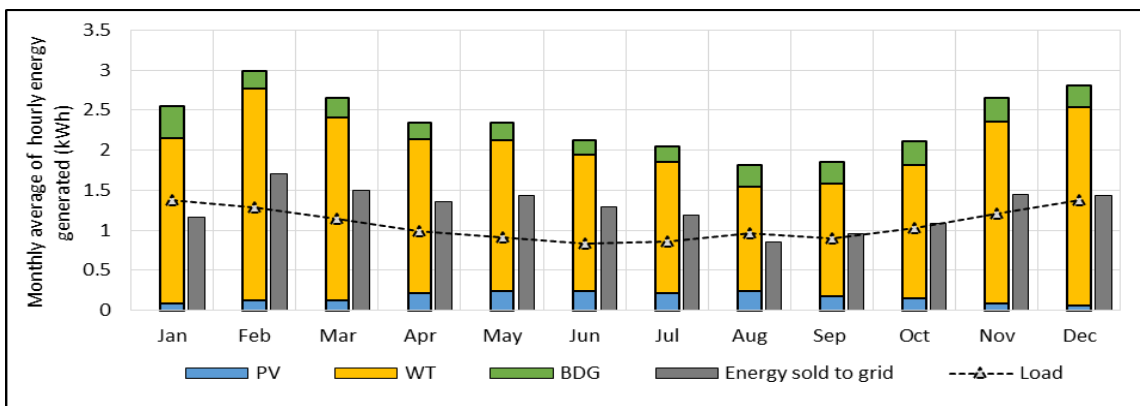
Figure 11 Analysis of monthly energy generated for the lowest cost microgrid configuration (solution #1) in Dickinson, ND

The LCOE ($/kWh) for individual components in the microgrid (solution no 1) for Tucson, Lubbock and Dickinson are shown in Figures 5.4, 5.5 and 5.6 respectively. For Tucson and Lubbock, the LCOE was 14% and 9% higher than that observed in Dickinson which can be attributed to two factors, namely, absence of LBs and high share of energy generation through WTs. LBs' absence caused a reduction in LCOE since the annualized cost of a single unit of battery (22 kWh capacity) is approximately 8 times as that of PV or WT. In addition to this, the share of energy generation (as % of total energy generated) through WT for Dickinson is approximately 2.5 times as that of Tucson or Lubbock. As energy generation through WTs is cheapest method of production available within microgrid (see Figures 9, 10, 11), the LCOE for Dickinson was found to be lowest among all the three cities.
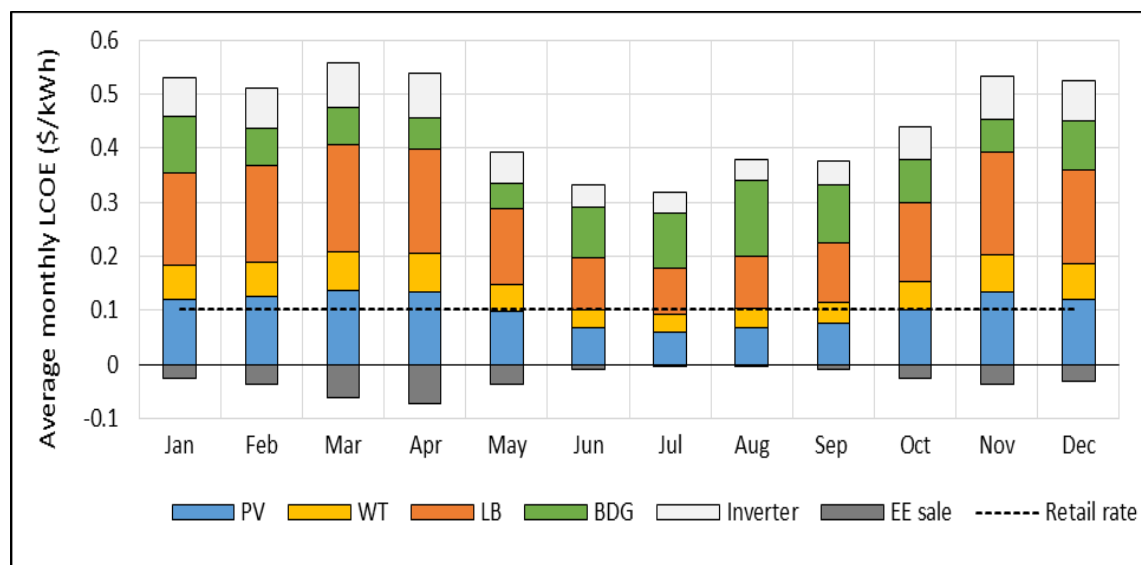
Figure 12 Component wise average monthly LCOE ($/kWh) for lowest cost microgrid configuration (solution #1) in Tucson, AZ

The net LCOE for all the three cities was found to be approximately 4 times as that of the retail rate of electricity in their respective states. Even though the net LCOE of the microgrid is significantly higher than the retail rate of electricity, the LCOE for individual components such as PV or WT may lie below it. For instance in Tucson and Lubbock, the average annual LCOE from WT alone is approximately 50% lower than the retail electricity rates in those locations respectively. Furthermore, for all the three cities, the annual average component LCOEs from PV ($0.071/kWh) and WT ($0.064/kWh) lie at the lower end of cost spectrum, while those from LB ($0.103/kWh) and BDG ($0.122/kWh) lie at the higher end. This is mainly because PV and WT, being the primary sources of energy, produce large amounts of energy while LB and BDG which act as emergency sources produce small amounts of energy (shown in Figures 12, 13 and 14). The purchase of biodiesel also contributes to the increase in costs for power generation through BDGs.
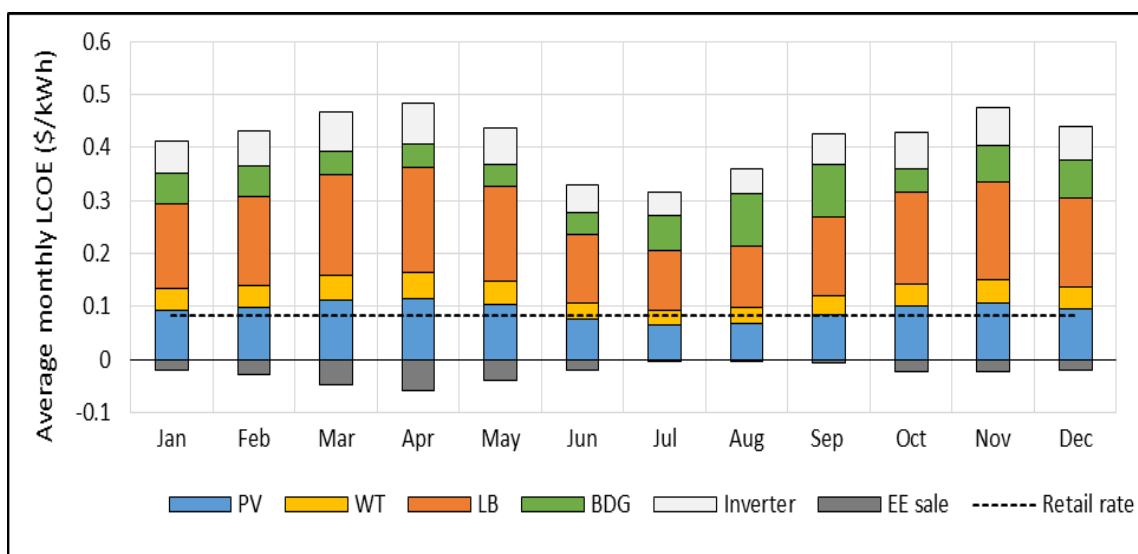
Figure 13 Component wise average monthly LCOE ($/kWh) for lowest cost microgrid configuration (solution #1) in Lubbock, TX

The sale of excess electricity to conventional grid does not significantly affect the net LCOE. For Tucson and Lubbock, it brings down the value of LCOE by only 6%, while for Dickinson the drop is 14%. The drop is more for Dickinson because its share of excess energy (as a share of net generated by PV and WT, which is eventually sold) generated is approximately 1.6 times as that of Tucson or Lubbock.
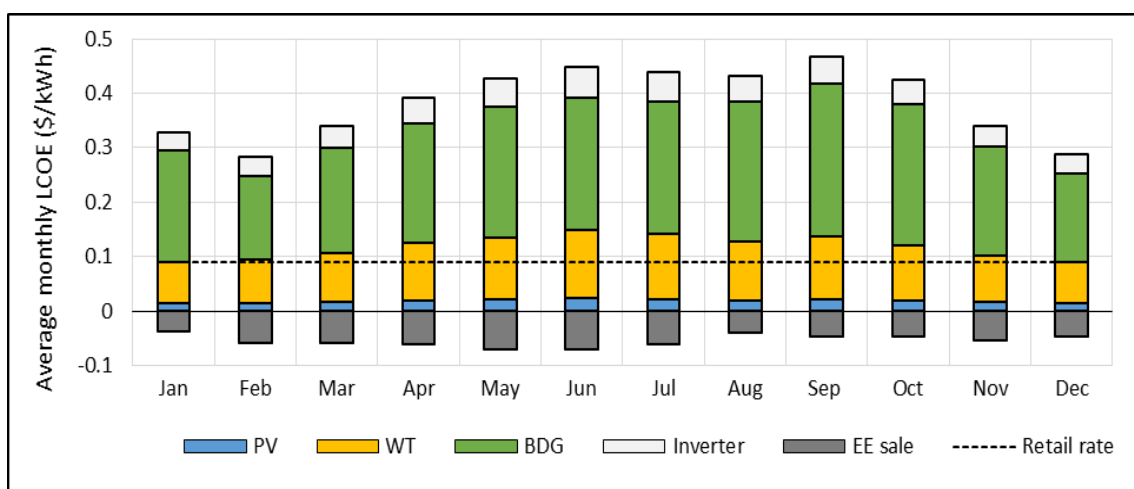
Figure 14 Component wise average monthly LCOE ($/kWh) for lowest cost microgrid configuration (solution #1) in Dickinson, ND

For the cities of Tucson, Lubbock and Dickinson, Figures 15, 16 and 17 depict the monthly LCA GHG emissions for the individual components of the microgrid along with their comparison with those emitted from a conventional electric grid respectively. For Tucson, Lubbock and Dickinson, the corresponding annual GHG emissions are 7, 8 and 11 times smaller than those emitted by their conventional electric grid equivalents.
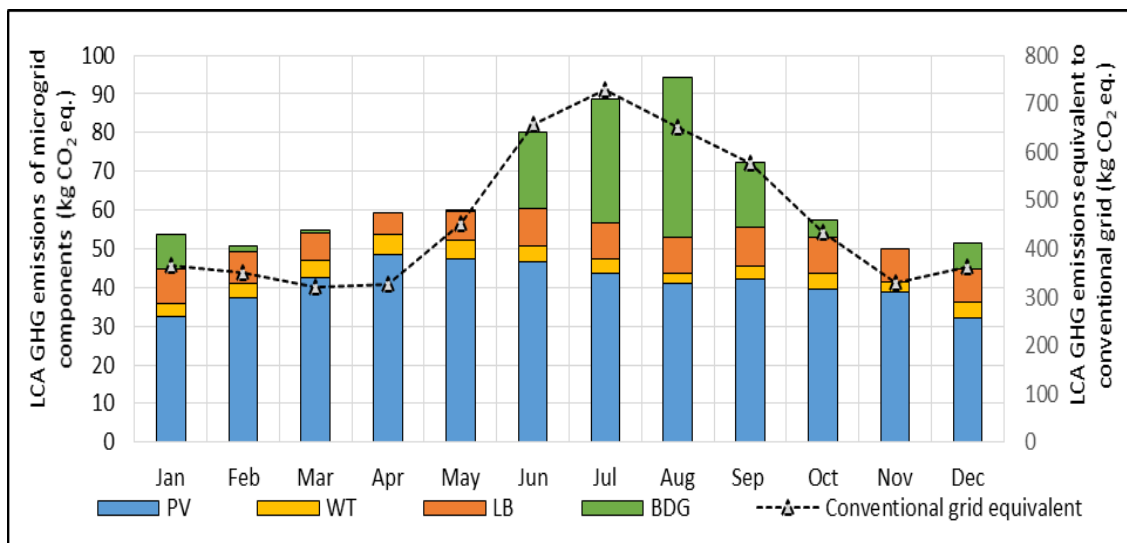
Figure 15 Monthly LCA GHG emissions (kg CO2 eq.) for lowest cost single home microgrid configuration (solution #1) in Tucson, AZ

The net emissions follow the electricity consumption patterns since they are directly proportional to the amount of energy generated by the microgrid. Additionally, they are also dependent on individual components' emission factors (Table 2). For Tucson and Lubbock, 64% of total annual emissions were attributed to PV component as it produced approximately 65% of their total annual energy. However in the case of Dickinson, even though 82% of total annual energy was generated by WTs, the share of annual emissions attributed to them was just 27%. The majority of emissions were attributed to energy production by BDGs (63%) although their annual share of energy generation was only 11%. This is because the emission factor (kg CO_2 emitted/kWh) of BDG is 17 times as that of WT (see Table 2).
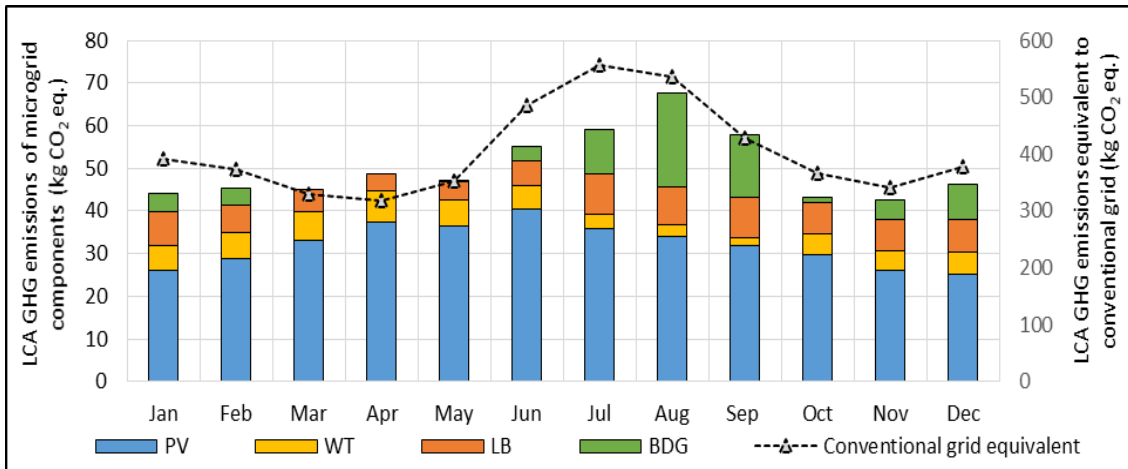
Figure 16 Monthly LCA GHG emissions (kg CO2 eq.) for lowest cost single home microgrid configuration (solution #1) in Lubbock, TX
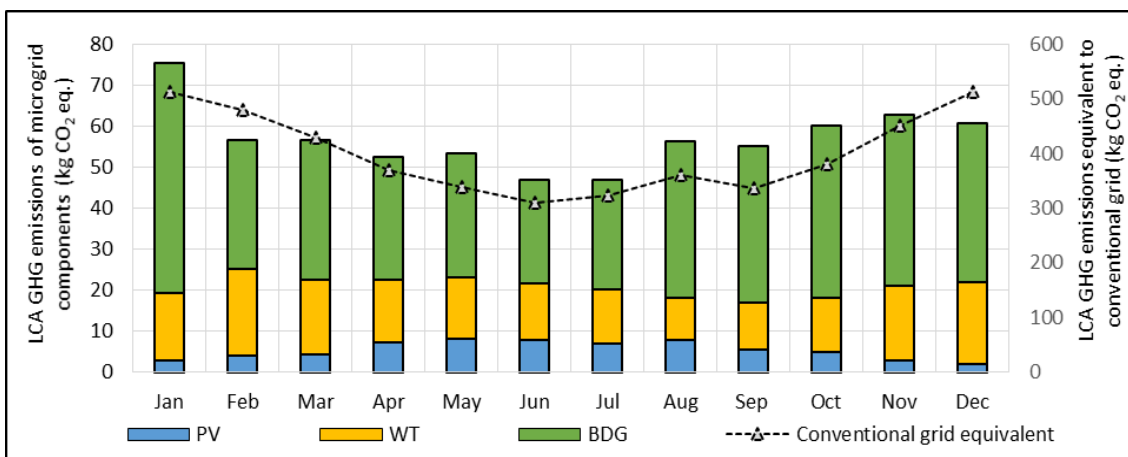
Figure 17 Monthly LCA GHG emissions (kg CO2 eq.) for lowest cost single home microgrid configuration (solution #1) in Dickinson, ND

5.2. SCENARIO II: TEN HOME ANALYSES

For ten home analyses, the upper bound of solution domain for variables (N_{PV} N_{WT} N_{LB} N_{BDG} N_{FC} N_{EM} N_{H2}) was set at (60 60 10 60 60 60 10) while the lower bound was set at zero. Within this solution space, a simple calculation revealed that the number

of possible integer combinations would be 1.02×10^{11}. The ESA technique would

approximately take 7.75×10^7 mins or 147 years to evaluate every combination before

determining the lowest cost microgrid configuration. It was shown previously (single

home analysis) that the GA converges to the optimum solution within fraction of the time

taken by the ESA while also maintaining high levels of accuracy. Therefore, in the case

of ten homes only GA was used to find the optimum solution.

Table 6 Performance analysis of GA for the case of ten homes

	Tucson, AZ	Lubbock, TX	Dickinson, ND
Maximum number of possible combinations	1.02×10^{11}	1.02×10^{11}	1.02×10^{11}
GA performance statistics			
Number of combinations evaluated	8191	10,501	7001
Number of solutions obtained	70	70	70
Number of generations	116	149	99
Run time (mins)	6.08	6.65	4.6

The performance of the GA was summarized in Table 6. The top three lowest

cost microgrid configurations for the three cities as predicted by the GA are depicted in

Table 7. Due to the increase in electricity demand by a factor of ten, the net generation

capacity also got expanded within the range of 8.5 to 10 for all the three cities.

Table 7 Lowest cost microgrid configurations for ten homes as predicted by GA

Solution Number	N_{PV} (kW)	N_{WT} (kW)	N_{LB} (of 22 kW each)	N_{BDG} (kW)	N_{FC} (kW)	N_{EM} (kW)	N_{H2} (kW)	LCOE ($/kWh)	GHG (kg CO_2 eq./year)
Tucson, AZ									
1	54	35	8	39	0	0	0	0.421	7864
2	54	34	8	39	0	0	0	0.421	7902
3	54	36	8	39	0	0	0	0.422	7828
Lubbock, TX									
1	37	35	4	29	0	0	0	0.378	6761
2	38	36	4	29	0	0	0	0.379	6786
3	37	37	4	28	0	0	0	0.387	6714
Dickinson, ND									
1	9	45	3	31	0	0	0	0.329	5269
2	10	45	3	31	0	0	0	0.329	5278
3	8	46	3	31	0	0	0	0.329	5246

The net GHG emissions also increased by a factor of 10, 11 and 8 for Tucson, Lubbock and Dickinson respectively. The energy distribution patterns for Tucson and Dickinson were similar to those of the single home and therefore are not shown here. However, these patterns were different for the case of Lubbock and are shown in Figure 18.

For Dickinson, the presence of LBs did not affect these patterns in a major way since only 6% of the total energy generated by PV and WT was stored in them. For Tucson, the share of energy generated by PV rose by 7% while that of WT and BDG fell by 5% and 2% respectively. The share of energy stored in LB also fell by 3%.

For Lubbock, the share of energy generated by PV (as a share of total energy generated by PV, WT, BDG) fell by 22% while that of WT and BDG rose by 20% and 2% respectively.
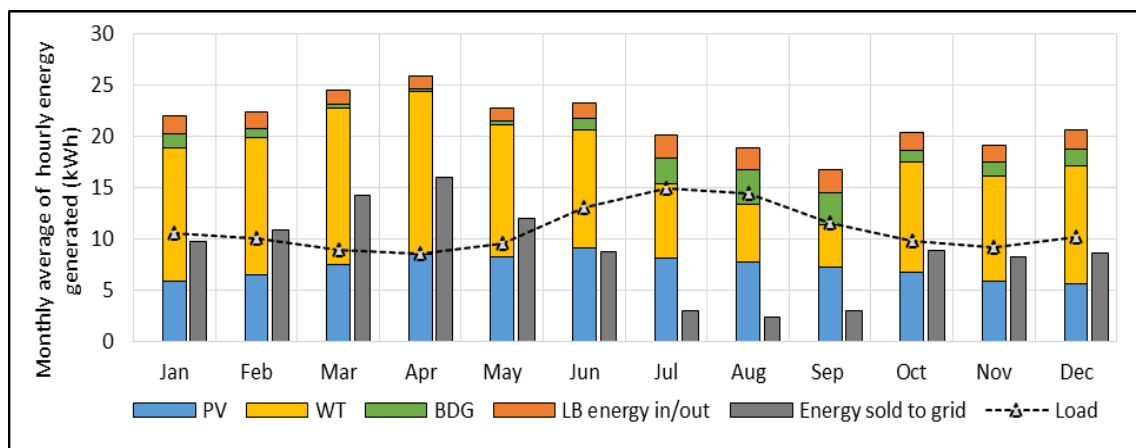
Figure 18 Analysis of monthly energy generated for lowest cost ten home microgrid configuration (solution #1) in Lubbock, TX

Furthermore, the share of energy stored in LB (as a share of total energy generated by PV and WT) also fell by 11%. As less energy was stored in LB, the share of excess energy sold to the grid (as a share of total energy generated by PV and WT) surged by 13%. These results for Lubbock indicate that, as microgrid size increases, greater preference was given to WTs than PVs while converse is true for the case of Tucson.

The LCOE for Lubbock and Dickinson are shown in Figures 19 and 20 respectively.

The cost analysis for Tucson was not shown here as it was similar to that of a single home.

Relative to single home case, the annual drop in net LCOE for Lubbock and Dickinson was 8% and 12% respectively.

For Lubbock, the drop was attributed to 25% and 65% decline in component LCOEs for PV and LB units respectively.

For Dickinson, the drop was attributed to 38% decline in LCOE for BDGs. It is interesting to note that the net LCOE drop in Dickinson occurred even after addition of capital intensive components (three LBs) to the microgrid.

Despite its drop in costs, the annual LCOE values for Lubbock and Dickinson were still 4.5 and 3.6 times as that of the retail costs respectively.
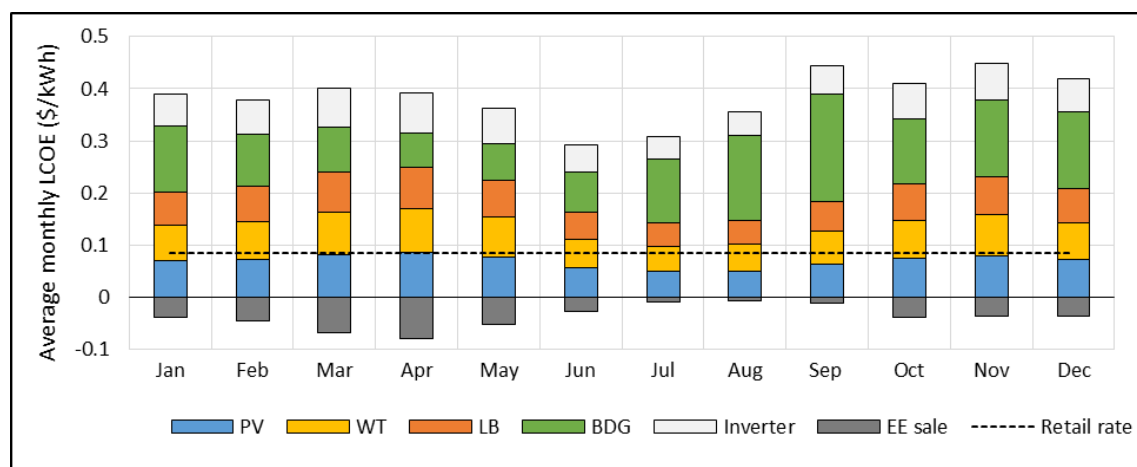
Figure 19 Average monthly LCOE ($/kWh) for lowest cost ten home microgrid configuration (solution #1) in Lubbock, TX
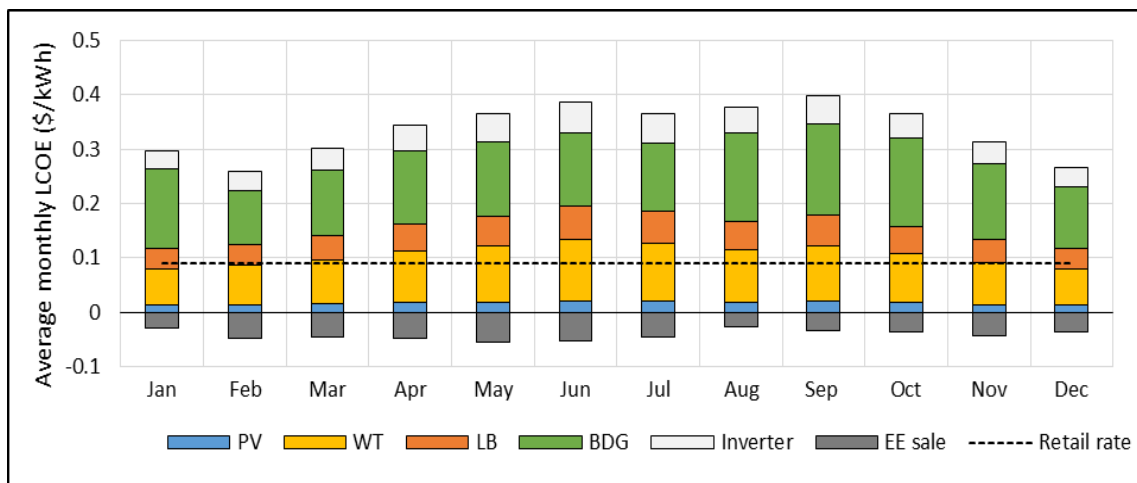
Figure 20 Average monthly LCOE ($/kWh) for lowest cost ten home microgrid configuration (solution #1) in Dickinson, ND

Figures 21, 22 and 23 illustrate the LCA GHG emissions for the lowest cost ten home microgrid configuration in Tucson, Lubbock and Dickinson respectively. Relative to the single home scenario, the net LCA GHG emissions approximately increased by a factor of 10, 11 and 8 times for Tucson, Lubbock and Dickinson respectively.
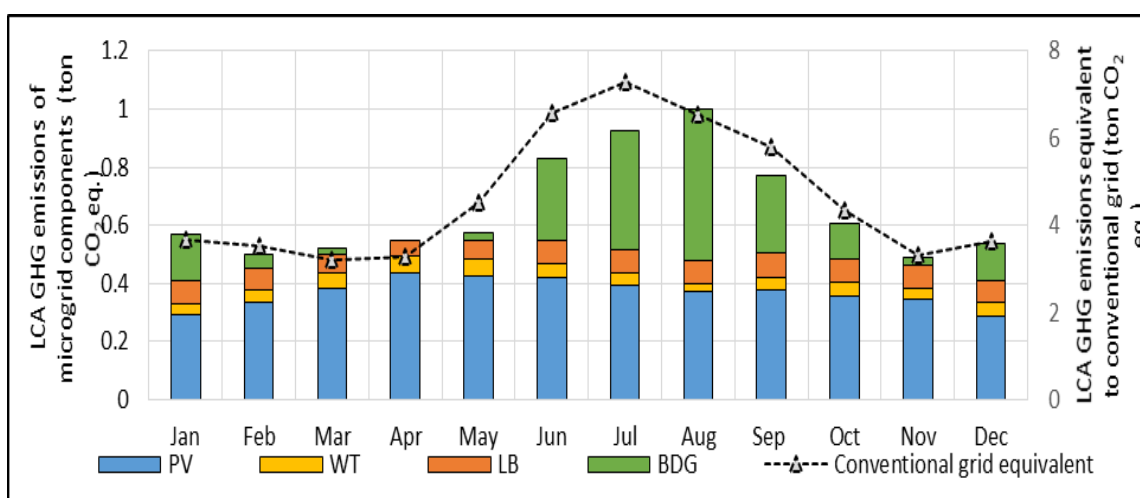
Figure 21 Monthly LCA GHG emissions (ton CO2 eq.) for lowest cost ten home microgrid configuration (solution #1) in Tucson, AZ
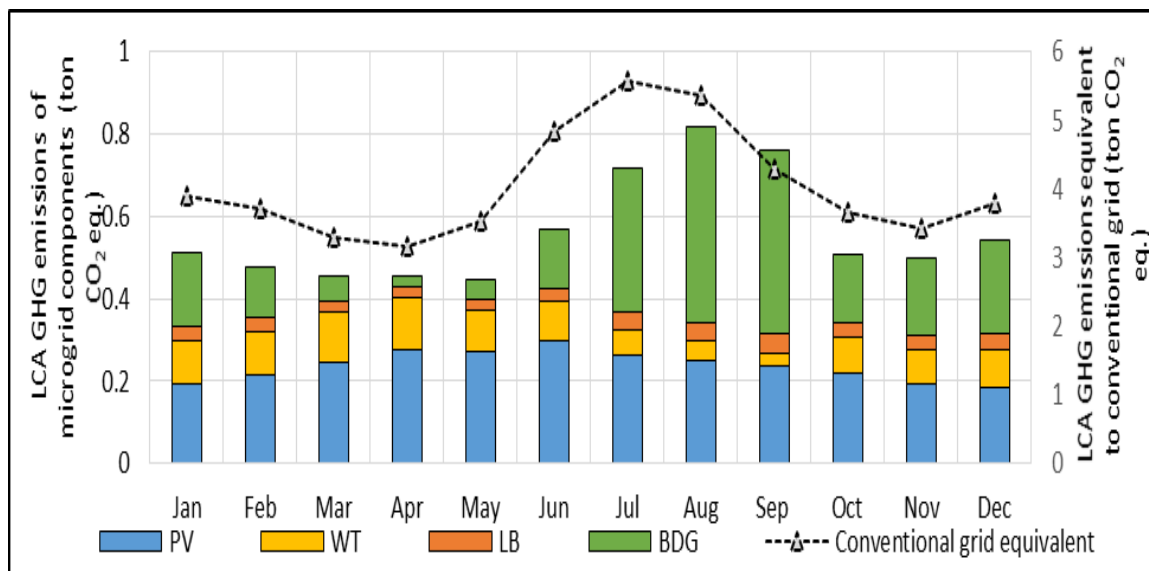
Figure 22 Monthly LCA GHG emissions (ton CO2 eq.) for lowest cost ten home microgrid configuration (solution #1) in Lubbock, TX

For Tucson and Lubbock, BDGs' share of total emissions increased by 12% and 24% while PVs' share decreased by 8% and 22% respectively. The corresponding emissions' share of LB in these cities also fell by 5% and 7%. In case of Dickinson, the share of PV, WT and LB in total emissions increased by 2%, 5% and 5% respectively at the expense of BDG's share.

These results indicate that as microgrid size is increased, the share of individual components' emissions changes and nature of this change is dependent on microgrid's location.

For Tucson, Lubbock and Dickinson, the corresponding annual GHG emissions are 7, 8 and 9 times smaller than those emitted by their conventional electric grid equivalents.
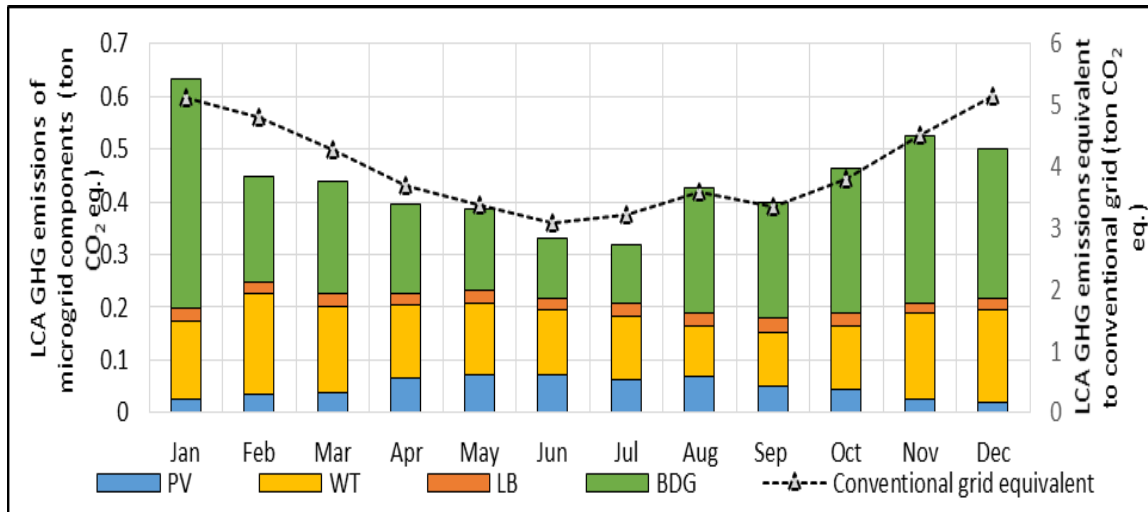
Figure 23 Monthly LCA GHG emissions (ton CO2 eq.) for lowest cost ten home microgrid configuration (solution #1) in Dickinson, ND

5.3. SCENARIO III: FIFTY HOME ANALYSES

For fifty home analyses, the upper bound of solution domain for variables (N_{PV} N_{WT} N_{LB} N_{BDG} N_{FC} N_{EM} N_{H2}) was set at (300 300 50 300 300 300 50) while the lower bound was set at zero. Within this solution space, the number of possible integer combinations were found to be 6.42×10^{15}.

Based on the single home analyses, the ESA technique would approximately take 4.78×10^{12} mins or 9.09×10^{6} years to evaluate every combination before determining the lowest cost microgrid configuration.

It was shown also previously that the GA converges to the optimum solution within fraction of the time taken by the ESA while maintaining high levels of accuracy. Therefore, in the case of fifty homes only GA was used to find the optimum solution. The performance of the GA is summarized in Table 8.

Table 8 Performance analysis of GA for the case of fifty homes

	Tucson, AZ	Lubbock, TX	Dickinson, ND
Maximum number of possible combinations	6.42×10^{15}	6.42×10^{15}	6.42×10^{15}
GA performance statistics			
Number of combinations evaluated	10,991	20,651	10,781
Number of solutions obtained	70	70	70
Number of generations	156	294	153
Run time (mins)	7.7	14.73	6.66

The top three lowest cost microgrid configurations for all the cities as predicted by the GA are depicted in Table 9. As compared to the single home scenario, increasing the electricity demand by a factor of fifty caused the net generation capacity of the microgrid to increase by a similar factor. There was not much difference observed in the LCOEs for ten home and fifty home microgrids. The net GHG emissions increased by a factor of 50, 57 and 38 for Tucson, Lubbock and Dickinson respectively when compared with the single home scenario. For all the cities, the share of energy generation, emissions and LCOE values of individual microgrid components for lowest cost configuration (solution no. 1) are approximately similar to that of the ten homes scenario. In case of Lubbock, it is interesting to note the presence of FCs and H_2 tanks in lowest cost microgrid configurations numbered 2 and 3 (Table 9). These results suggest that as microgrid size increases, it might be actually cheaper to generate energy from FCs than

from any other sources thereby demonstrating an economies of scale effect. The LCOEs

for all the three scenarios (1, 10 and 50 homes) mentioned above were in the range of

$0.32 - 0.42 /kWh. Furthermore, the sale of surplus amount of electricity did not have a

major economic impact as it lowered the LCOE by only 7 - 15%.

Table 9 Lowest cost microgrid configurations for fifty homes as predicted by GA

Solution Number	N_{PV} (kW)	N_{WT} (kW)	N_{LB} (of 22 kW each)	N_{BDG} (kW)	N_{FC} (kW)	N_{EM} (kW)	N_{H2} (kW)	LCOE ($/kWh)	GHG (kg CO_2 eq./year)
Tucson, AZ									
1	277	172	43	192	0	0	0	0.419	38,760
2	278	173	43	192	0	0	0	0.419	38,763
3	277	173	43	192	0	0	0	0.419	38,725
Lubbock, TX									
1	185	188	18	143	0	0	0	0.377	34,432
2	195	253	18	148	3	0	1	0.393	34,234
3	190	191	18	166	2	0	1	0.395	34,636
Dickinson, ND									
1	49	213	17	152	0	0	0	0.326	25,812
2	49	214	17	152	0	0	0	0.326	25,792
3	48	214	17	152	0	0	0	0.326	25,784

The LCOEs were approximately 3.5 - 4.5 times as that of retail cost of electricity in their respective cities. Even though it might not be economically feasible to build a microgrid in these cities, there might be an economic case for cities that have higher electricity retail rates. For instance, in 2017 the average retail electricity price in the state of Hawaii was $0.26 /kWh [44]. Microgrids would relatively become more economically competitive and feasible in such states. A detailed economic analysis would be needed to ascertain the economic feasibility.

One of the drawbacks of this work is that it can only conduct the techno-economic and environmental assessment of a small scale microgrid (up to 50 homes). To perform the analyses for larger capacity, the economic costs need to be correspondingly adjusted to those of a larger scale (or utility scale).

5.4. COMPARISON OF ECONOMIC ANALYSIS RESULTS WITH SIMILAR STUDIES IN LITERATURE

The economic results obtained in this work are similar to those recently reported in the literature regarding small scale microgrids with the exclusion of any subsidies. The comparison of LCOE (adjusted to 2018$ value) with those available in literature are shown in Table 10. It should be noted that the LCOE for microgrid is calculated on the basis of local acquisition (capital) costs of the individual components. These costs can significantly differ from country to country. However, this comparison is valuable as it can give an insight regarding the economic feasibility of microgrids in the US and also across the world. Ensuring global economic feasibility is essential in order to tackle the common environmental conundrum of anthropogenic climate change.

Table 10 Comparison of LCOE (adjusted to 2018$) with other studies available in the literature focusing on small scale microgrids

Sr No.	Microgrid components	Location	LCOE ($/kWh)	Reference
1.	PV-WT-LB-BDG-FC-H_2	US	0.32 - 0.42	This study
2.	PV-WT-DG	Singapore	0.19 – 0.30	[6]
3.	PV-WT-DG-LB	Saudi Arabia	0.05 - 0.08	[9]
4.	PV-WT-DG-LB	India	0.27 - 0.3	[10]
5.	PV-WT-FC	Iran	0.55 – 0.81	[8]

6. CONCLUSIONS

In this work, a methodology was developed that assessed the technical, economic and environmental performance of a small scale microgrid composed of seven components, namely, PV, WT, LB, BDG, FC, EM and H2 tanks. This methodology was implemented for US cities of Tucson, Lubbock and Texas.

The main conclusions of this study are as follows:

1. Based on the regional electricity load profile and availability of renewable sources, an optimum configuration of a standalone microgrid was determined that had the lowest LCOE using a stochastic optimization algorithm known as GA. The results of the GA for a single home microgrid were verified using a brute force method (ESA) for the case of single home.

2. Scaling up the microgrid size (1 to 10 homes) reduced the LCOE by 7-12% thereby demonstrating the economies of scale effect.

3. Neglecting financial subsidies, the LCOEs were in the range of $0.32 - 0.42 /kWh and were approximately 3.5 - 4.5 times as that of their local retail electricity cost.

4. The average individual component LCOE values for lowest cost microgrid configurations for PV ($0.066/kWh) and WT ($0.07/kWh) were found to lie at the lower end of cost spectrum while those for LB ($0.0866/kWh) and BDG ($0.119/kWh) were found to lie at the higher end.

5. The environmental footprint of microgrid was found to be extremely low as they were found to be approximately 1/10th as those emitted by an equivalent conventional electric grid.

Future work should be carried out to determine the economic feasibility for a utility scale microgrid that incorporates the social cost ($/ton) of carbon which is a measure of long term economic damage done by CO_2 emissions. Such an assessment that incorporates the technical, economic and environmental aspects would serve as a firm basis that would aid lawmakers in shaping energy and environmental policies of the future.

REFERENCES

1. http://www.iea.org/publications/freepublications/publication/KeyWorld2017.pdf [Accessed May 7, 2018]

2. J Jung, M Villaran; Optimal planning and design of hybrid renewable energy systems for microgrids; Renew Sust Energy Rev 2017; 70:180-191. DOI: https://doi.org/10.1016/j.rser.2016.10.061

3. Bagen, Billington R. Evaluation of different operating strategies in small stand alone power systems. IOEEE Trans Energy Convers 2005; 20(3):654-60. DOI: 10.1109/TEC.2005.847996

4. De Bosio F, Luna AC, Ribeiro L, Graells M, Saavedra OR, Guerrero JM. Analysis and improvement of the energy management of an isolated microgrid in Lencois island based on a linear optimization approach, IEEE; 2016. DOI: 10.1109/ECCE.2016.7854871

5. A Maleki, A Aksarzadeh. Artificial bee swarm optimization for optimum sizing of a stand-alone PV/WT/FC hybrid system considering LPSP concept. Solar Energy 2014; 107:227-235. DOI: https://doi.org/10.1016/j.solener.2014.05.016

6. C Shang, D Srinivasan T Reindl. An improved particle swarm optimization algorithm applied to battery sizing for stand alone hybrid energy power systems. Electrical Power and Energy systems 2016; 74:104-117. DOI: https://doi.org/10.1016/j.ijepes.2015.07.009

7. A Maleki, M G Khajeh, M Ameri; Optimal sizing of a grid independent hybrid renewable energy system incorporating resource uncertainty, and load uncertainty 2016; 83:514-524. DOI: https://doi.org/10.1016/j.ijepes.2016.04.008

8. R Hosseinalizadeh, H Shakouri, M Amalnick, P Taghipour; Economic sizing of a hybrid (PV-WT-FC) renewable energy system (HRES) for standalone usages by an optimization simulation model: Case study of Iran; Renew Sust Energy Rev 2016, 54:139-150. DOI: https://doi.org/10.1016/j.rser.2015.09.046

9. MAM Ramli, HREH Bouchekara, AS Alghamdi. Optimal sizing of PV/wind/diesel hybrid microgrid system using multi-objective self-adaptive differential evolution algorithm, Renew Energy 2018; 121:400-411. DOI: https://doi.org/10.1016/j.renene.2018.01.058

10. C Phurailatpam, BS Rajpurohit, L Wang. Planning and optimization of autonomous DC microgrids for rural and urban applications in India. Renew Sust Energy Rev 2018, 82:194-204. DOI: https://doi.org/10.1016/j.rser.2017.09.022

11. R Dufo-Lopez, JL Agustin. Multi-objective design of PV-wind-diesel-hydrogen-battery systems. Renew Energy 2008, 33:2559-2572. DOI: https://doi.org/10.1016/j.renene.2008.02.027

12. YA Katsigiannis, PS Georgilakis, ES Karapidakis. Multiobjective genetic algorithm solution to optimum economic and environmental performance problem of small autonomous hybrid power systems with renewables. IET Renew Power Gener 2010, 4(5),404-419. DOI: 10.1049/iet-rpg.2009.0076.

13. X Pelet, D Favrat, Leyland G. Multiobjective optimization of integrated energy systems for remote communities considering economics and CO_2 emissions. Int J Thermal Sci 2005, 44 (12), 1180-89. DOI: https://doi.org/10.1016/j.ijthermalsci.2005.09.006

14. MD Somma, G Graditi, EH Forushani, M Shafie-khah, P Siano. Stochastic optimal scheduling of distributed energy resources with renewables considering economic and environmental aspects, Renew Energy 2018, 116, 272-287. https://doi.org/10.1016/j.renene.2017.09.074

15. A Rezvani, M Gandomkar, M Izadbakhsh, A Ahmadi. Environmental/economic scheduling of a micro-grid with renewable energy resources. Journal of Cleaner Production 2015, 216-226. https://doi.org/10.1016/j.jclepro.2014.09.088

16. M Elsied, A Oukaour, H Gualous, OAL Brutto. Optimal economic and environment operation of micro-grid power systems. Energy Conversion and Management 2016, 122, 182-194. https://doi.org/10.1016/j.enconman.2016.05.074

17. A Lyden, R Pepper, P Tuohy. A modeling tool selection process for planning of community scale energy systems including storage and demand side management, Sustainable cities and Society 2018, 39, 674-688. DOI: https://doi.org/10.1016/j.scs.2018.02.003

18. https://rredc.nrel.gov/solar/old_data/nsrdb/1991-2005/tmy3/by_state_and_city.html [Accessed May 7, 2018]

19. Iqbal M. An introduction to solar radiation, Canada Academic Press, 1983, ISBN 0-12-373752-4.

20. De Miguel A, Bilbao J, Aguiar R, Kambezidis H, Negro E. Diffuse solar model evaluation in the North Mediterranean belt area. Sol Energy 2001; 70(2):143-53. DOI: https://doi.org/10.1016/S0038-092X(00)00135-3

21. T. M. Klucher, "Evaluation of models to predict insolation on tilted surfaces," Solar Energy, vol. 23, no. 2, pp. 111–114, 1979. DOI: https://doi.org/10.1016/0038-092X(79)90110-5

22. System Advisor Model Version 2017.1.17 (SAM 2017.1.17). National Renewable Energy Laboratory. Golden, CO. [Accessed May 7, 2018]

23. JA Duffie, W Beckman, Solar Engineering of Thermal Processes, 2013, Wiley, ISBN 978-1-118-43348-5

24. Tina G, Gagliano S, Raiti S. Hybrid solar/wind power system probabilistic modelling for long-term performance assessment. Solar Energy 2006, 80:578-88. DOI: https://doi.org/10.1016/j.solener.2005.03.013.

25. S Diaf, G Notton, M Belhamel, M Haddadi, A Louche, Design and techno-economical optimization for hybrid PV/wind system under various meterological conditions, Applied Energy 2008, 85:968-987. DOI: https://doi.org/10.1016/j.apenergy.2008.02.012

26. M.Mohammadi, S.H.Hosseinian, G.B.Gharehpetian. Optimization of hybrid solar energy sources/wind turbine systems integrated to utility grids as microgrid (MG) under pool/bilateral/hybrid electricity market using PSO. Solar Energy 2012, 86:112-125. DOI: https://doi.org/10.1016/j.solener.2011.09.011

27. https://www.nrel.gov/grid/wind-toolkit.html [Accessed May 7, 2018]

28. C Zhang, Y Wei, PF Cao, MC Lin, Energy storage system: Current studies on batteries and power condition system, Renew Sustain Ener Rev 2018, 82:3091-3106. DOI: https://doi.org/10.1016/j.rser.2017.10.030

29. O Gergaud, G Robin, B Multon, HB Ahmed. Energy Modeling of a Lead-Acid Battery within Hybrid Wind/Photovoltaic Systems. European Power Electronic Conference 2003, Sep 2003, TOULOUSE, France. 8pp, 2003.

30. D Guasch, S Silvestre. Dynamic battery model for photovoltaic applications, Prog. Photovolt: Res. Appl. 2003; 11:193–206, DOI: 10.1002/pip.480

31. R Chen, Z Qin, J Han, M Wang, F Taheripour, W Tyner, D O'Conner, J Duffield. Life cycle energy and greenhouse gas emission effects of biodiesel in US with induced land change impacts, Bioresource technology, 251, 2018 249-258. DOI: https://doi.org/10.1016/j.biortech.2017.12.031

32. OS Valente, MJ Silva, VMD Pasa, CRP Belchior, JR Sodré. Fuel consumption and emissions from a diesel power generator fuelled with castor oil and soybean biodiesel. 2010. Fuel. 89:3637-3642. DOI: https://doi.org/10.1016/j.fuel.2010.07.041

33. S. Yerramalla, A. Davari, A. Feliachi, T. Biswas Modeling and simulation of the dynamic behavior of a polymer electrolyte membrane fuel cell, J Power Sources, 124 (1) (2003), pp. 104-113. DOI: https://doi.org/10.1016/S0378-7753(03)00733-X

34. Z Abdin, CJ Webb, EMA Gray. PEM fuel cell model and simulation in Matlab-Simulink based on physical parameters 2016. Energy 116:1131-1144. DOI: 10.1016/j.energy.2016.10.033

35. https://www.iea.org/publications/freepublications/publication/essentials6.pdf

36. AHA Rahim, AS Tijani, SK Kamarudin, S Hanapi. An overview of polymer electrolyte membrane electrolyzer for hydrogen production: Modeling and mass transport, Journal of Power Sources 2016, 309:56-65. DOI: https://doi.org/10.1016/j.jpowsour.2016.01.012

37. CH Li, XJ Zhu, GY Cao, S Sui, MR Hu. Dynamic modeling and sizing optimization of standalone photovoltaic power systems using hybrid energy storage technology. Renewable energy 2009, 34:815-26. DOI: https://doi.org/10.1016/j.renene.2008.04.018

38. https://openei.org/datasets/files/961/pub/RESIDENTIAL_LOAD_DATA_E_PLUS_OUTPUT/BASE/ [Accessed May 7, 2018]

39. R Dufo-Lopez, JL Bernal Agustin, F Mendoza. Design and economical analysis of hybrid PV-wind systems connected to the grid for the intermittent production of hydrogen. Energy policy. 2009. 37:3082-3095. DOI: https://doi.org/10.1016/j.enpol.2009.03.059

40. https://www.afdc.energy.gov/fuels/prices.html [Accessed May 7, 2018]

41. www.wholesalesolar.com/[Accessed May 7, 2018]

42. https://www.absolutegenerators.com/american-built/watts/2000-3999-watts/fuel-type/diesel [Accessed May 7, 2018]

43. http://www.fuelcellstore.com/fuel-cell-stacks/high-power-fuel-cell-stacks [Accessed May 7, 2018]

44. http://www.airgas.com/p/HY%20300 [Accessed May 7, 2018]

45. http://www.praxair.com/-/media/corporate/praxairus/documents/specification-sheets-and-brochures/gases/hydrogen/hydrogen-h2-spec-sheet-ss-p4604.pdf?la=en [Accessed May 7, 2018]

46. Greenhouse gases, Regulated Emissions, and Energy use in Transportation Model. (GREET Version 2016.1.3.0.13245). UChicago Argonne Laboratory. [Accessed May 7, 2018]

47. http://www.neo.ne.gov/statshtml/204.htm [Accessed May 7, 2018]

48. A Mahesh, KS Sandhu, A genetic algorithm based improved optimal sizing strategy for solar-wind-battery hybrid system using energy filter algorithm, Front Energy, 2017, 1-13. DOI: https://doi.org/10.1007/s11708-017-0484-4

49. DE Goldberg, Genetic algorithms in search optimization and machine learning, Addison Wesley, 1989.

II. TECHNO-ECONOMIC OPTIMIZATION AND SOCIAL COSTS ASSESSMENT OF MICROGRID USING GENETIC ALGORITHM AND ARTIFICIAL NEURAL NETWORKS

Prashant Nagapurkar[a], Joseph D. Smith[a]

[a]Chemical and Biochemical Engineering department, Missouri University of

Science and Technology, Rolla-65401,MO, USA.

ABSTRACT

A methodology is presented that assessed the techno-economic and environmental

performance of a microgrid (MG) integrated with conventional grid (CG) for a residential

community (fifty homes) located in US cities of Fargo and Phoenix. The MG was

composed of seven components - solar photovoltaics, wind-turbines, lead acid batteries,

biodiesel generators, fuel cells, electrolyzers and H2 tanks. Firstly, mathematical models

that predicted the hourly power generation were developed for each of the MG

components. Secondly, Artificial Neural Network was utilized to predict hourly

electricity demand and its results were validated with actual available data. Thirdly,

through an electricity dispatch strategy and an optimization method (Genetic Algorithm),

MG configurations were determined that had lowest levelized cost of energy, LCOE

($/kWh). From peak power standpoint, four MG-CG integration scenarios were examined

(MG penetration level - 25%, 50%, 75%, 100%). Based on the environmental life cycle

assessment (LCA) of power generation, carbon taxes imposed were $12, $48, $72/tonne

CO_2. MG's LCOE was found to be $0.43-0.86/kWh. Imposing carbon taxes barely

showed any effect on MG's LCOE or its optimum configuration, but CG's electricity rate

($/kWh) was found to increase by 7-33% as CO2 emissions of CG were five times as that of MG.

HIGHLIGHTS

- Techno-economic optimization, environmental analysis (LCA) of microgrid (50 homes).

- Artificial Neural Network accurately predicted hourly power demand of 2 US cities.

- 4 MG-CG integration scenarios were examined (MG penetration – 25%, 50%, 75%, 100%).

- 3 carbon taxes (CT) imposed on each integration scenario - $12, $48, $72/tonne CO2.

- CT barely affected MG's LCOE ($/kWh) but CG's rate increased by 7-33% due to CT.

1. INTRODUCTION

The US is heavily reliant on fossil fuels to meet its power demand. In 2017, about 62% of the total demand was met via the combustion of coal and natural gas [1]. As a direct consequence of this, the annual carbon dioxide (CO2) emissions were nearly 5 million metric tons which constituted to about one third of the total US energy related emissions [2]. CO2, being a greenhouse gas pollutant has shown to negatively affect the human health and the environment. Therefore, there is an imminent need to curb CO2

emissions, and with regards to power generation it can be done by utilizing renewable energy sources such as solar photovoltaics (PV) and wind turbines (WT) that have a small carbon footprint. According to cradle to grave life cycle analyses (LCA) of power generation technologies, in order to produce the same amount of electricity, coal and natural gas powered electric grid emit 20 times and 10 times more greenhouse gases (GHG) than PV, WT or nuclear technologies respectively [3]. Despite their clean method of production one of main challenges of renewable sources is their generation intermittency as they are dependent on weather conditions. For instance, power production through PV is dependent on unpredictable weather phenomena such as solar radiation and cloud cover. This intermittency causes a mismatch between production and power consumption [4]. Several solutions have been proposed to address this mismatch. From the energy consumption standpoint, the demand can adjusted to meet the generation amount [5]. From the standpoint of energy generation, using diverse sources such as PV, WT, diesel generators (DG), fuel cells (FC), etc. that complement each other can be utilized to minimize the mismatch [6]. Another solution is to use energy storage units such as batteries, capacitors, etc. which can be used during periods of high electricity demand [4,7].

The solutions pertaining to energy generation and storage can be integrated together in a 'microgrid' (MG) which can be defined as a group of interconnected energy generation, storage and consumption units that can operate in conjunction with the conventional grid (CG) or in a standalone mode [8,9]. However, in order to maximize reliability and minimize cost the MG needs to be optimally sized. There exists analyses in the literature that have conducted such optimization studies based on regional electricity

demand and availability of renewable resources. For instance using a self-adaptive differential algorithm, Ramli et al sized an optimal microgrid that was composed of PV, WT, DG and batteries for city of Yanbu in Saudi Arabia [10]. For rural and urban applications, similar analysis was conducted to optimally size a microgrid in India that had the least cost and which comprised of PV, WT and biodiesel generators (BDG) using HOMER software [11].

In the literature, few studies examined the impact of social cost of CO2 emissions (SCC) or carbon tax on electricity cost. Anestis et al studied the effect of SCC (15 €/tonne CO2 – 200 €/tonne CO2) on the electricity costs for a microgrid that provided power to a hotel in Greece (using GAMS software) [12]. Even though the authors incorporated carbon taxes in their study, the microgrid was assumed to comprise of only one renewable component (PV). Furthermore, they used only simple efficiency based models to predict PV's power output. Similar study was conducted by Mehleri et al for a residential center in Greece, where only PV unit was modeled using DER-CAM software tool and while also including an SCC of 17 €/ton CO2 [13].

The current electricity generation infrastructure is predominantly fossil fuel based. For renewables to displace them, there is a need to examine effect of renewable energy (or microgrid) penetration on cost and emissions. This is one of the main motives of present work. There exist studies in the literature which examine the effects of integration of renewable energy sources with conventional grid. For instance, Denholm et al. have analyzed different scenarios where WT, PV and concentrating solar could provide up to 80% of grid demand for US electric grid [14]. This work was extended by incorporating nuclear energy (as a generation source) and thermal energy (as storage) to explore

different combinations of wind, solar and nuclear that can maximize overall efficiency thereby minimizing losses [15]. Similar study was conducted for an electric grid in France where different scenarios of PV and WT integration (up to 50%) with nuclear energy were explored and its subsequent effect on LCOE was computed. Even though this study reported losses due to high penetration of renewable sources, the economic feasibility was shown to significantly improve by the inclusion of carbon tax (>100 €/tonne CO2) [16]. Aforementioned works did not conduct a cost optimization of renewable energy penetration [14-16]. A study conducted by Shang et al used improved particle swarm optimization (PSO) technique to minimize costs, sized a microgrid that was composed of PV, WT and DGs [17]. Even though different levels of renewable penetration levels were analyzed in this study, the authors designed a standalone microgrid that was not connected with the conventional grid and also excluded carbon tax. One of the common themes of previously mentioned works was that current grid scale electricity generation sources that is coal (with carbon capture and sequestration), natural gas and nuclear are extremely economical when they are utilized to fulfill baseload electric demand [14-16]. However, when they are utilized to fulfil peak power demand their costs surges by a factor of 4-6. [18,19]. None of the above referenced studies focused on the economic feasibility of renewable energy penetration when compared with peak power while including carbon tax impact.

Most of the studies in the literature on sizing and optimization of microgrids used a predefined hourly load for the entire year. For instance, Maleki et al. [20] and Hosseinalizadeh et al. [21] used typical hourly load profiles for sizing their microgrid designs in Iran. Similar predefined hourly loads were assumed by Phurailatpam et al. to

optimally size a microgrid for rural and urban microgrids in India [11]. None of the studies used any forecasting methodology to predict the electricity load. The accurate prediction of energy consumption in residential and commercial buildings is extremely vital to microgrid sizing and optimization. These methods can be tremendously beneficial in the absence of consumption data.

The present work addresses all the previously mentioned research gaps and provides five novel contributions which are as follows:

Develop a methodology that conducts a techno-economic and environmental assessment for microgrid that is composed of PV, WT, LB, FC, BDG, EM and H2 tanks and that can power a small residential community of fifty homes. This methodology was implemented for two US cities and a comparison of results was also made.

- Utilize artificial neural network to predict electricity demand of the two US cities and validate it using actual available data.

- Examine the electricity cost (LCOE) along with CO2 emissions for each of the four scenarios of MG-CG integration (from peak power standpoint), namely, 25%, 50%, 75% and 100%.

- For every grid integration scenario, optimally size a MG to find a lowest LCOE ($/kWh) configuration using genetic algorithm.

- Impose three levels of carbon taxes ($12, $48, $72 per tonne CO2) and examine their impact on electricity cost and CO2 emissions for every grid integration scenario.
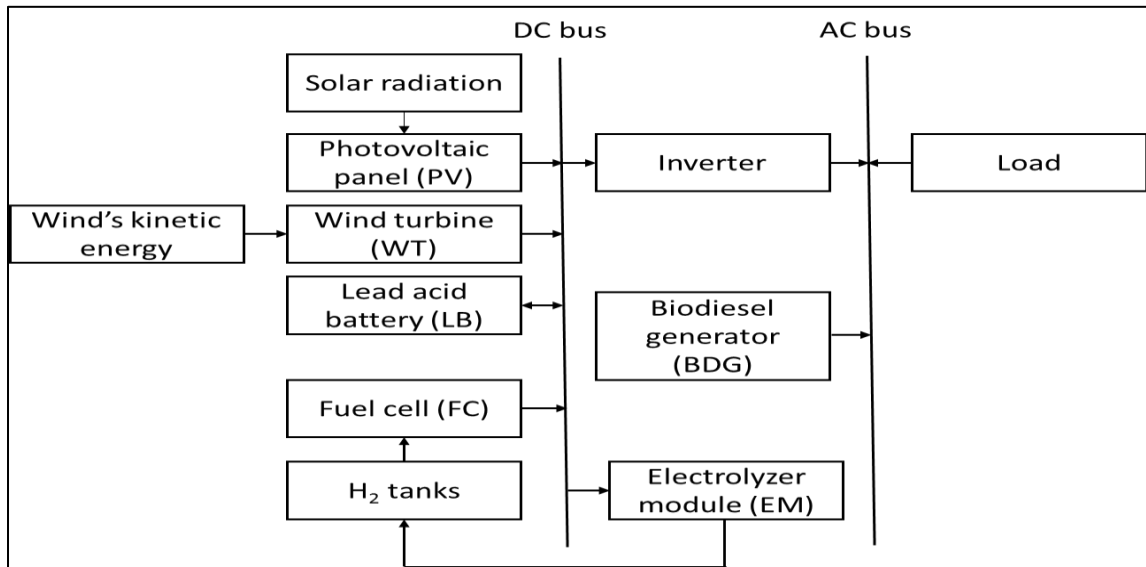
Figure 1 Schematic diagram of Microgrid

The aim of this work was to assess the techno-economic and environmental performance of the microgrid that provides power to a small residential community (fifty homes) in two US cities of Phoenix and Fargo. In the first step, hourly electricity consumption of the two cities was predicted using Artificial Neural Network (ANN) for the entire year. ANN was trained using the data for a single month of every season and was then subsequently used to predict the demand for rest of months of respective seasons. In the second step, based on demand and availability of renewable resources, microgrid was sized for lowest cost using optimization routine known as genetic algorithm (GA). The microgrid was assumed to be composed of PV, WT, lead acid battery (LB), biodiesel generator (BDG), FC, Electrolyzer module (EM) and hydrogen (H2) tanks (shown in Figure 1).

Techno-economic and environmental assessment models for each component of the microgrid were developed and deployed through an energy management strategy

(EMS) in GA. The technical, economic and environmental metrics evaluated were loss of load supply probability (LPSP), levelized cost of energy (LCOE, \$/kWh) and CO2 emissions (kg CO2 equivalent emitted/year).

The microgrid was sized for four levels of load (peak power) satisfaction, namely, 25%, 50%, 75% and 100%. The remaining load was assumed to be satisfied by conventional grid (CG).

Three different levels of carbon taxes (\$12, \$48, \$72 per tonne CO2) were also incorporated in economic costs to estimate microgrid's LCOE.

The paper is organized as follows: Section 2 sheds light on the renewable energy potential of the two considered US cities, Section 3 delves into the demand forecasting method and mathematical techno-economic and environmental models along with the formulation of optimization problem. Section 4 describes the electricity dispatch strategy and the GA optimization technique. Section 5 and 6 describe the results and conclusions respectively.

2. RENEWABLE ENERGY OF TWO US CITIES – FARGO AND PHOENIX

The solar and wind energy potential for Fargo, ND and Phoenix, AZ are shown in Figure 2.

The hourly direct normal irradiance (DNI), averaged for the entire year for Phoenix is 0.29 kWh/m^2 and is 65% more than of Fargo.

Conversely, the average hourly wind speed in Fargo is 7.3 m/s and is 40% more than of Phoenix. These values suggest that Phoenix has better solar potential than Fargo, while the latter has better wind potential than the former.
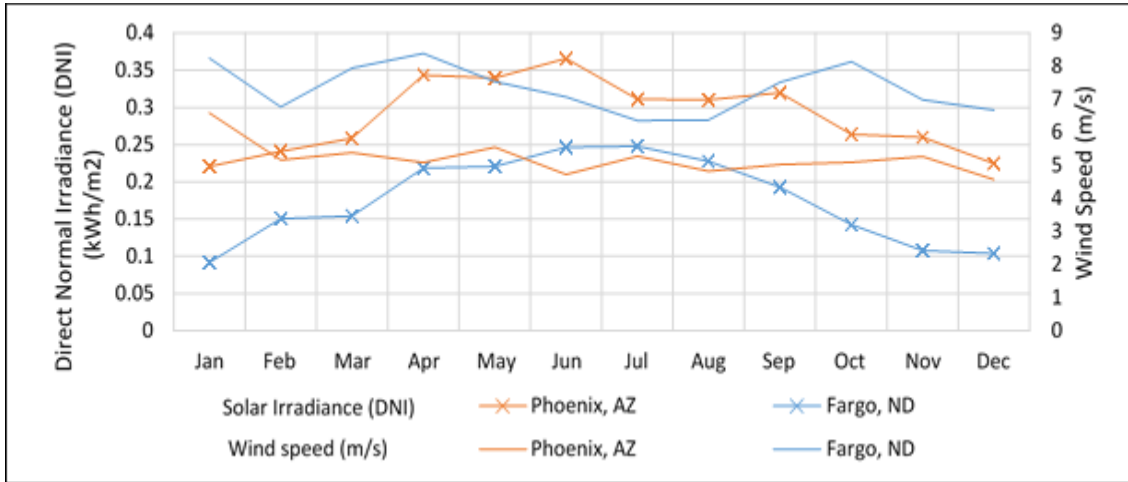
Figure 2 Solar and wind energy potential for Fargo, ND and Phoenix, AZ.

The location specific hourly irradiance and wind speed values have been taken from typical meteorological year (TMY3) data set [22].

3. MODEL DEVELOPMENT

This section develops the mathematical models for each component of the MG. The technical model is described first followed by economic and environmental emissions' model.

3.1. TECHNICAL MODEL

Mathematical models for individual MG components are described in this section.

3.1.1. Solar Model. The solar model is composed of two parts – solar irradiance and solar photovoltaic panel model.

Solar irradiance model calculates the location specific solar radiation that is incident on a tilted panel, Gβ (W/m2) and is given by [23]:

$$G_\beta(t) = G_{b,\beta}(t) + G_{r,\beta}(t) + G_{d,\beta}(t) \qquad (1)$$

$G_{b,\beta}$, $G_{r,\beta}$, $G_{d,\beta}$ are the direct, reflected and the sky diffuse components of solar irradiance respectively. Only two hourly values, namely, extraterrestrial radiation on a horizontal surface (ETR) and the global horizontal irradiance (GHI) were procured from TMY3 data set [22]. Based on these two location specific values, hourly values for each of the three radiation components were estimated using models described in the following section.

Initially, clearness index (k) was calculated by [24]:

$$k(t) = \frac{GHI(t)}{ETR(t)} \tag{2}$$

Subsequently, diffuse fraction (f) was calculated by [24]:

$$f(t) = 0.995 - 0.081k(t) \; for \; k(t) \le 0.21 \tag{3}$$

$$f(t) = 0.724 + 2.738k(t) - 8.321k^2(t) + 4.967k^3(t) for \; 0.21 < k(t) \le 0.76$$

(4)

$$f(t) = 0.18 \; for \; k(t) > 0.76 \tag{5}$$

Horizontal diffuse component (G_{dh}) was calculated by [24]:

$$G_{dh}(t) = f(t) \, GHI(t) \tag{6}$$

The value of $G_{b,\beta}$ was computed by [25]:

$$G_{b,\beta}(t) = (GHI \; (t) - G_{dh}(t)) \frac{\cos \theta(t)}{\cos \theta_z \; (t)} \tag{7}$$

In the above equation, θ_z and θ are zenith and incidence angles respectively.

The reflected component of solar irradiance $G_{r,\beta}$ (W/m^2) was calculated under isotropic solar irradiance [25]:

$$G_{r,\beta}(t) = \frac{\rho}{2} GHI(t)(1 - \cos \beta) \tag{8}$$

Here, β was the PV panel tilt (20^0) and ρ was the albedo (0.2).

Tilted component of solar radiation, $G_{d,\beta}$ (W/m^2) was computed using factor, f_k, which incorporates the effect of cloudy conditions. This f_k was given by [25]:

$$f_k(t) = 1 - \left(\frac{G_{dh}(t)}{GHI(t)}\right)^2 \tag{9}$$

$G_{d,\beta}$ was computed by [25]:

$$G_{d,\beta}(t) = G_{dh}(t)\left[0.5\left(1 + \cos\frac{\beta}{2}\right)\right]\left[1 + f_k(t)\left(\sin\frac{\beta}{2}\right)^3\right][1 +$$

$$f_k(t)(\cos\theta(t))^2(\sin\theta_z(t))^3] \tag{10}$$

G_β was calculated from the values of $G_{b,\beta}$, $G_{r,\beta}$ and $G_{d,\beta}$ using equation 1.

The model for PV panel computes the hourly power, $P_{gen,PV}$ (product of I_{mp} V_{mp}) produced by the PV panel. Two non-linear equations for current (I_{mp}) and voltage (V_{mp}) were solved in Matlab for each hour of the year using following expressions [26]:

$$\frac{I_{mp}(t)}{V_{mp}(t)} = \left[\frac{\frac{I_o(t)}{a(t)}exp\left(\frac{V_{mp}(t)+I_{mp}(t)R_S(t)}{a(t)}\right) + \frac{1}{R_{sh}(t)}}{1 + \frac{R_S(t)}{R_{sh}(t)} + \frac{I_o(t)R_S(t)}{a(t)}exp\left(\frac{V_{mp}(t)+I_{mp}(t)R_S(t)}{a(t)}\right)}\right] \tag{11}$$

$$I_{mp}(t) = I_L(t) - I_o(t)\left[exp\left(\frac{V_{mp}(t)+I_{mp}(t)R_S(t)}{a(t)}\right) - 1\right] - \left[\frac{V_{mp}(t)+I_{mp}(t)R_S(t)}{R_{sh}(t)}\right] \tag{12}$$

To solve the above equations hourly values of five parameters were needed - light current (I_L), diode reverse saturation current (I_o), modified ideality factor (a), series resistance (R_s) and shunt resistance (R_{sh}). These parameters are calculated from their own reference condition values. PV panel was assumed to be BP4175B (possessing capacity of 175W) and the parameter reference values for $I_{L,ref}$, $I_{o,ref}$, a_{ref}, $R_{s,ref}$, $R_{sh,ref}$ were assumed to be 5.467A, 1.452 x 10^{-9}A, 1.982V, 0.495Ω and 155Ω respectively [27]. The correlations to calculate the hourly values of five parameters are provided in subsequent sections.

The hourly value of PV module temperature, T_c (^{0}C), was estimated from ambient temperature and the solar radiation incident on panel (G_β) by [26]:

$$T_c(t) = T_{amb}(t) + (T_{NOCT} - 20)\frac{G_\beta(t)}{800}\left(1 - \frac{\eta_c}{0.9}\right)$$ (13)

Here, hourly value of T_{amb} was procured from TMY3 data [22] while T_{NOCT} (46.5 ^{0}C) denotes the nominal operating cell temperature [27] while η_c represents PV module efficiency (13.9%) [27].

Based on corresponding hourly values of G_β and T_c, the value of light current - I_L (A) was computed by [26]:

$$I_L(t) = \frac{G_\beta(t)}{G_{\beta,ref}}\left[I_{L,ref} + \mu_{I,sc}(T_c(t) - T_{c,ref})\right]$$ (14)

Here, $\mu_{I,sc}$ (0.005 A/^{0}C) denotes the short circuit temperature coefficient of PV module [27].

The hourly values for modified ideality factor, a (V), were estimated using the following correlation [26]:

$$\frac{a(t)}{a_{ref}} = \frac{T_c}{T_{c,ref}}$$ (15)

The shunt resistance (R_{sh}) was computed by [26]:

$$\frac{R_{sh}(t)}{R_{sh,ref}} = \frac{G_{\beta,ref}}{G_\beta(t)}$$ (16)

Based on the values of T_c, and E_g (material bandgap for Silicon), reverse diode saturation current, I_o (A), was calculated by [26]:

$$\frac{I_o(t)}{I_{o,ref}} = \left(\frac{T_c(t)}{T_{c,ref}}\right)^3 exp\left[\frac{1}{k}\left(\frac{E_{g,ref}}{T_{c,ref}} - \frac{E_g(t)}{T_c(t)}\right)\right]$$ (17)

Here, k indicates the Boltzmann constant (1.38 x 10^{-23} J/K). E_g (J) was estimated hourly by [26]:

$$\frac{E_g\,(t)}{E_{g,ref}} = 1 - 0.000267\big(T_c\,(t) - T_{c,ref}\big) \tag{18}$$

$E_{g,ref}$ was assumed to be as 1.794 x 10^{-19} J [26].

Using equations 13-18, hourly values for all the five parameters were calculated and inserted into equations 11 and 12 to estimate power $P_{gen,PV}$ (W) produced from PV module. However, $P_{gen,PV}$ represents the power produced by a BP4175B module of 175W power production capacity. The module was scaled up to 1kW capacity since the step size for optimization algorithm (GA) was 1kW.

3.1.2. Wind Turbine Model. Numerous models exist in the literature that compute the power generated by WTs as a function of wind velocity. Researchers either used a quadratic [28], cubic [29], statistical method [30] or turbine manufacturer provided power curves [27] to estimate power produced by a WT in a MG. In this work a cubic equation was employed to estimate WT power ($P_{gen,WT}$) using the following correlation [29]:

$$P_{gen,WT}\,(t) = \begin{cases} P_R\left(\frac{v^3(t)-v_c^3(t)}{v_R^3(t)-v_c^3(t)}\right) \; for \; v_c \leq v(t) \leq v_R \\ P_R \; for \; v_R < v(t) < v_F \\ 0 \; for \; v(t) < v_c \; and \; v(t) > v_F \end{cases} \tag{19}$$

Here, Bergey BWC XL turbine of 1kW capacity was chosen and velocity values for v_C, v_R and v_F were taken to be 3 m/s, 12 m/s and 23 m/s respectively [27]. Location specific hourly values of instantaneous velocity (v) at 100m were procured from NREL's database [31] and adjusted to 30m hub height using following equation [28]:

$$v(t) = v_{ref}(t)\left(\frac{H}{H_{ref}}\right)^{\alpha} \tag{20}$$

Here α is the wind speed power law coefficient whose value can be taken as (1/7) assuming well exposed WT location sites [28].

3.1.3. Lead Acid Battery Model. Lead acid batteries (LB) were chosen for electrochemical energy storage due to their low capital and maintenance costs as compared to Lithium ion batteries [32]. A normalized and generalized battery model was employed in this work as it was shown to represent a wide range of LBs [33,34]. Prior MG techno-economic works used a simple energy balance to compute energy stored in the battery and its state of charge and did not take model the transient effects of current, voltage, capacity and state of charge [10,17,21,28]. These gaps were addressed in this current LB model.

For sake of simulation, the nominal values of voltage (V_{nom}), current (I_{nom}) and capacity (C_{nom}, at 10 hours discharge rate) for a single electrochemical accumulator were assumed to be 2V, 55A and 550 Ah respectively [33,34]. A single LB unit was assumed to be constructed of 20 such accumulator connected in series resulting to a total energy capacity of 22 kWh. The flowcharts that depict the step by step calculations of the LB during its charging and discharging mode are provided in the SID. The following section describes each of the correlations that were used to model LB.

For charging regime, the value for Instantaneous state of charge (ISOC) at the end of time instant 't' was given by [33,34]:

$$ISOC(t) = \frac{ERIBI(t) + I_{batt}(t)V_{batt}(t)C_{eff}(t)}{C_{batt}(t)V_{batt}(t)} \tag{21}$$

During discharging regime, the value for ISOC was given by [33,34]:

$$ISOC(t) = \frac{ERIBI(t) - I_{batt}(t)V_{batt}(t)}{C_{batt}(t)V_{batt}(t)} \tag{22}$$

Here, $I_{batt}(t)$, $C_{batt}(t)$, $V_{batt}(t)$, $C_{eff}(t)$ are respective values for instantaneous current,

capacity, voltage and charging efficiency of the battery at the end of time instant 't'. ERIBI

(t) is the energy residing in the battery at the beginning of time instant 't'.

The transient nature of battery capacity - Instantaneous battery capacity (C_{batt})

was described by the following equation [33,34]:

$$C_{batt}(t) = \frac{1.67 \, C_{nom}[1+0.005 \, (T_{amb}(t)-25)]}{\left[1+0.67 \left(\frac{|I_{batt}(t)|}{I_{nom}}\right)^{0.9}\right]} \tag{23}$$

Here, T_{amb} (t) is the ambient temperature (^0C) which were procured from location

specific TMY3 data [22].

Neglecting internal resistances, a coulombic charging efficiency model was used

which given by [33,34]:

$$C_{eff}(t) = 1 - exp\left[\frac{20.73 \, (ISOC(t)-1)}{\frac{I_{batt}(t)}{I_{nom}}+0.55}\right] \tag{24}$$

The discharging efficiency was assumed to be 100%.

During charging regime, the battery voltage was given by [33,34]:

$$V_{batt}(t) = N_b \, [2 + 0.16 \, ISOC(t)] + N_b \, \frac{I_{batt}(t)}{C_{nom}}\left[\frac{6}{1+I_{batt}(t)^{0.86}} + \frac{0.48}{(1-ISOC(t))^{1.2}} + 0.036\right](1 - 0.025 \, (T_{amb}(t) - 25)) \tag{25}$$

During discharging regime, the battery voltage was given by [31,32]:

$$V_{batt}(t) = N_b \, [1.965 + 0.12 \, ISOC(t)] - N_b \, \frac{|I_{batt}(t)|}{C_{nom}}\left[\frac{4}{1+|I_{batt}(t)|^{1.3}} + \frac{0.27}{ISOC(t)^{1.5}} + 0.02\right](1 - 0.007 \, (T_{amb}(t) - 25)) \tag{26}$$

Here, N_b denotes the number of battery units.

3.1.4. Biodiesel Generator Model. Most of previously mentioned studies

employed a conventional diesel generator (DG) as a source of backup power in their MG

techno-economic analyses [10,17,36,37].

Few studies used a biodiesel generator (BDG) [11,38]. However in this work,

with an objective to increase the sustainability and reduce the carbon footprint, a BDG

was chosen. The specific fuel consumption C_{BD} (lit/hr) of the electric generator was given by [37]:

$$C_{BD} = 1.08 \left(0.08145 \, P_{NG} + 0.2476 \, P_{gen} \right) \tag{27}$$

Here P_{NG} (kWh) and P_{gen} (kWh) are nominal rated power and the actual power generated by the generator.

3.1.5. Fuel Cell Model. A hydrogen powered proton exchange membrane fuel cell (PEMFC) was chosen in this work as a means of backup power generator as its energy conversion efficiencies were found to be in the range of 40-60% which are higher than most of other energy conversion pathways [39]. A PEMFC consists of a cathode and an anode separated by a polymer electrolyte membrane. Pure H_2 is fed to anode where it is oxidized, while oxygen (mostly via air) is supplied to cathode where it is reduced subsequently producing water and heat.
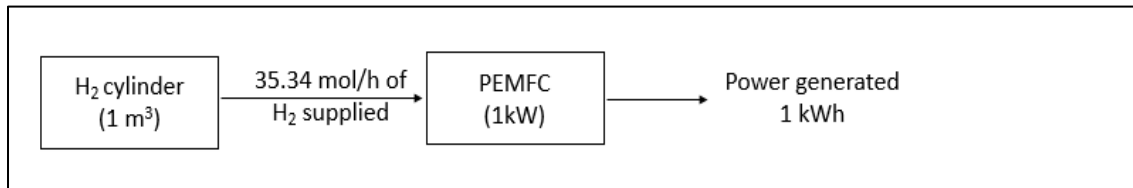
Figure 3 Schematic diagram of FC model

For simulation purposes, a one dimensional mathematical model that predicted the power generated by a FC was used [40]. The active area and electrical efficiency of FC were assumed to be 51.84 cm^2 and 42% respectively [40,41]. The entire FC model comprising of 47 equations was solved in a sequential manner to obtain curves for power – current density and efficiency- current density. Forty such PEMFCs (N_{FCs}) were then

assumed to be connected in series to scale up the capacity to 1kW. The systems level interaction and energy balance between H_2 cylinder and PEMFC is shown in Figure 3.

3.1.6. Electrolyzer Module. An electrolyzer (EM) is a FC operating in a reverse direction. It consumes electrical energy to produce H_2 and O_2. For simulation purposes, current (η_i) and voltage efficiencies (η_v) were assumed to be 100% and 74% respectively [42, 43]. The power rating of EM was assumed to be 1kW. H_2 released through EM was pumped to 13.5 MPa through a compressor and was stored in cylinder.
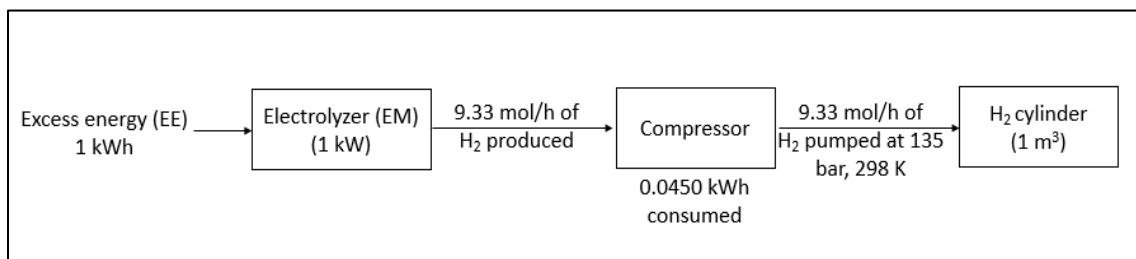
Figure 4 Schematic diagram of electrolyzer (EM), compressor and hydrogen cylinder

The systems level energy balance and the interaction between the EM, compressor and the H_2 cylinder is shown in Figure 4.

3.1.7. Electricity Consumption Model. As opposed to the prior MG studies utilizing a predefined load for energy consumption [11,17,20,21,28,42], this work utilized an artificial intelligence algorithm known as Artificial Neural Networks (ANN) to predict residential energy consumption.

For forecasting purposes, some researchers used software such as BEOpt [44] while others have used artificial intelligence methods such as random forest (RF) or ANN [45]. In this work, feed forward ANN trained with Levenberg - Marquardt back

propagation method was used because of its high accuracy in predicting location specific

energy consumption of buildings [45].

Table 1 Training and validation of model with actual energy consumption data for a
single home in Fargo, ND

Fargo, ND					
Seasons	**Training Period**		**Prediction and its validation with actual data**		
	Months	R^2	**Prediction and validation period**	R^2	**RMSE (kW)**
Spring	Jan 1 – 30	0.99	Dec 1 - 30, Feb 1 –30	0.96	0.09
Summer	Apr 1 – 30	0.98	Mar 1 - 30, May 1 – 30	0.92	0.10
Fall	Jul 1 – 30	0.97	Jun 1 - 30, Aug 1 – 30	0.96	0.07
Winter	Oct 1 – 30	0.99	Sep 1 - 30, Nov 1 – 30	0.92	0.12
Phoenix, AZ					
Spring	Jan 1 – 30	0.99	Dec 1 - 30, Feb 1 –30	0.98	0.05
Summer	Mar 1 - 30	0.99	Apr 1 – 30, May 1 - 30	0.96	0.13
Fall	Jul 1 – 30	0.97	Jun 1 - 30, Aug 1 – 30	0.96	0.07
Winter	Oct 1 – 30	0.99	Sep 1 - 30, Nov 1 – 30	0.95	0.19

Six predictor variables were used which were as follows: 1) Day of month 2)

Hour of day 3) Hourly dry bulb temperature (^{0}C) 4) Hourly relative humidity (%) 5)

Hourly Global Horizontal Irradiance (W/m^2) 6) Previous hour actual electricity

consumption taken from same day of same week from recorded data (kW) [45].

Table 2 Training and validation of model with actual energy consumption data for a single home in Phoenix, AZ

Seasons	Training Period		Prediction and its validation with actual data		
	Months	R^2	Prediction and Validation period	R^2	RMSE (kW)
Spring	Jan 1 – 30	0.99	Dec 1 - 30, Feb 1 –30	0.98	0.05
Summer	Mar 1 - 30	0.99	Apr 1 – 30, May 1 - 30	0.96	0.13
Fall	Jul 1 – 30	0.97	Jun 1 - 30, Aug 1 – 30	0.96	0.07
Winter	Oct 1 – 30	0.99	Sep 1 - 30, Nov 1 – 30	0.95	0.19

The response variable was hourly electricity consumption (kW). The location specific hourly values for predictor variables were obtained from NREL's website [22]. For each of the four seasons, ANN model was trained using the actual available data for representative month of that season. For model training purposes, the training period data was divided into 70% training, 15% testing and 15% validation.

The number of neurons in the hidden layer were set at 10 [45]. This trained model was used to make predictions for rest of the months in that particular season. The predicted data was validated with the actual available energy consumption data [46] for both the cities. This entire process was carried out for both the cities. The periods of training and testing for each season for Fargo and Phoenix are displayed in Table 1 and Table 2 respectively.
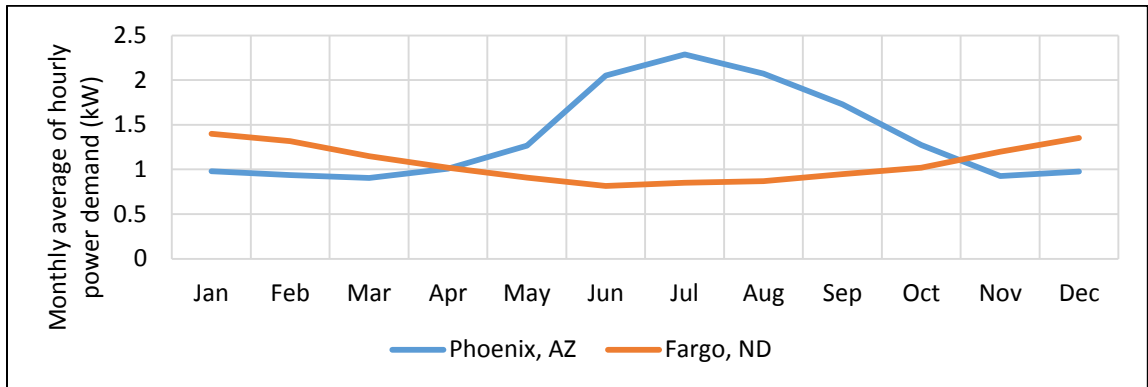
Figure 5 Monthly average of hourly electricity demand (kW) for a single home in both the cities.

The monthly average of predicted hourly electricity demand for both the cities are shown in Figure 5. The predicted energy consumption for a single home was linearly extrapolated to fifty homes assuming that each home uses same amount of electricity. This energy consumption profile was used for microgrid sizing purposes.

3.2. ECONOMIC AND ENVIRONMENTAL ASSESSMENT MODEL

The economic and environmental assessment methodologies are specified in this section.

3.2.1. Economic Assessment. The sole optimization objective was to minimize the LCOE ($/kWh) that was calculated by [10, 42]:

$$LCOE = \frac{TAC}{P_{L,an}} \tag{28}$$

Here, $P_{L,an}$ is the annual electricity demand (kWh) and TAC ($) is total annualized cost which was given by [28]:

$$TAC = (PVC)(CRF) \tag{29}$$

Here, PVC denoted the total present value of costs for acquisition, maintenance and replacement of microgrid components. CRF was the annual capital recovery factor which was given by [28]:

$$CRF = \frac{d\,(1+d)^T}{(1+d)^T - 1} \tag{30}$$

Here, d was the annual discount rate (8%) and T was microgrid lifetime (20 years).

Table 3 Capital, Installation and maintenance costs of microgrid components along with their respective lifespans

Module name	Capital costs, P_k ($/W)	Installation costs, $Inst_k$ (%)	Maintenance costs, Mtn_k (%)	Life span (yrs)
Solar PVs (PV) [49]	1.8	40	1	20
Wind turbines (WT) [49]	1.65	20	2	20
Lead acid battery (LB), $/Wh [49]	0.25	20	0	5
Biodiesel generator (BDG) [50]	1.01	10	2	20
Fuel cell (FC) [51]	5.8	10	2	5
Electrolyzer with compressor [20,37,42]	8.46	10	2	5
H₂ cylinder, $/cylinder [52]	300	10	0	20
Inverter (Inv) [49]	0.75	10	1	10

Some microgrid components such as LB, FC and EM will need replacement every 5 years. However, technologies for FC and EM are still in the nascent stage and it is assumed that their capital costs will fall with time due to technology maturation. The 10% (g_k=-0.1) annual drop was assumed to take place every year until the price of components reached 50% (Lg_k=-0.5) of their initial price. The time for reaching 50% reduction was estimated by [47]:

$$Y_{mat} = \frac{\log(1+Lg_k)}{\log(1+g_k)} \tag{31}$$

For all the components, the annual inflation rate was assumed to be 3%. For EM and FC the inflation rate came into effect only after Y_{mat} ended [47].

The present value (C_k) of capital (P_k) and installation costs (P_k $Inst_k$) for component 'k', for PV, WT, BDG and H_2 cylinder was given by [47]:

$$C_k = P_k(1 + Inst_k) \tag{32}$$

For LB the equation assumed was [47]:

$$C_{LB} = P_{LB}(1 + Inst_{LB})\left[1 + \left(\frac{1+i}{1+d}\right)^5 + \left(\frac{1+i}{1+d}\right)^{10} + \left(\frac{1+i}{1+d}\right)^{15}\right] \tag{33}$$

For inverter following equation was used [47]:

$$C_{Inv} = P_{Inv}(1 + Inst_{Inv})\left[1 + \left(\frac{1+i}{1+d}\right)^{10}\right] \tag{34}$$

For EM and FC components following equations were used [47]:

$$C_k = P_k(1 + Inst_k)\left[1 + \left(\frac{1+g_k}{1+d}\right)^5 + \frac{(1+g_k)^7(1+i)^3}{(1+d)^{10}} + \frac{(1+g_k)^7(1+i)^8}{(1+d)^{15}}\right] \tag{35}$$

The component wise capital, installation and maintenance costs are provided in Table 3. The biodiesel consumption costs were assumed to be $0.91/lit [48].

Utilizing the cost factors provided in Table 3, the present value of maintenance costs for component 'k' was computed by [28,47]:

$$CMtn_k = \sum_{T=1}^{T=20} P_k \, Mtn_k \left(\frac{1+i}{1+d}\right)^T \tag{36}$$

The total annualized costs in present value for all the components (k) was given by [28,47]:

$$TAC = CRF \sum_{k=1}^{k=7} (C_k + CMtn_k) \, N_k \tag{37}$$

Here, N_k is the number of 'k' type components.

3.2.2. Environmental Assessment. The GHG emissions are estimated first in this section which are then followed by their social cost.

Table 4 Greenhouse gases emission factors for microgrid components and conventional electric grid [38]

Component	LCA GHG emissions (kg CO_2 eq./kWh), e_k
PV module (mono- Si)	0.045
WT (at speed 6.5 m/s)	0.011
Lead acid battery (per kWh stored)	0.028
Biodiesel generator	0.191
Fuel cell	0.664
Electrolyzer and H_2 tanks	0.011
US conventional electric grid [53]	0.51

The GHG emissions (kg CO_2 equivalent) were estimated on the basis of life cycle assessment (LCA) of power generation. The individual emission factors for microgrid components and conventional fossil fuel grid are shown in Table 4. The net GHG emissions (TE, kg CO_2 eq./yr) for microgrid were estimated using the following equation:

$$TE = \sum_{k=1}^{k=7}(p_k e_k) \tag{38}$$

3.2.3. Country-level Social Cost of Carbon (CSCC) or Carbon Tax. Social cost of carbon (SCC) is a measure of economic damage (or benefit) caused due to CO_2 emissions.

For every tonne of CO_2 emitted, some studies estimate the SCC to be within \$10 - \$1000 [54-56] while others report a value within \$150 - \$200 [57]. The US' Environmental Protection Agency recommends SCC values of \$12, \$42 and \$72 based on social discount rates of 5%, 3% and 2.5% respectively. In place of global SCC, a recent study by Ricke et al. estimated country-level SCC (CSCC) that focused on economic damage caused to a particular country or region for every emitted tonne of CO_2 [58]. For instance, the authors estimated the highest value of CSCC to India at \$86, followed by US and Saudi Arabia at \$48 and \$47 respectively. One of the merits of the current work was to utilize such CSCC values instead of global SCC values. Because the current work focuses on microgrids in the US, three CSCC values were imposed that were not only in accordance with US EPA but also with CSCC values suggested by Ricke et al [58]. The CSCC values imposed on each of the four microgrid penetration levels were \$12, \$48 and \$72/tonne CO_2 and their effect on electricity cost (\$/kWh) was examined. The additional costs due to this were added to the TAC in equation 28.

3.2.4. Constraints. There were five main constraints which were as follows:

1. The values for number of components (N_k) were assumed to take only integer

   values. The bounds for every component were given by:

$0 \leq N_k \leq N_{k,max}$

The upper bound of variables - (N_{PV} N_{WT} N_{LB} N_{BDG} N_{FC} N_{EM} N_{H2}) was set at (300

300 50 300 300 300 50) while the lower bound was set at zero. Here, N_k not only

denotes the number of units of particular component, k, but also indicates its

installed capacity. For instance, N_{PV} indicates 2 PV components having a total

capacity of 2 kW. This also holds true for WT, EM, FC and BDG components. In

case of LB, N_{LB} of value 2 denotes 2 LB units, each possessing a storage capacity

of 22kWh. This capacity for LB was chosen in such a way that the battery alone

should be able to power a single home for at least 10-12 hours. Similarly the value

of a single H_2 cylinder capacity was selected to be $1m^3$ which can power a single

home for 2-3 days through FCs.

2. The LB model was only operational when the ISOC lied between 20% and

   80% and this is represented by the equation:

   $0.2 \leq ISOC(t) \leq 0.8$

3. From the peak power standpoint, optimum microgrid configurations were

   determined for four MG penetration levels, namely, 25%, 50%, 75% and

   100%. A level of 25% indicated that only the top 25% of annual power

   demand of the residential community was fulfilled by the microgrid while the

   rest (75%) was met through conventional grid. Thus the residential

community was dependent on microgrid for fulfilling peak power demand
while its baseload demand was met by CG.

4. The loss of power supply probability (LPSP) for microgrid was computed
using the following expression [10] and it was maintained at zero for every
penetration level:

$$LPSP\ (t) = \sum_{t=1}^{8760} \left(\frac{P_L(t) - P_{gen}(t)}{P_L(t)} \right)$$

5. The H2 cylinder model was assumed to be operational only when the pressure
in it lied between 135 bar and 27 bar [59].

$$27\ bar \leq Pressure\ (t) \leq\ 135\ bar$$

4. METHODOLOGY

This section entails the description of electricity dispatch strategy (EDS) of the
microgrid and the GA technique.

4.1. ELECTRICITY DISPATCH STRATEGY (EDS)

The flowchart for the hourly EDS is shown in Figure 6. Initially, the energy
generation by primary sources such as PV and WT were determined based on their
individual generating capacity and meteorological data (wind speed and solar radiation).
Based on the difference between generated power and demand, the EDS splits into two
routes. One for excess energy (EE) while the other for energy deficit (ED). In case of EE,
the LB model is run into charging mode while in case of ED it is run in discharging
mode. After LB model, if ED still exists, then BDG unit is run to fulfil the shortfall. If
BDG is unable to fulfil it, then FC model is operated which is the last energy dispensing

unit. After this step the LPSP is calculated. In case of EE path (after LB model), H_2 is generated through electrolyzer which is stored in the cylinder. After this step if EE still exists, then LPSP is assigned a value of zero and the EE is sold to the conventional grid at 50% of retail electricity costs. The retail electricity costs (per kWh) in Phoenix and Fargo were assumed to be $0.103 and $0.089 respectively [60].
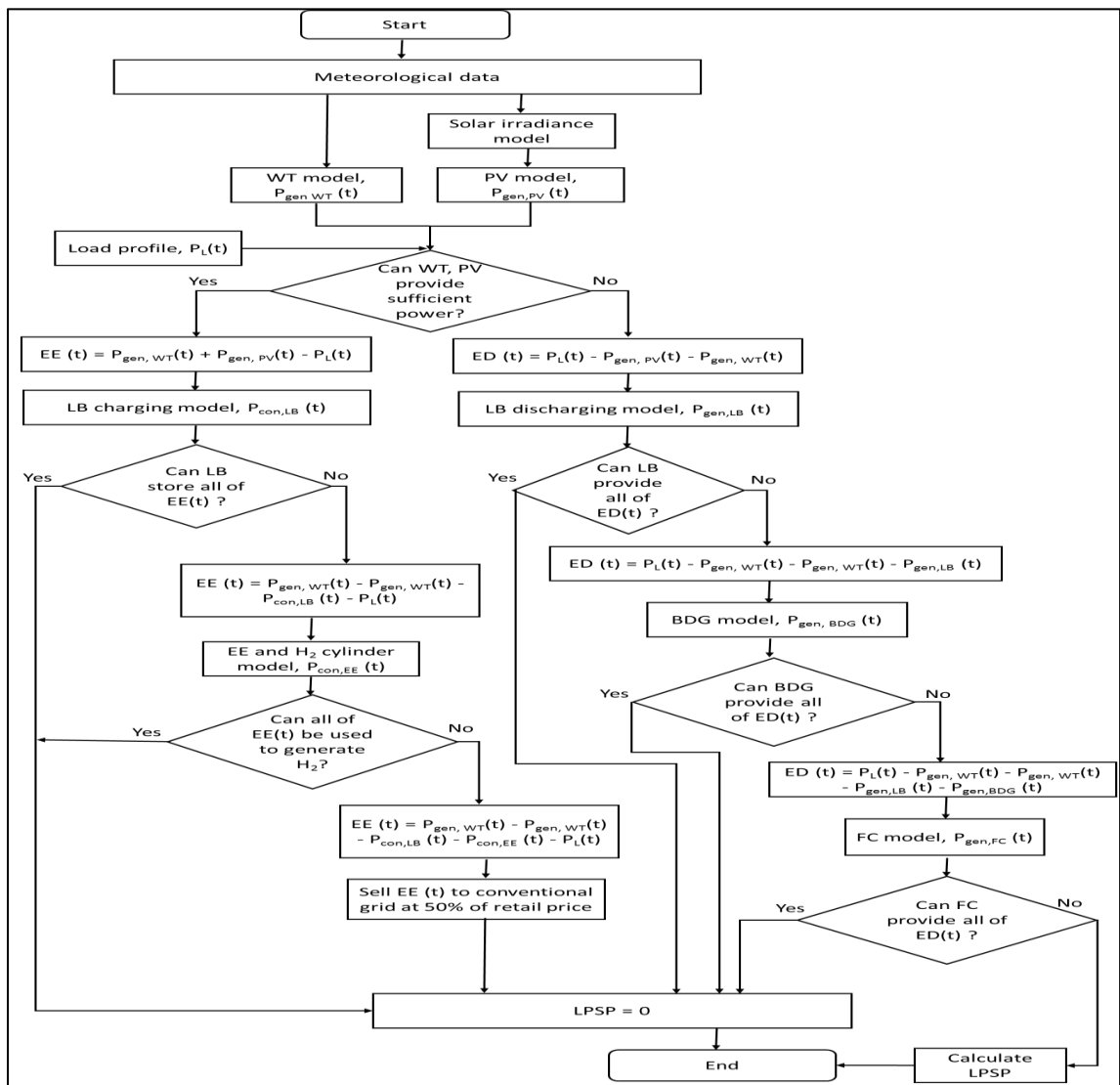
Figure 6 Electricity dispatch strategy (EDS) of the microgrid

4.2. GENETIC ALGORITHM (GA)

GA was employed to find the optimum microgrid configurations (least LCOE) for each of the four MG-CG integration scenarios (MG penetration level - 25%, 50%, 75%, 100%).
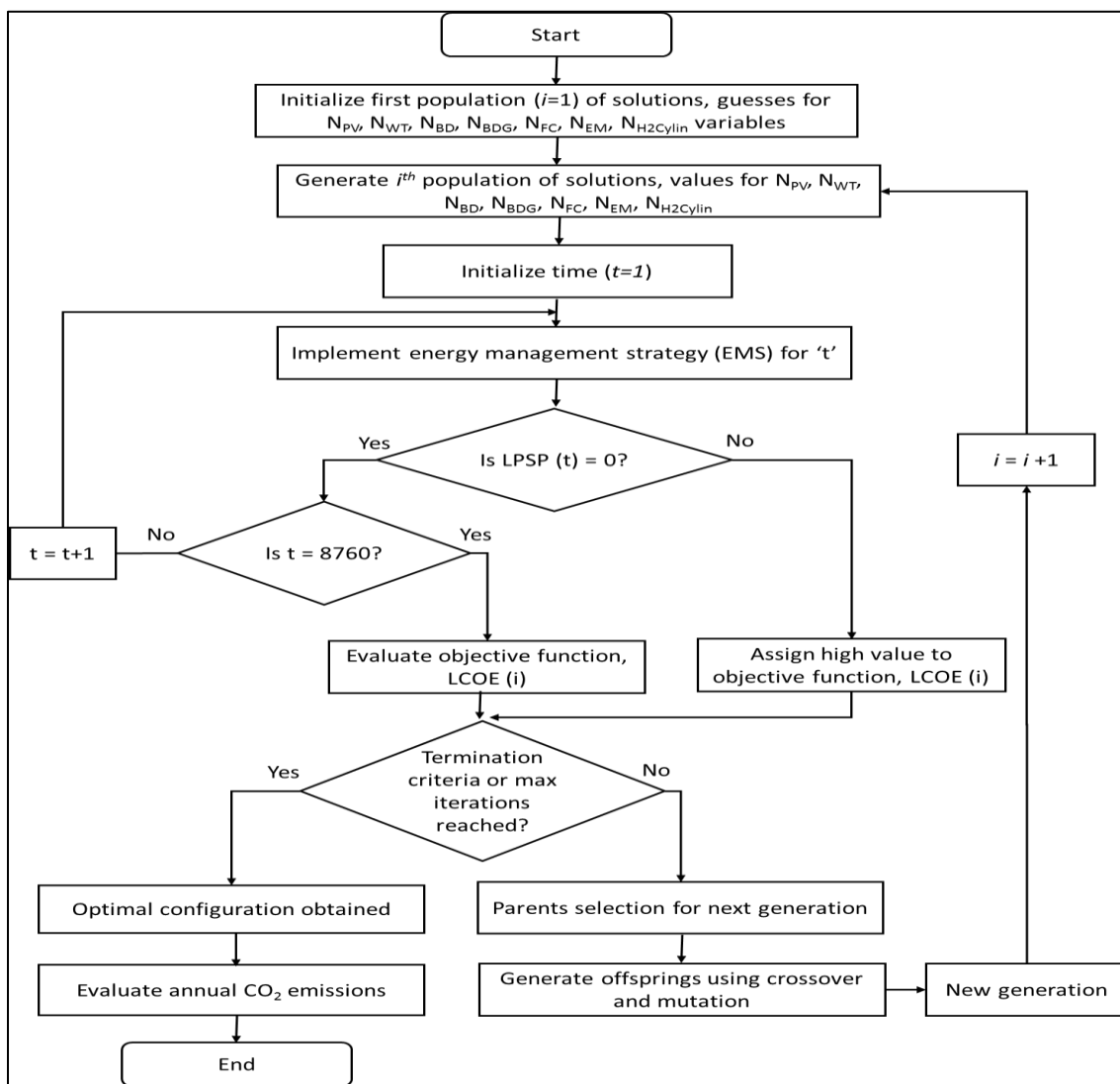
Figure 7 GA Flowchart

Using Matlab, these simulations were carried out on a computer having a dual core processor (i5-3230M) with 4GB of memory. The flowchart for GA is depicted in Figure 7.

In the first step of the GA, a random population of solutions was generated. Each solution (N_{PV} N_{WT} N_{LB} N_{BDG} N_{FC} N_{EM} N_{H2}) represented a single microgrid configuration. For every solution in the current population EDS was implemented for every time instant of the entire year and its annual LPSP value was evaluated. The value of LPSP (objective function) was a measure of fitness of a solution. Lower the value of LPSP, higher is the solution's fitness. Fittest individuals of the population were then chosen as parents which generate offsprings (new solutions) through crossover and mutation. Through such mechanism, a new generation (of new solutions) was generated which was fitter than previous generation. Again the EDS was implemented for all the new solutions to finally compute the value of LPSP. This iterative procedure was terminated if the number of generations exceeded the maximum allowed (threshold) value. The optimum solution was the fittest individual of the current population. The operator values utilized for genetic operators are depicted in Table 5.

Table 5 Genetic algorithm operator values [61]

Parameter	Population size	Maximum generations	Crossover probability	Mutation probability	Elitism probability
Value	200	700	0.8	0.01	0.05

5. RESULTS

In this section the results have been presented for each of the MG penetration levels (25%, 50%, 75% and 100%). For these levels and both the cities, the GA evaluated only about 2.18 x 10^{-9} % of the total number of possible solutions in the entire solution domain before converging to the optimum solution (MG configuration with least LCOE). The average run time of the GA was approximately 10 minutes.

5.1. 25% PEAK POWER PENETRATION MG LEVEL WITH SCC OF $48/TONNE CO$_2$

The lowest cost MG configurations and electricity cost for 25% peak penetration level with $48 per ton of CO$_2$ are depicted in Table 6. With respect to MG's net installed capacity, high preference was shown to WTs than PVs in Fargo due to the Fargo's high wind energy potential (Figure 2). Similarly in case of Phoenix, high preference was shown to PVs than WTs due to the city's high solar energy potential. For both the cities, preference was not given to FC and EM units by the optimization routine (GA) due to their high costs. The LCOEs obtained for Fargo and Phoenix were $0.73 and $0.86 per kWh respectively while the corresponding GHG emissions of those cities were 12 and 10 times as that of CG. Varying the SCC from $12 to $72 did not show any effect on the MGs' LCOE nor its configuration.

The monthly average of hourly power provided by MG components and conventional grid in Fargo is depicted in Figure 8. Since MG was only operational during the peak 25% of power demand, its energy generation trends followed those of demand. For instance in case of Fargo, about 56% of the total annual energy produced by MG was

generated during the four months of November to February because these months

accounted for nearly 40% of the total annual power consumption.

For Phoenix, approximately 78% of the total annual energy produced by MG was

generated during the four months of June to September as these months accounted for

nearly half of the total annual energy demand.

Table 6 Lowest cost microgrid configurations and electricity cost for 25% peak penetration level with $48 per tonne of CO2

Microgrid (MG)									Conventional grid (CG)	
N_{PV} (kW)	N_{WT} (kW)	N_{LB} (22 kWh)	N_{BDG} (kW)	N_{FC} (kW)	N_{EM} (kW)	N_{H2} (kW)	LCOE ($/kWh)	GHG (tonne CO_2 eq./yr)	COE ($/kWh)	GHG (tonne CO_2 eq./yr)
Fargo, ND										
9	57	3	106	0	0	0	0.73	15	0.11	178
Phoenix, AZ										
49	7	8	190	0	0	0	0.86	23	0.13	230

The power produced by MG's individual components was shown to depend on not only the installed capacity but also on the power dispatch strategy (EMS). For instance in Fargo, even though the generation capacity of WT is nearly half as that of BDG, the energy produced by WTs is nearly 1.6 times as that of BDGs. This is because WTs are a primary sources of energies while BDGs are secondary sources. Similarly for Phoenix, the installed power generation capacity ratio of BDGs to PVs is 3.87 while their corresponding annual power generation ratio is 1.07.

The average monthly LCOEs ($/kWh) of MG components and CG for Fargo are shown in Figure 9. The LCOE was also observed to show an inverse relationship with the amount of monthly energy generated by MG. For instance owing to their high share of annual energy generation, the average LCOE for the four months from November to February was shown to be 63% less than the average LCOE value observed for rest of the months. Similar observation was also made in case of Phoenix during the months of June to September.
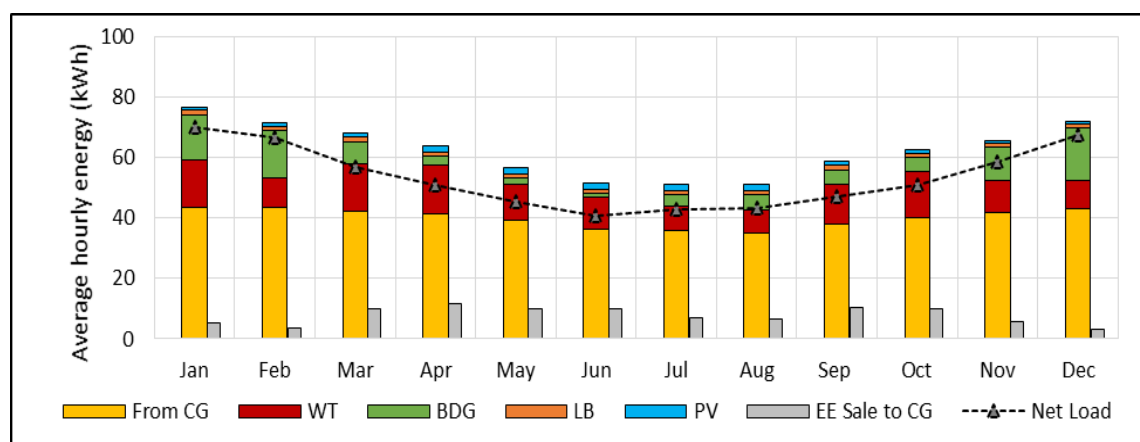
Figure 8 Monthly average of energy provided by MG components and CG for Fargo
(25% MG penetration level and $48/tonne CO2)

It was observed for MG located in Fargo that the share of BDG in annual LCOE was 58% while the shares of inverter and WT were 18% and 16% respectively. BDG was expected to occupy a major share because it generates low amounts of energy (35% annual energy share within MG) while simultaneously possessing high capital costs (due to its elevated installed capacity, see Table 3). Similarly for Phoenix, the shares of BDG, inverter, LB and PV in net annual LCOE were found to be 37%, 25%, 18% and 14% respectively.

The differential increase in electricity cost ($/kWh) for CG due to incorporation of $48/tonne CO_2 of SCC was observed to be nearly 4 times as that of MG. This is because the carbon footprint (GHG emissions per kWh of power produced) of CG is nearly 6.4 times as that of MG. For both the cities, the sale of excess electricity barely affected the MG's LCOE due to their presence in small amounts.

Figure 9 Average monthly LCOE of MG components and CG for Fargo (25% MG penetration level and SCC of $48 per tonne CO2)

Figure 10 Average monthly LCA GHG emissions (tonne CO2/yr) for Fargo (25% MG penetration level and SCC of $52 per tonne CO2)

The GHG emissions due to MG and CG for Fargo are depicted in Figure 10. The share of CG in total annual emissions attributed to electricity production was about 92%. This was due to two factors, namely, CG's high CO_2 emission factor (Table 4) and its high share of annual energy production (75%). Within MG, almost 85% of the total annual emissions were attributed to BGD even though its share in annual energy generation was just 36%. This is because the emission factors of BGD are roughly 4 times as that of PV or WT (Table 4).

5.2. 50% PEAK POWER PENETRATION LEVEL OF MG

The lowest cost configurations and LCOE for 50% peak penetration level with SCC of $48 per tonne of CO_2 are displayed in Table 7. With regards to 25% level in Fargo, the individual generation capacities of PV, WT, LB, BDG increased by about 5.1, 1.68, 1.33 and 1.15 times respectively. The corresponding increases observed for Phoenix were 2.97, 1.57, 2.75 and 1.21 respectively.

Table 7 Lowest cost MG configurations in Fargo and Phoenix (50% penetration level and SCC of $48 per tonne CO2)

Microgrid (MG)									Conventional grid (CG)	
N_{PV} (kW)	N_{WT} (kW)	N_{LB} (22 kWh)	N_{BDG} (kW)	N_{FC} (kW)	N_{EM} (kW)	N_{H2} (kW)	LCOE ($/kWh)	GHG (tonne CO_2 eq./yr)	COE ($/kWh)	GHG (tonne CO_2 eq./yr)
Fargo, ND										
46	96	4	122	0	0	0	0.54	24	0.116	119
Phoenix, AZ										
146	11	22	231	0	0	0	0.70	35	0.13	153

On average, the MG's net power generation capacity increased by roughly 55% for both the cities. This growth in capacity mainly occurred in accordance with the respective city's renewable energy potential. For instance, due to the high solar energy potential (Figure 2) in Phoenix, its share of PV and BDG in net capacity increase were observed to be 68% and 28% respectively. Similarly, the shares of PV, WT and BDG in capacity increases were observed to be 40%, 42% and 17% respectively. For both the cities, increasing the MG's penetration level by 25% decreased the MG's LCOE by 26% and 19% respectively demonstrating the economies of scale effect. For Fargo and

Phoenix, the total annual carbon footprint of the residential communities diminished by 26% and 34% respectively owing to 25% decrease in energy production.

For Fargo, the energy distribution within MG components and that of CG with SCC of $48/tonne CO_2 is shown in Figure 11. With respect to 25% peak power penetration level, the energy produced by WT and BDG increased by 68% and 50% respectively while that of PV surged by a factor of 5. Due to increased amounts of energy produced by PV and WT, the amount of excess energy sold to CG also rose by 65%. For Phoenix, PV units accounted for nearly 92% of the total increase in annual power produced by MG.
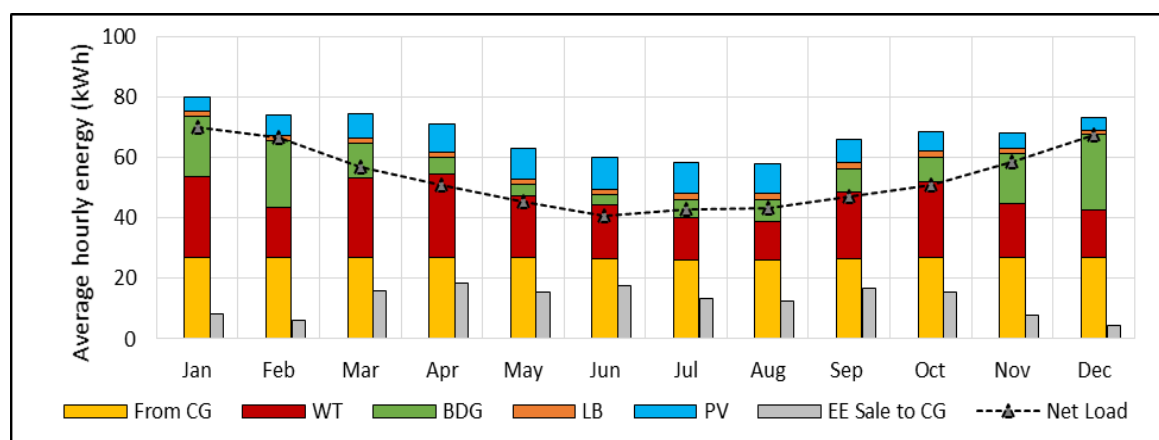
Figure 11 Monthly average of energy provided by MG components and CG for Fargo (50% MG penetration level and SCC of $48 per tonne CO2)

The average monthly LCOEs ($/kWh) of MG components and CG for 50% peak penetration level in Fargo are shown in Figure 12. With respect to 25% penetration level, even though there was a 53% increase in MG's capital expenses (due to increased generation capacity), its annual LCOE decreased by 26% due to 28%, 35% and 50%

decline in LCOEs for WT, BDG and inverter respectively. The effect of capital cost on

LCOE was offset by the 25% increase in the amount of energy produced by individual

components of MG. Similarly for the case of Phoenix, the annual LCOE fell by 19% due

to decline in component wise LCOEs for LB, BDG and inverter by 42%, 63% and 78%

respectively.

For both the cities, imposing a SCC of \$48/tonne CO_2 barely affected the net

LCOE of MG. However, it increased the CG's retail electricity cost by approximately

28% or \$0.026 /kWh.
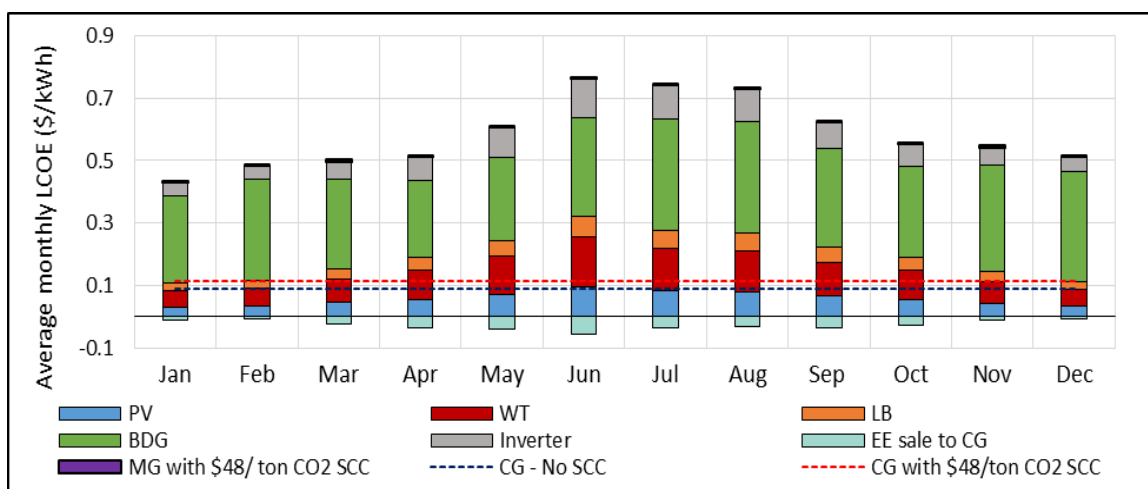
Figure 12 Average monthly LCOE of MG components and CG for Fargo (50% MG
penetration level and SCC of \$48 per tonne CO2)

For Fargo, the average monthly LCA GHG emissions of MG components and CG

for 50% MG penetration level are shown in Figure 13. Even though CG and MG

produced equal amounts of annual power, MGs share of total annual emissions was about

one fifth. However, this still represents a 60% increase in CO_2 emissions for MG with

respect to 25% peak penetration level which was caused primarily due to 50% increase in

BDG's carbon footprint. In case of Phoenix, MG's carbon footprint was also about one fifth which denoted a 52% increase of its own carbon footprint relative to 25% peak penetration level. This upsurge was mainly caused due to tripling of carbon footprint caused due to PV's power generation.
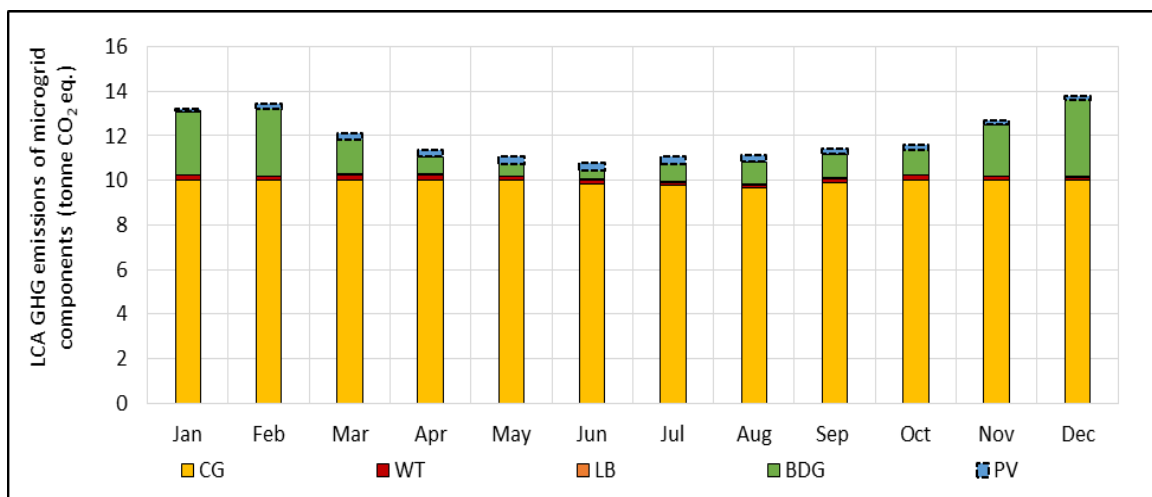
Figure 13 Average monthly LCA GHG emissions (tonne CO2/yr) for Fargo (50% MG penetration level and SCC of $48 per tonne CO2)

5.3. 75% PEAK POWER PENETRATION LEVEL

The lowest cost configurations and LCOEs for 75% peak penetration level with SCC of $48 per tonne of CO_2 are displayed in Table 8.

For Fargo and Phoenix, further increase in peak power penetration level by 25% increased the net MG generation capacities by roughly 28%. Owing to the high wind energy potential in Fargo, 55% of this increase was caused due to increase in generation capacities of WTs while the rest of the increase was attributed to BDGs and PVs in equal amounts. Similarly for Phoenix, the share of increase in MG's generation capacity was dominated by PV (69%) followed by BDG (21%) and WT (9%).

Table 8 Lowest cost MG configurations in Fargo and Phoenix (75% penetration level and SCC of $48 per tonne CO2)

Microgrid (MG)									Conventional grid (CG)	
N_{PV} (kW)	N_{WT} (kW)	N_{LB} (22 kWh)	N_{BDG} (kW)	N_{FC} (kW)	N_{EM} (kW)	N_{H2} (kW)	LCOE ($/kWh)	GHG (tonne CO_2 eq./yr)	COE ($/kWh)	GHG (tonne CO_2 eq./yr)
Fargo, ND										
64	140	3	139	0	0	0	0.47	34	0.116	60
Phoenix, AZ										
221	21	35	254	0	0	0	0.60	45	0.13	77

For Fargo and Phoenix, with respect to 50% penetration level, the annual values of MG's LCOE were observed to decline by nearly 13% thereby depicting the economies of scale effect. The total annual CO_2 emissions attributed to power production in those cities were also observed to decline by nearly one third. This was due to 50% decline in GHG emissions owing to CG's electricity production.

For Fargo, the energy distribution within MG components and that of CG with SCC of $48 is shown in Figure 14. Within the MG, approximately half of the annual energy was produced by WT (due to high wind potential) while 28% was produced was by BDG and the rest by PV units. For the MG located in Phoenix, nearly three fourths of

the total energy was generated via PVs (due to high solar potential) while BDGs and WTs generated about 21% and 4% respectively.

With respect to 50% MG penetration level in Fargo, the average annual energy generated by WT and BDG increased by roughly 45% while that of PV increased by 39%. Furthermore, it was also observed that the average amount of energy stored in LB remained the same while that sold to CG rose by 30%. In case of Phoenix, the average annual energy generated by PV units rose by nearly 50% while that of other components remained approximately the same. However, as opposed to Fargo, the hourly average of energy stored in LB rose by 73% while the amount of excess energy sold to CG remained nearly the same.
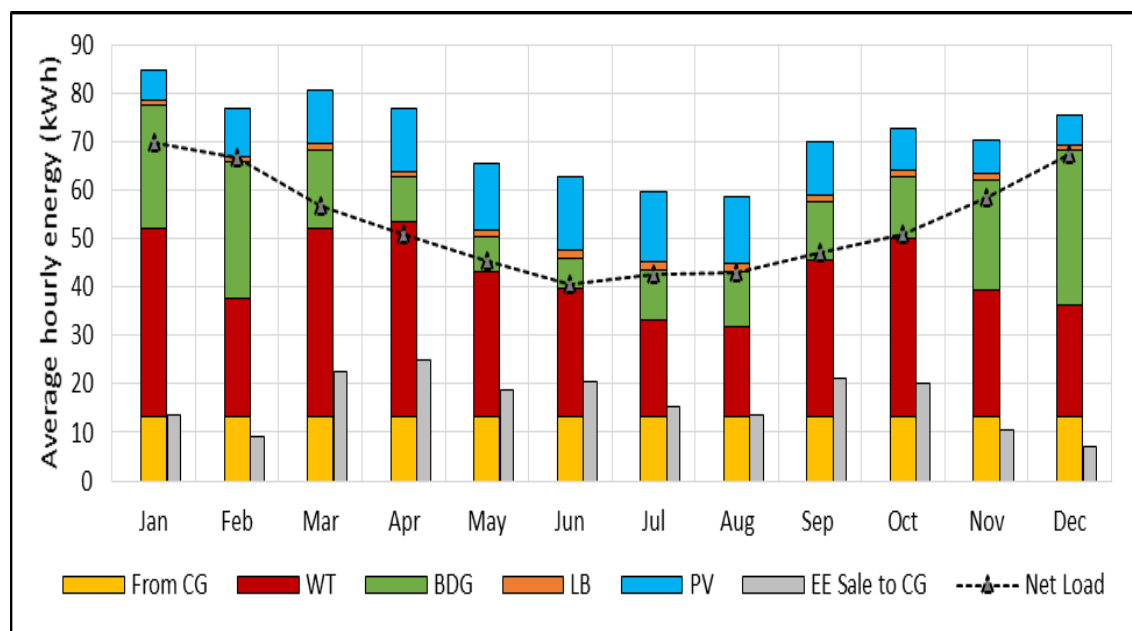
Figure 14 Monthly average of energy provided by MG components and CG for Fargo (75% MG penetration level and SCC of $48 per tonne CO2).

The average monthly LCOE ($/kWh) of MG components and CG for 75% peak penetration level in Fargo are shown in Figure 15. The shares of BDG and WT in annual LCOE were 58% and 19% respectively while those of PV and inverter were about 10% each. For Phoenix, each of BDG and LB had a share of 30% while PV and inverter had shares of 22% and 12% respectively. For both the cities, the sale of excess energy sold to the grid reduced the annual LCOE by approximately 3%. The imposition of carbon tax ($48 SCC) barely affected the LCOE for both the cities.

With respect to 50% MG penetration level in Fargo and Phoenix, the shares of individual components in annual LCOE remained roughly the same.
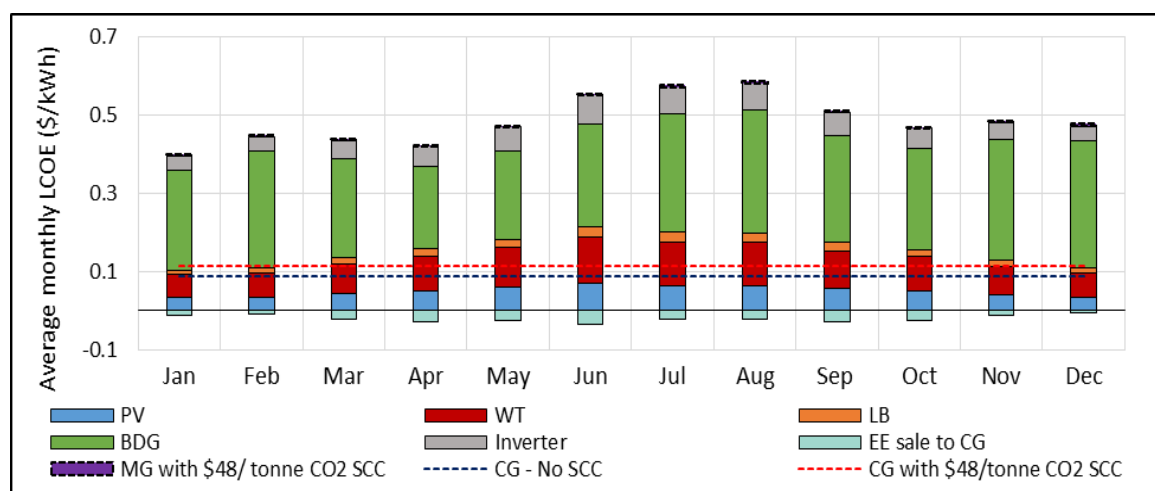
Figure 15 Average monthly LCOE of MG components and CG for Fargo (75% MG penetration level and SCC of $48 per tonne CO2)

For Fargo, the average monthly LCA GHG emissions of MG components and CG for 75% MG penetration level are shown in Figure 16. For both the cities, even though MG generated about three fourths of the total annual energy, its share in total annual

carbon footprint was just one third. This can be attributed due to low emission factors of MG components (Table 4) as compared to CG.

Within MG situated in Fargo, even though BDG generated only about a quarter of MG's annual energy, its share in MG's total annual CO_2 emissions was nearly three fourths. Furthermore, even though PV only generated about one third of the annual energy as WT, its carbon footprint was nearly 1.5 times as that of WT. This was observed due to the emission factors of individual MG components and of CG (Table 4). For instance, on a life cycle basis, PV emits four times as much GHG emissions as WT to produce same amounts of power. For MG situated in Phoenix, the shares of BDG and PV in annual CO_2 emissions were 50% and 40% respectively while the rest was due to LB. The WTs had a negligible carbon footprint for MG in Phoenix.
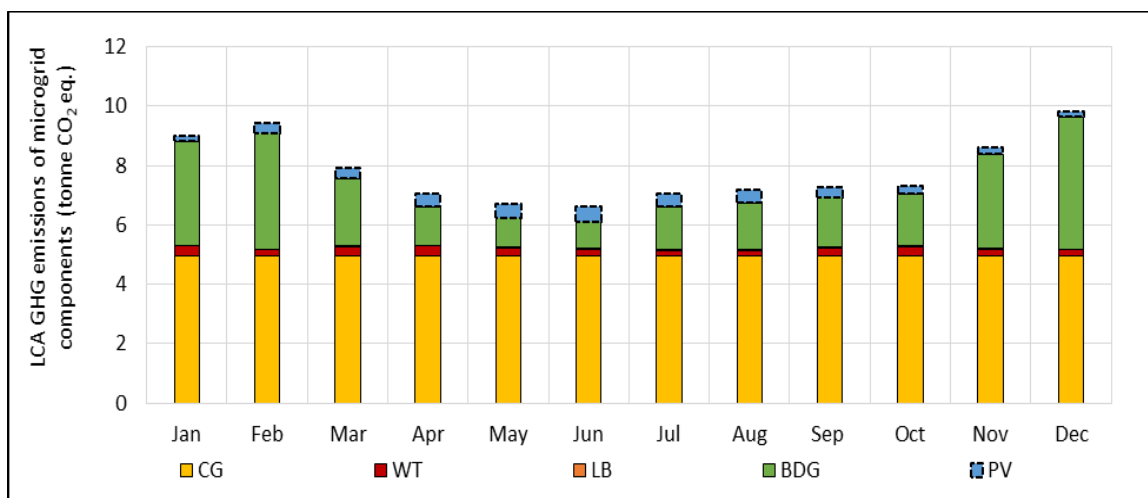
Figure 16 Average monthly LCA GHG emissions (tonne CO2/yr) for Fargo (75% MG penetration level and SCC of $48 per tonne CO2)

5.4. 100% PEAK POWER PENETRATION LEVEL (STANDALONE MICROGRID)

The MG configurations at 100% penetration level are essentially standalone power generation units which are able to meet the complete power demand of the residential community. The lowest cost configurations and LCOEs with SCC of $48 per tonne of CO_2 are displayed in Table 9.

For Fargo, it was observed that the rate at which new component specific capacity additions which were made to MG was similar to that of 75% penetration level. For instance, 18 kW of new generation capacity was made to PV for 100% penetration level which were roughly similar to that made for 75% penetration level which was 19 kW. Similar observation was also made for the case of MG situated in Phoenix.

With respect to 75% penetration level in Fargo and Phoenix, the annual LCOEs declined by nearly 8%. The corresponding annual GHG emissions of the residential communities also fell by roughly half.

The annual GHG emissions of MG were found to nearly one fifth as that of an equivalent 100% CG.

For Fargo, the energy distribution within MG components and that of CG with SCC of $48/tonne CO_2 is shown in Figure 17. As expected, major share of annual energy was produced through WTs (53%) than PVs (28%) or BDGs (19%). It is interesting to note that MG finds it cheaper to produce energy through BDGs than utilizing stored energy in LBs (which was originally generated via WTs). This indicates the life cycle costs ($/kWh) of BDG (which includes biodiesel fuel costs) is less than that of LBs (generation plus storage). As a consequence of this, the average annual energy supplied by LB is 44 times less than that of BDG for the case of Fargo. However, in case of

Phoenix, a converse phenomenon was observed. It was cheaper for MG to utilize LBs

than BDGs as a result of which the average annual energy dispatched by LBs was found

out to be 1.5 times as that of BDGs.

Table 9 Lowest cost MG configurations in Fargo and Phoenix (100% penetration level and SCC of $48 per tonne CO2)

Microgrid (MG)									Conventional grid (CG)	
N_{PV} (kW)	N_{WT} (kW)	N_{LB} (22 kWh)	N_{BDG} (kW)	N_{FC} (kW)	N_{EM} (kW)	N_{H2} (kW)	LCOE ($/kWh)	GHG (tonne CO_2 eq./yr)	COE ($/kWh)	GHG (tonne CO_2 eq./yr)
Fargo, ND										
83	190	1	155	0	0	0	0.43	45	NA	NA
Phoenix, AZ										
295	35	48	276	0	0	0	0.56	55	NA	NA

The average monthly LCOEs ($/kWh) of MG components and CG for 100% peak

penetration level in Fargo are shown in Figure 18. The shares of BDG, WT in annual

LCOE were found to be 60% and 20% respectively while those of PV and inverter were

10% each. In case of Phoenix, the shares of BDG and LB were 32% each while those of

PV and inverter were 24% and 10% respectively.
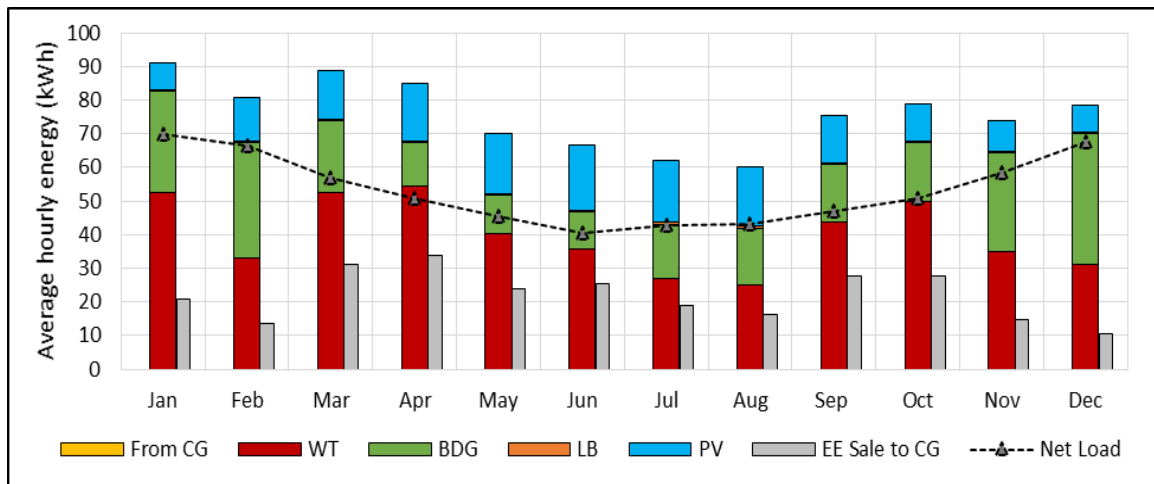
Figure 17 Monthly average of energy provided by MG components and CG for Fargo (100% MG penetration level and SCC of $48 per tonne CO2)
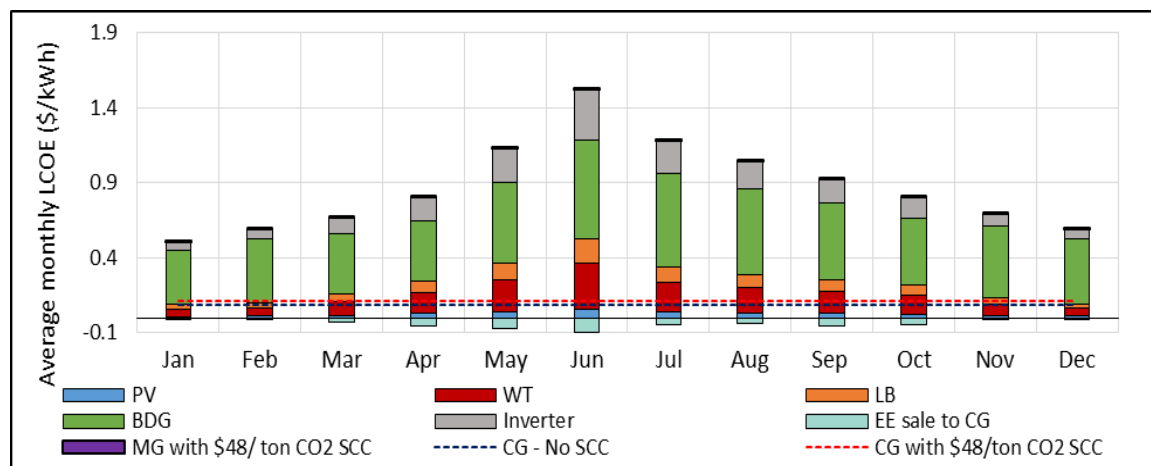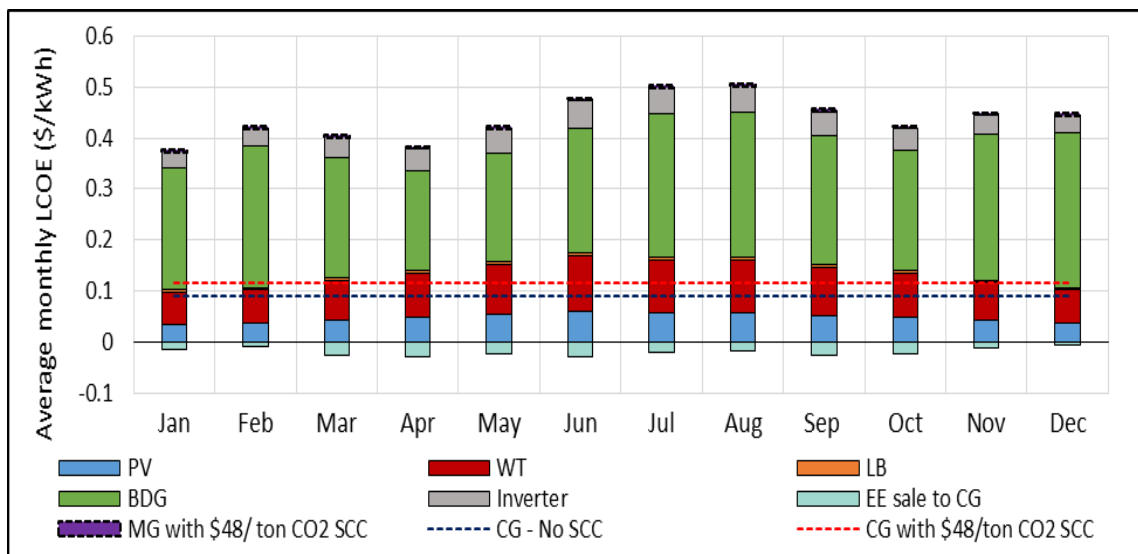

Figure 18 Average monthly LCOE of MG components and CG for Fargo (100% MG penetration level and SCC of $48 per tonne CO2)

For Fargo, the average monthly LCA GHG emissions of MG components and CG for 100% MG penetration level are shown in Figure 19. For both the cities, the shares of

individual components in MG's annual GHG emissions were similar to those of 75%

penetration level.
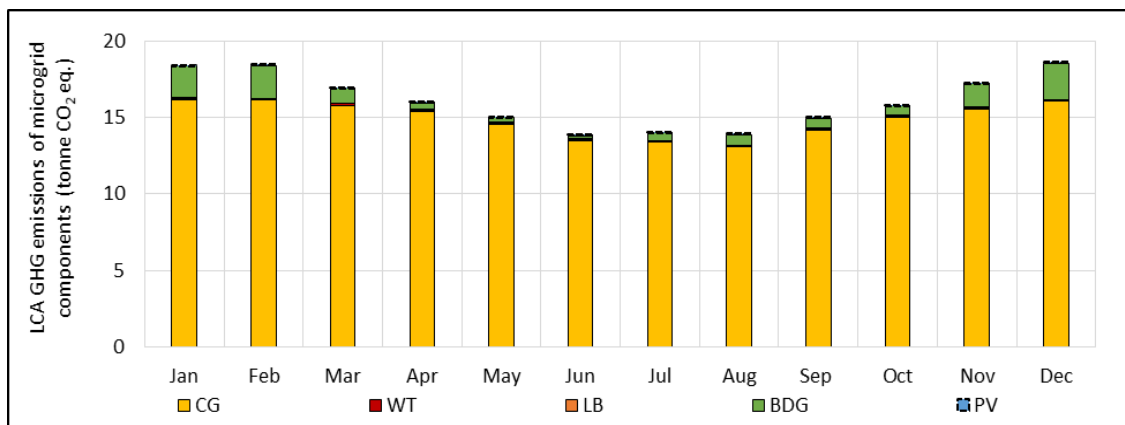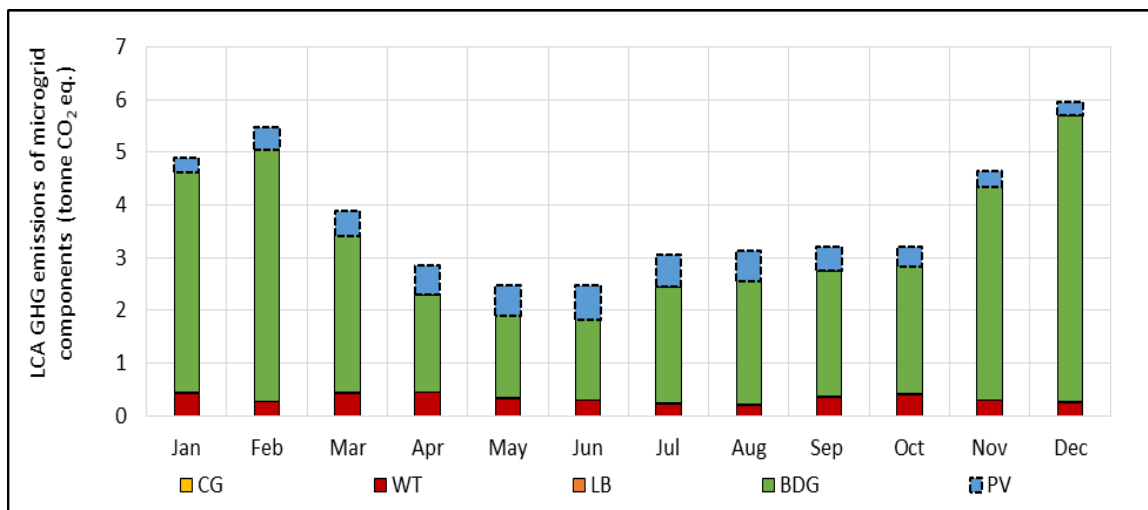

Figure 19 Average monthly LCA GHG emissions (tonne CO2/yr) for Fargo (100% MG penetration level and SCC of $48 per tonne CO2)

For Fargo, it is interesting to note that WT produces maximum amount of energy

within MG (annual share 53%) while also maintaining a LCOE that is 3% less than CG's

retail electricity price. However, for Phoenix, even though three fourths energy was

produced by PVs, its average annual LCOE was 40% more than that of CG's retail price.

5.5. COMPARISON OF MG CONFIGURATIONS AND LCOES BETWEEN FARGO AND PHOENIX FOR ALL PENETRATION LEVELS

The comparison between lowest cost MG configurations between Fargo and

Phoenix for all penetration levels is shown in Figure 20. It is interesting to note that MG

prefers to rely more on BDG units at low penetration levels while at higher penetration

levels more emphasis is placed by MG on PV and WT units. Furthermore, as penetration level increases typically more additions are made to PV or WT capacity than BDG or LB units and the choice between PV and WT depends on the respective city's renewable energy potential.

For each of the MG penetration levels, all the three SCC levels ($12, $48, $72 per tonne of CO_2) were imposed for both the cities and its impact on electricity cost are presented for Fargo in Figure 21. It was found that imposing SCC did not have any effect on MG's LCOE nor its MG configuration. This is because as stated earlier, the carbon footprint of MG is very small. However, owing to CG's high carbon footprint, imposing a SCC of $12, $48, $72 increased the CG's electricity rate ($/kWh) by 7%, 27% and 33% respectively for both the cities.
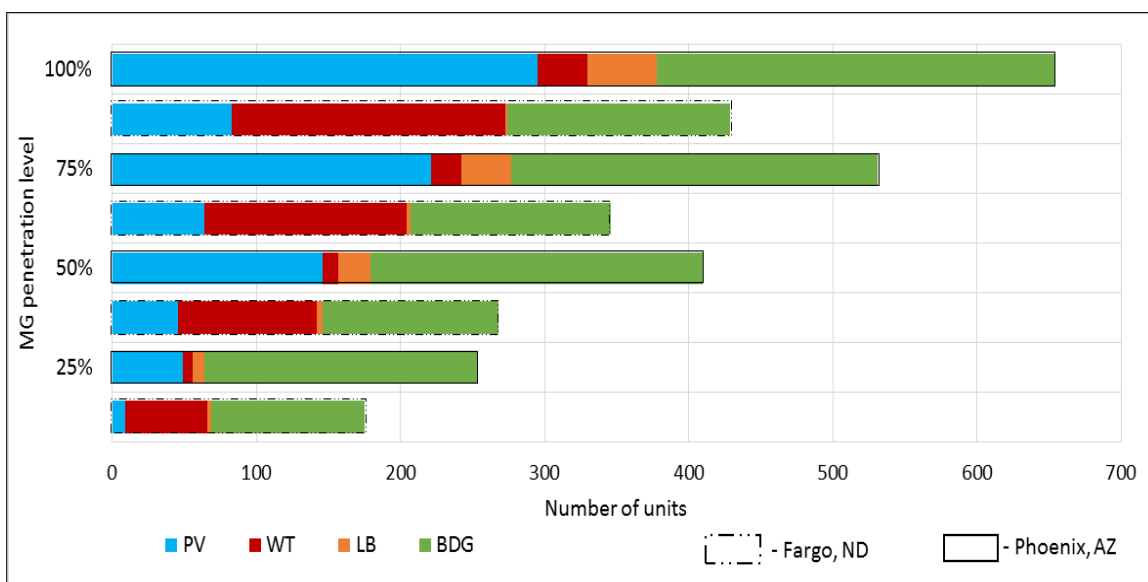
Figure 20 Comparison of lowest cost MG configuration between Fargo and Phoenix for all penetration levels.
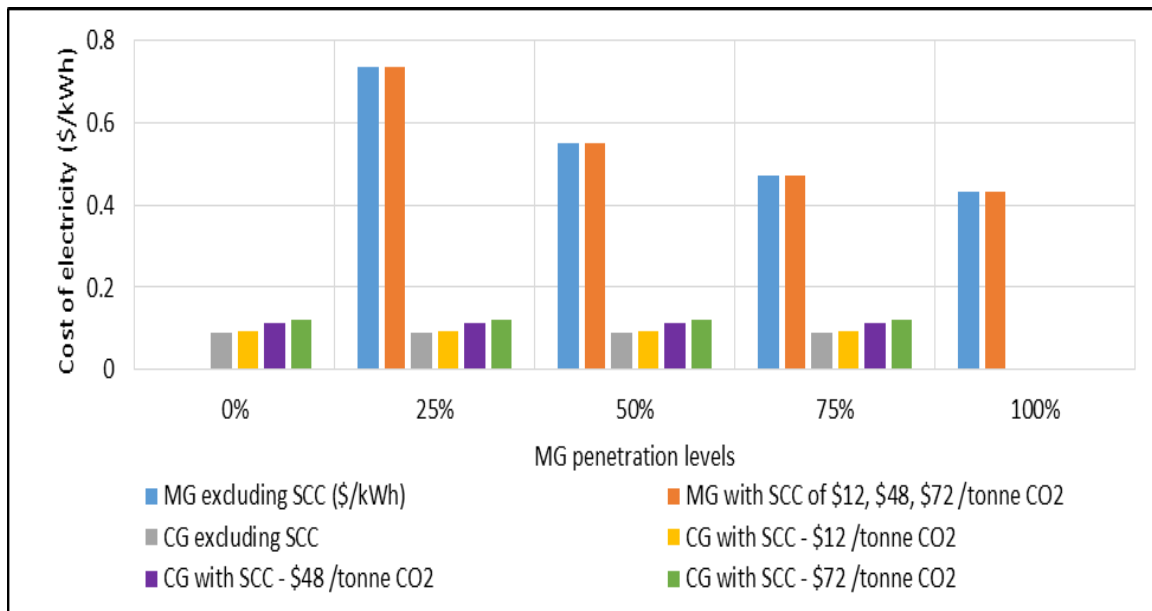
Figure 21 Cost of electricity for MG and CG for all penetration levels along with SCC values ($12, $48, $72) in Fargo.

For Fargo, the LCOE of MG was found to be between 3.8 - 6.4 times as that of CG's retail baseload electricity rate. However, when compared to CG's peak power rate, MG's LCOE was observed to be 5 - 40% smaller [18, 19] thereby formulating a strong case for MG in terms of economic feasibility with respect to CG.

5.6. EFFECT OF CARBON TAX (SCC) ON LCOE OF FARGO AND PHOENIX

A simple analysis was conducted that adds the carbon tax to the electricity cost based on the amount of annual emissions emitted due to power production.

The values of carbon tax were varied and a power cost comparison was made between a standalone MG and a CG for both the cities.
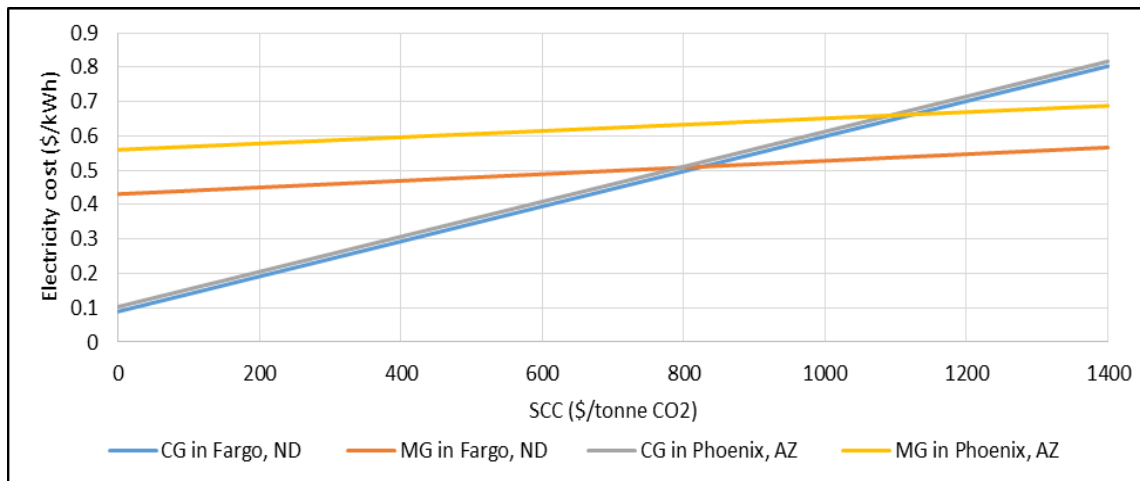
Figure 22 Effect of carbon tax (SCC) on LCOE of Fargo and Phoenix

The results of this analysis are shown in Figure 22 and there are two characteristics that need to be noted. The y-intercept of line is the LCOE of a standalone MG (or retail cost in case of CG) and hence its value depends on location of MG. The slope of line is indicative of annual GHG emissions emitted by a grid (MG or CG). Higher are the annual emissions, steeper are the lines' slopes which in turn indicate higher sensitivity of SCCs to electricity cost. The results of this analysis reinforce our intuitive viewpoints that imposing a carbon tax would drastically affect the electricity cost of CG than MG.

5.7. COMPARISON OF MG LCOES WITH SIMILAR STUDIES IN LITERATURE

The results pertaining to economic assessment of this work were found to be in close agreement with other MG assessment studies across the globe (Table 10). It should be noted that the value of MG is strongly dependent on local capital cost of individual components and these costs can differ significantly from region to region. However, this

comparison is valuable as it evaluates the economic competitiveness of MGs across the

globe. Ensuring global economic feasibility of MGs is crucial in order to tackle the

common environmental challenge of anthropogenic climate change.

Table 10 Comparison of LCOE (adjusted to 2018$) with other studies available in the
literature on small scale MG

Sr No.	Microgrid components	Location	LCOE ($/kWh)	Reference
1.	PV-WT-LB-BDG-FC-H_2	US	0.43 - 0.86	This study
2.	PV	US	0.13 - 0.16	[62]
3.	PV-WT-DG	Singapore	0.19 – 0.30	[17]
4.	PV-WT-Biomass-LB-DG	India	0.25 - 0.27	[63]
5.	PV-WT-FC	Iran	0.55 – 0.81	[21]
6.	PV-WT-DG	Saudi Arabia	0.34	[64]

6. CONCLUSIONS

In this work, a methodology was developed that assessed the techno-economic

and environmental sustainability of a residential community (fifty home) microgrid that

comprised of seven components, namely, PV, WT, LB, BDG, FC, EM and H_2 tanks. This

methodology was implemented for US cities of Fargo and Phoenix and a subsequent

comparison was made.

This study has five main conclusions which can be described as:

1. Based on the regional electricity load profile and availability of renewable

   sources, optimum MG configurations (lowest LCOE) were determined for each

of its grid integration scenarios using a stochastic optimization algorithm known as GA. Four MG-CG grid integration scenarios were examined from peak power standpoint, namely, 25%, 50%, 75% and 100%.

2. The MG's LCOE was obtained to be between $0.43 - 0.86 per kWh. Even though the obtained LCOE was 3.8 – 6.4 times as that of CG's non-peak (baseload) power retail rate, its value was found to be 5-40% lower than CG's peak power rate.

3. Artificial neural network was able to successfully predict the electricity demand of the considered US cities (Fargo and Phoenix).

4. The imposition of carbon tax ($12, $48, $72 per tonne of emitted CO2) did not have any effect on MG's LCOE nor its optimum configuration but increased the CG's electricity rate by nearly 7% - 33%. This occurred due to MG's small footprint which approximately one fifth as that of CG.

5. Increasing the MG's penetration level (from 25% to 100%) was found to lower the LCOE thereby depicting economies of scale effect. The drop in LCOE for Fargo and Phoenix was found out to be 41% and 35% respectively.

As current power generation infrastructure is predominantly based on fossil fuel, it would be immensely difficult to replace them entirely by renewable power generation technologies. There's no silver bullet, but only a silver buckshot approach to meeting energy demands of the future which makes this work valuable.

Future work should be carried out to implement such methodology to other countries such as India, China or Saudi Arabia. An assessment which incorporates the

technical, economic and environmental perspectives would assist the local policymakers

in making informed decisions regarding future energy policies.

REFERENCES

1. https://www.eia.gov/tools/faqs/faq.php?id=427&t=3 [Accessed October 25, 2018]

2. https://www.eia.gov/tools/faqs/faq.php?id=77&t=11 [Accessed October 25, 2018]

3. https://www.nrel.gov/docs/fy13osti/57187.pdf [Accessed October 25, 2018]

4. Colmenar-Santos A et al. Profitability analysis of grid-connected photovoltaic facilities for household electricity self-sufficiency. Energy Policy 2012;51:749–64. DOI: https://doi.org/10.1016/j.enpol.2012.09.023

5. S Shivashankar, S Mekhilef, H Mokhlis, M. Karimi. Mitigating methods of power fluctuation of photovoltaic (PV) sources – a review. Renew Sustain Energy Rev 2016;59:1170–84. DOI: https://doi.org/10.1016/j.rser.2016.01.059

6. Bayod-Rújula A, Haro-Larrodé M, Martínez-Gracia A. Sizing criteria of hybrid photovoltaic-wind systems with battery storage and self-sufficiency considering interaction with the grid. Sol Energy 2013;98:582–91. DOI: https://doi.org/10.1016/j.solener.2013.10.023

7. Li J, Danzer M. Optimal charge control strategies for stationary photovoltaic battery systems. J Power Sour 2014;258:365–73. DOI: https://doi.org/10.1016/j.jpowsour.2014.02.066

8. Jung, M Villaran; Optimal planning and design of hybrid renewable energy systems for microgrids; Renew Sust Energy Rev 2017; 70:180-191. DOI: https://doi.org/10.1016/j.rser.2016.10.061

9. Soshinskaya M, Crijns-Graus WHJ, Guerrero JM, Vasquez JC. Microgrids: experiences, barriers and success factors. Renew Sust Energy Rev 2014;40:659–72. DOI: https://doi.org/10.1016/j.rser.2014.07.198

10. MAM Ramli, HREH Bouchekara, AS Alghamdi. Optimal sizing of PV/wind/diesel hybrid microgrid system using multi-objective self-adaptive differential evolution algorithm, Renew Energy 2018; 121:400-411. DOI: https://doi.org/10.1016/j.renene.2018.01.058

11. C Phurailatpam, BS Rajpurohit, L Wang. Planning and optimization of autonomous DC microgrids for rural and urban applications in India. Renew Sust Energy Rev 2018, 82:194-204. DOI: https://doi.org/10.1016/j.rser.2017.09.022

12. Anastasiadis AG, Vokas G, Papageorgas P, Kondylis G, Kasmas S. Effects of carbon taxation, distributed generation and electricity storage technologies on a microgrid. Energy Procedia 2014;50:824–31. DOI: https://doi.org/10.1016/j.egypro.2014.06.101

13. Mehleri ED, Sarimveis H, Markatos NC, Papageorgiou LG. Optimal design and operation of distributed energy systems: application to greek residential sector. Renew Energy 2013;51:331–42. DOI: https://doi.org/10.1016/j.renene.2012.09.009

14. P. Denholm, M. Hand Grid flexibility and storage required to achieve very high penetration of variable renewable electricity Energy Pol., 39 (3) (2011), pp. 1817-1830. https://doi.org/10.1016/j.enpol.2011.01.019

15. P. Denholm, J.C. King, C.F. Kutcher, P.P.H. Wilson Decarbonizing the electric sector: combining renewable and nuclear energy using thermal storage Energy Pol., 44 (2012), pp. 301-311. https://doi.org/10.1016/j.enpol.2012.01.055

16. C. Cany, C. Mansilla, P. da Costa, G. Mathonnière, T. Duquesnoy, A. Baschwitz Nuclear and intermittent renewables: two compatible supply options? The case of the French power mix Energy Pol., 95 (2016), pp. 135-146. https://doi.org/10.1016/j.enpol.2016.04.037

17. C Shang, D Srinivasan T Reindl. An improved particle swarm optimization algorithm applied to battery sizing for stand alone hybrid energy power systems. Electrical Power and Energy systems 2016; 74:104-117. DOI: https://doi.org/10.1016/j.ijepes.2015.07.009

18. S Wijesuriya, MB Paulo, C Tabares-Velasco. Parametric analysis of a residential building with phase change material (PCM)-enhanced drywall, precooling, and variable electric rates in a hot and dry climate, Applied Energy, 2018, 222:497-514. https://doi.org/10.1016/j.apenergy.2018.03.119

19. J. Blanchard, "Smart energy solutions using fuel cells," 2011 IEEE 33rd International Telecommunications Energy Conference (INTELEC), Amsterdam, 2011, pp. 1-8. Doi: 10.1109/INTLEC.2011.609988

20. A Maleki, A Aksarzadeh. Artificial bee swarm optimization for optimum sizing of a stand-alone PV/WT/FC hybrid system considering LPSP concept. Solar Energy 2014; 107:227-235. DOI: https://doi.org/10.1016/j.solener.2014.05.016

21. R Hosseinalizadeh, H Shakouri, M Amalnick, P Taghipour; Economic sizing of a hybrid (PV-WT-FC) renewable energy system (HRES) for standalone usages by an optimization simulation model: Case study of Iran; Renew Sust Energy Rev 2016, 54:139-150. DOI: https://doi.org/10.1016/j.rser.2015.09.046

22. https://rredc.nrel.gov/solar/old_data/nsrdb/1991-2005/tmy3/by_state_and_city.html [Accessed October 25, 2018]

23. Iqbal M. An introduction to solar radiation, Canada Academic Press, 1983, ISBN 0-12-373752-4.

24. De Miguel A, Bilbao J, Aguiar R, Kambezidis H, Negro E. Diffuse solar model evaluation in the North Mediterranean belt area. Sol Energy 2001; 70(2):143-53. DOI: https://doi.org/10.1016/S0038-092X(00)00135-3

25. T. M. Klucher, "Evaluation of models to predict insolation on tilted surfaces," Solar Energy, vol. 23, no. 2, pp. 111–114, 1979. DOI: https://doi.org/10.1016/0038-092X(79)90110-5

26. JA Duffie, W Beckman, Solar Engineering of Thermal Processes, 2013, Wiley, ISBN 978-1-118-43348-5

27. System Advisor Model Version 2017.1.17 (SAM 2017.1.17). National Renewable Energy Laboratory. Golden, CO. [Accessed October 25, 2018]

28. S Diaf, G Notton, M Belhamel, M Haddadi, A Louche, Design and techno-economical optimization for hybrid PV/wind system under various meterological conditions, Applied Energy 2008, 85:968-987. DOI: https://doi.org/10.1016/j.apenergy.2008.02.012

29. M.Mohammadi, S.H.Hosseinian, G.B.Gharehpetian. Optimization of hybrid solar energy sources/wind turbine systems integrated to utility grids as microgrid (MG) under pool/bilateral/hybrid electricity market using PSO. Solar Energy 2012, 86:112-125. DOI: https://doi.org/10.1016/j.solener.2011.09.011.

30. Tina G, Gagliano S, Raiti S. Hybrid solar/wind power system probabilistic modelling for long-term performance assessment. Solar Energy 2006, 80:578-88. DOI: https://doi.org/10.1016/j.solener.2005.03.013.

31. https://www.nrel.gov/grid/wind-toolkit.html [Accessed October 25, 2018]

32. C Zhang, Y Wei, PF Cao, MC Lin, Energy storage system: Current studies on batteries and power condition system, Renew Sustain Ener Rev 2018, 82:3091-3106. DOI: https://doi.org/10.1016/j.rser.2017.10.030

33. O Gergaud, G Robin, B Multon, HB Ahmed. Energy Modeling of a Lead-Acid Battery within Hybrid Wind/Photovoltaic Systems. European Power Electronic Conference 2003, Sep 2003, TOULOUSE, France. 8pp, 2003.

34. D Guasch, S Silvestre. Dynamic battery model for photovoltaic applications, Prog. Photovolt: Res. Appl. 2003; 11:193–206, DOI: 10.1002/pip.480

35. Bagen, Billington R. Evaluation of different operating strategies in small stand alone power systems. IOEEE Trans Energy Convers 2005; 20(3):654-60. DOI: 10.1109/TEC.2005.847996

36. De Bosio F, Luna AC, Ribeiro L, Graells M, Saavedra OR, Guerrero JM. Analysis and improvement of the energy management of an isolated microgrid in Lencois island based on a linear optimization approach, IEEE; 2016. DOI: 10.1109/ECCE.2016.7854871

37. R Dufo-Lopez, JL Agustin. Multi-objective design of PV-wind-diesel-hydrogen-battery systems. Renew Energy 2008, 33:2559-2572. DOI: https://doi.org/10.1016/j.renene.2008.02.027

38. YA Katsigiannis, PS Georgilakis, ES Karapidakis. Multiobjective genetic algorithm solution to optimum economic and environmental performance problem of small autonomous hybrid power systems with renewables. IET Renew Power Gener 2010, 4(5),404-419. DOI: 10.1049/iet-rpg.2009.0076

39. S. Yerramalla, A. Davari, A. Feliachi, T. Biswas Modeling and simulation of the dynamic behavior of a polymer electrolyte membrane fuel cell, J Power Sources, 124 (1) (2003), pp. 104-113. DOI: https://doi.org/10.1016/S0378-7753(03)00733-X

40. Z Abdin, CJ Webb, EMA Gray. PEM fuel cell model and simulation in Matlab-Simulink based on physical parameters 2016. Energy 116:1131-1144. DOI: 10.1016/j.energy.2016.10.033

41. https://www.iea.org/publications/freepublications/publication/essentials6.pdf

42. CH Li, XJ Zhu, GY Cao, S Sui, MR Hu. Dynamic modeling and sizing optimization of standalone photovoltaic power systems using hybrid energy storage technology. Renewable energy 2009, 34:815-26. DOI: https://doi.org/10.1016/j.renene.2008.04.018

43. K. Agbossou, M. L. Doumbia and A. Anouar, Optimal hydrogen production in a stand-alone renewable energy system, Fourtieth IAS Annual Meeting. Conference Record of the 2005 Industry Applications Conference, 2005., 4:2932-36. Doi: 10.1109/IAS.2005.1518876

44. Yuan, J., Farnham, C., & Emura, K. (2017). Inter-building effect and its relation with highly reflective envelopes on building energy use: Case study for cities of Japan. Atmosphere, 8(11), 211. https://doi.org/10.3390/atmos8110211.

45. J Yuan, C Farnham, C Azuma, K Emura. Predictive artificial neural network models to forecast the seasonal hourly electricity consumption for a University Campus, Sustainable cities and society, 2018, 42:82-92. https://doi.org/10.1016/j.scs.2018.06.019

46. https://openei.org/datasets/files/961/pub/RESIDENTIAL_LOAD_DATA_E_PLUS_OUTPUT/BASE/ [Accessed October 25, 2018]

47. R Dufo-Lopez, JL Bernal Agustin, F Mendoza. Design and economical analysis of hybrid PV-wind systems connected to the grid for the intermittent production of hydrogen. Energy policy. 2009. 37:3082-3095. DOI: https://doi.org/10.1016/j.enpol.2009.03.059

48. https://www.afdc.energy.gov/fuels/prices.html [Accessed October 25, 2018]

49. www.wholesalesolar.com/ [Accessed October 25, 2018]

50. https://www.absolutegenerators.com/american-built/watts/2000-3999-watts/fuel-type/diesel [Accessed October 25, 2018]

51. http://www.fuelcellstore.com/fuel-cell-stacks/high-power-fuel-cell-stacks [Accessed October 25, 2018]

52. http://www.airgas.com/p/HY%20300 [Accessed October 25, 2018]

53. Greenhouse gases, Regulated Emissions, and Energy use in Transportation Model. (GREET Version 2016.1.3.0.13245). UChicago Argonne Laboratory. [Accessed October 25, 2018]

54. IAWG Technical Update of the Social Cost of Carbon for Regulatory Impact Analysis Under Executive Order 12866 (US Government, 2013).

55. Anthoff, D. & Tol, R. S. J. The uncertainty about the social cost of carbon: a decomposition analysis using fund. Climatic Change 117, 515–530 (2013).

56. Moore, F. C. & Diaz, D. B. Temperature impacts on economic growth warrant stringent mitigation policy. Nat. Clim. Change 5, 127–131 (2015).

57. Pindyck, R. S. The Social Cost of Carbon Revisited (National Bureau of Economic Research, 2016).

58. K Ricke, L Drouet, K Caldeira, M Tavoni. Country-level social cost of carbon. Nature Climate Change. 2018,8:895-900. DOI: https://doi.org/10.1038/s41558-018-0282-y

59. http://www.praxair.com/-/media/corporate/praxairus/documents/specification-sheets-and-brochures/gases/hydrogen/hydrogen-h2-spec-sheet-ss-p4604.pdf?la=en [Accessed October 25, 2018]

60. http://www.neo.ne.gov/statshtml/204.htm [Accessed October 25, 2018]

61. A Mahesh, KS Sandhu, A genetic algorithm based improved optimal sizing strategy for solar-wind-battery hybrid system using energy filter algorithm, Front Energy, 2017, 1-13. DOI: https://doi.org/10.1007/s11708-017-0484-4

62. R Fu, D Feldman, R Margolis, M Woodhouse, K Ardani. The U.S. Solar Photovoltaic System Cost Benchmark: Q1 2017, NREL, 2017.

63. Y Sawle, SC Gupta, AK Bohre, Optimal sizing of standalone PV/Wind/Biomass hybrid system using GA and PSO Optimization technique, Energy Procedia, 2017, 117,690-698. DOI: https://doi.org/10.1016/j.egypro.2017.05.183

64. M.A. Mohamed, A.M. Eltamaly, A.I. Alolah. Sizing and techno-economic analysis of stand-alone hybrid photovoltaic/wind/diesel/battery power generation systems, J Renew Sustain Energy, 7 (6) (2015). DOI: https://doi.org/10.1063/1.4938154

III. TECHNO-ECONOMIC ASSESSMENT OF THE SUPERCRITICAL BIODIESEL PRODUCTION PROCESS PLANT LOCATED IN THE MIDWEST REGION OF THE US

Prashant Nagapurkar[a], Joseph D. Smith[a]

[a]Chemical and Biochemical Engineering department, Missouri University of Science and

Technology, Rolla-65401,MO, USA

ABSTRACT

A supercritical biodiesel production process from waste cooking oil (WCO) using methanol in the presence of propane as a co-solvent has been technically analyzed using Aspen Plus software. The presence of the co-solvent propane reduced the severity of supercritical conditions required for the transesterification reaction which was carried out at 280 ^{0}C and 128 bar with a residence time of 8.35 minutes and with a realistic conversion rate of triglycerides to biodiesel of 97.8%. Based on the technical results, an economic assessment of the process was carried out for a small production capacity plant (10,600 ton/yr) as well as for a large capacity plant (128,000 ton/yr) in order to capture the effect of economies of scale on sustainability. The cash flow analysis and breakeven point analysis proved the ability of the supercritical biodiesel production process to thrive even when the purchase price of WCO increased or decreased by 50%.

HIGHLIGHTS

- Techno-economic analysis of biodiesel production from WCO with co-solvent was done.

- Two plant capacities were analyzed – 10,600 ton per year and 128,000 ton per year.

- Analysis was done to capture the effect of economies of scale on sustainability.

- Plants of both capacities in Midwest region of the US were economically feasible.

- Results were compared with other biodiesel production pathways.

1. INTRODUCTION

The transportation sector is heavily reliant on conventional diesel as a fuel source. However, the challenges associated with the rapid depletion of fossil fuel sources coupled with concerns regarding climate change have spurred the development of renewable and sustainable liquid fuel alternatives that can displace conventional diesel. Biodiesel is an example of such an alternative with a low carbon intensity as it emits 78% less carbon dioxide and 35% less carbon monoxide than conventional diesel on a life cycle basis [1]. Biodiesel also exhibits more favorable combustion performance characteristics than conventional diesel by possessing higher Cetane numbers. Furthermore, it is also biodegradable and benign in nature [2]. All of these attributes make a compelling case for biodiesel as a preferred sustainable transportation fuel over conventional diesel.

Biodiesel can be defined as monoalkyl esters of long chain fatty acids derived from renewable lipids feedstock, such as vegetable oil or animal fats. They can be synthesized using approaches broadly classified as follows: homogeneous catalytic,

heterogeneous catalytic, enzymatic, supercritical (catalytic and non-catalytic) and microwave assisted production processes [3-5]. Out of these methods, research efforts during the past decade have been primarily focused on generating biodiesel via non-catalytic transesterification of triglycerides (soybean oil, waste cooking oil, etc.) under supercritical conditions. Under these conditions, the transesterification reaction is carried out at temperatures 280-400 ^{0}C and pressures 100-300 bar along with a high alcohol to triglyceride molar ratio of 42:1 [4]. Over the catalytic approach the supercritical route has shown distinct advantages, such as high reaction rates and no requirement of catalysts. It also permits simultaneous triglyceride transesterification and free fatty acid (FFA) esterification, which reduce the number of processing steps, thereby increasing the production efficiency [5]. Additionally, the supercritical production route is relatively insensitive to the presence of water and FFA content in the reaction mixture and can also accommodate a wide variety of triglyceride feedstocks [4].

At ambient conditions, a mixture of methanol and triglycerides result in the formation of two distinct liquid phases due to their dissimilar size and polarity [6]. However, under supercritical conditions the density of methanol increases which reduces its polarity. As a result of this, the mass transfer resistance between the triglycerides and methanol will decrease resulting in the formation of a single homogenous phase [7,8]. Deslandes et al found that the solubility parameter of methanol becomes closer to that of vegetable oils under appropriate conditions of temperature and pressure [9]. Furthermore, Ma et al concluded that the solubility of methanol in triglycerides increases by 2-3% (mass basis) for every 10 ^{0}C rise in temperature [10]. Both of these studies point towards

the favorability of supercritical conditions as compared to ambient temperature and pressure conditions.

A conventional supercritical biodiesel production process requires a high alcohol to triglyceride ratio (42:1). Also, taking into account the elevated temperature (350 ^{0}C) and pressure (200 bar) requirements, costs rise substantially due to heating, pumping and recycling of alcohol [4,11]. This is a major limitation of the supercritical pathway which hinders its implementation on an industrial scale. Hence, current research is being directed to alleviate the temperature and pressure conditions required for the supercritical process. One of the ways to accomplish this is by addition of a co-solvent to the reaction mixture. It has been shown that addition of carbon dioxide (CO_2), n-hexane and propane reduces the severity of supercritical conditions [4]. Studies show that adding CO_2 as a co-solvent in the methanolysis of soybean oil, a 98% yield of biodiesel was obtained at 280 ^{0}C and 143 bar with a methanol to oil ratio of 24:1 and CO_2 to methanol ratio of 1:10 [12]. However, the biodiesel yield decreased as temperature and CO_2 to methanol ratio decreased. A different study found that during ethanolysis of soybean oil in a micro reactor, the addition of CO_2 had a positive effect on the yield of fatty acid ethyl esters. The reaction was performed at 325 ^{0}C, 200 bar with an ethanol to oil molar ratio of 20:1 and CO_2 to ethanol ratio of 1:5 [13]. Additionally, Muppaneni et al reported that n-hexane can be used as a co-solvent in producing biodiesel from Camelina oil under reduced supercritical conditions of 295 ^{0}C and 100 bar with n-hexane to oil ratio of 1:5 [14]. The biodiesel produced in this study also met the ASTM fuel quality standards. Cao et al found that 98% yield of biodiesel could obtained at reduced temperature and pressure conditions of 280 ^{0}C and 128 bar by adding propane to the reaction mixture. The

propane to methanol ratio and oil to methanol ratio was maintained at 1:20 and 1:24 respectively. This study showed that a complete conversion of biodiesel could be achieved at 300 ^{0}C.

In the available literature there are numerous studies which are focused on evaluating the techno-economic feasibility of biodiesel production via supercritical route. For example, using Aspen HYSYS one study simulated and made a comparison of four pathways to produce biodiesel. The pathways analyzed were the homogenous acid catalyzed pathway, alkali catalyzed pathway, heterogeneous acid catalyzed pathway and conventional supercritical production pathway. Results of this study for an 8,000 ton/yr plant showed that the after tax rate of return (ATROR) for conventional supercritical biodiesel process was -0.9% deeming the process to be economically unfeasible [15]. Similar analysis was conducted for a 36,000 ton/yr capacity plant situated in Argentina and the authors concluded the project to be unprofitable as it yielded a negative net present value (NPV) [16]. Some techno-economic studies available in the literature focus on supercritical biodiesel production processes employed thermodynamic models, which were unsuitable for the process conditions [17,18]. In addition, insufficient heat integration for the supercritical process was performed in certain studies [15,16,19]. As supercritical process takes place at high temperature and pressure, optimum design of a heat integration scheme is extremely vital to achieve economic sustainability of the process.

All the above mentioned studies evaluated the supercritical biodiesel production process in the absence of a co-solvent and its alleviating effect on temperature, pressure and methanol to oil ratio. There are very few studies that are devoted to assessing the

techno-economic feasibility of supercritical biodiesel production with the addition of a

co-solvent. Nisworo et al conducted a techno-economic feasibility study of a supercritical

biodiesel production using a co-solvent and determined the plant to be financially

profitable [18]. But this study assumed almost a complete conversion (>99%) of

triglyceride to biodiesel, which is unrealistic, and used thermodynamic models which

were not appropriate for process conditions. For instance, the process employed the

UNIQUAC fluid package for simulating high pressure systems instead of the

recommended fluid packages such as SRK, PSRK, etc. [8]. For a plant situated in

Europe, similar techno-economic analysis of the supercritical process was done wherein

the steam requirements were met by combusting the generated biodiesel in the boiler unit.

As a result of this, the process became self-sufficient in terms of energy, but the cost of

generating steam from biodiesel as compared to natural gas is very high. For instance, in

Europe the average cost of natural gas was $7/GJ whereas the cost of biodiesel was

$28/GJ in 2017 [20]. The authors did not take this factor into account during their

analysis which would have further reduced the plant's operating costs. Nonetheless, their

economic feasibility study deemed the supercritical process as financially viable process

for the annual production capacity of 10,000 ton of biodiesel [21].

The aim of this work is to conduct a techno-economic assessment of a

supercritical biodiesel production process from waste cooking oil (WCO) using propane

as a co-solvent for a plant located in the Midwest region of the US. The plant was

assumed to be situated in the Midwest region because it accounted for nearly 66% of the

total biodiesel produced in the US in 2017 [22]. In order to assess the impact of

economies of scale on the breakeven selling price of biodiesel, two independent process

simulations of annual biodiesel production capacities – 10,600 ton and 128,000 ton were performed using Aspen Plus. Suitable thermodynamic fluid packages were employed for simulating high pressure units.

The technical and economic assessment results of the processes were compared with each other and also with other existing biodiesel production processes. The generated biodiesel adhered to the US (ASTM D6751) and European (EN14214) fuel quality standards. Glycerol produced was purified to meet pharmaceutical grade standards (>99.5% purity). A detailed heat integration was also performed to reduce and optimize operating costs.

2. METHODOLOGY

A process simulation scheme of the supercritical biodiesel process is described in this section. Based on the technical design, an economic evaluation of the biodiesel production process is performed to assess economic sustainability.

The overall process has been broken down into five sections, namely, feed preheating section, reactor section, methanol recovery section, methyl oleate purification section, and glycerol purification section. The design and simulation of supercritical biodiesel production processes explained in this work have been primarily described using the process flowsheets standpoint for a 10,600 ton capacity plant.

The flowsheet is the same for both plant capacities (10,600 ton/yr and 128,000 ton/yr), except for some auxiliary units such as heat exchangers and pumps.

The exact differences, if any, in case of 128,000 ton plant capacity are specified in the corresponding description of process plant sections.

2.1. PROCESS SIMULATION

Aspen Plus v10 software was used to simulate a continuous and steady state supercritical biodiesel production process. For the purpose of simulation, annual plant capacities of 10,600 tons and 128,000 tons of biodiesel were considered along with operational runtime of 347 days. The procedure to develop this model involved defining components, evaluating and incorporating a suitable thermodynamic fluid package, and establishing optimum equipment and operating conditions. Mass and energy balances were conducted for every block in the flowsheet. Pressure drop across units was assumed to be negligible.

2.1.1. Key Components. Based on existing studies in the literature, triolein ($C_{57}H_{104}O_6$) and methyl oleate ($C_{19}H_{36}O_2$) were assumed to represent WCO and biodiesel respectively [15,16,18,21]. Methanol (CH_4O) was chosen as the reactant in the process instead of ethanol, butanol, iso-propanol, etc. due to its high reactivity and low cost [5]. As mentioned earlier, propane (C_3H_8) was used as a co-solvent as it has been shown to reduce the severity of harsh supercritical conditions [23]. Along with methyl oleate, in the transesterification reaction glycerol ($C_3H_8O_3$) was also generated as a by-product.

2.1.2. Thermodynamic Fluid Package. Identifying and using the correct thermodynamic package is extremely vital to accurately simulate any chemical process. Generally, UNIQUAC (Universal Quasi-Chemical) is suitable for units operating at low temperature and pressure (up to 5 bar).

For supercritical conditions of temperature and pressure UNIQUAC is not a suitable thermodynamic package [24]. However, Nisworo et al have employed UNIQUAC fluid package to simulate supercritical biodiesel production process [18].

Glisic et al have utilized RK-EOS (Redlich Kwong equation of state) model as it has been shown to better predict liquid-vapor equilibrium properties of triglycerides than other packages [8]. But in order to use this package, some missing parameters need to be correlated with the help of experimental data. Thermodynamic fluid packages such as Predictive Soave Redlich Kwong (SRK) or Soave Redlich Kwong (SRK) can be used to simulate this process under supercritical conditions [25]. Therefore in this work, the Soave Redlich Kwong (SRK) package has been used to simulate high temperature and pressure blocks (>5 bar) while the UNIQUAC fluid package is used to simulate low temperature and pressure units [21].

      2.1.3. Reactor and Kinetic Data. A single step irreversible transesterification reaction (single order with respect to triolein) was assumed to occur between triolein and methanol to produce methyl oleate and glycerol. A power law kinetic expression was adopted to model the reaction in a plug flow reactor. The experimental values reported in the literature for kinetic parameters are shown in Table 1. Furthermore, optimum reaction conditions such as temperature, pressure, oil to methanol ratio and propane to methanol ratio are also mentioned in Table 1 [7,18].

      Some of the recent studies published in the literature focusing on analyzing a supercritical process assumed a near complete conversion of triglycerides to biodiesel (>99.5%) [18, 26]. However, this conversion is not realistic as most of the experimental findings suggest a conversion in the range of 97-98% [15, 21, 27]. Therefore, based on supercritical reactor design studies available in the literature, the dimensions of the plug flow reactor were calculated in such a way that conversion resides in the range 97-98% [18, 21].

Table 1 Kinetic and reaction parameters for transesterification reaction [7, 18]

Parameters	Units	Value
Temperature	º C	280
Pressure	bar	128
Oil : Methanol	Molar ratio	1:24
Propane : Methanol	Molar ratio	1:20
Activation energy	kJ/kmol	38,482
Heat of reaction	kJ/s	3.2×10^{-2}
Kinetics constant	s^{-1}	7×10^{-3}
Residence time	mins	8.35

Table 2 Dimensions of plug flow reactor [18, 21]

Parameters	Units	Plant capacity	
		10,600 ton/yr	128,000 ton/yr
Tube diameter	m	0.10	0.10
Tube length	m	55	60
Number of tubes		2	21
Reactor volume	m^3	0.86	9.9

The exact molar conversion was calculated to be 97.8%. The reactor dimensions for both the plant capacities are shown in Table 2. The reactor volume required for annual capacity of 128,000 ton (9.90 m^3) was approximately 11 times than that required for the 10,600 ton (0.86 m^3) capacity.

2.2. PROCESS DESCRIPTION

Two processes of different annual capacities were designed and simulated.

A small capacity of 10,600 ton and a large capacity of 128,000 ton per year of biodiesel production were analyzed.

The process flowsheets for both the capacities are shown in Figure 1 and Figure 2 respectively.

Their corresponding mass and energy balances are also depicted in Table 3 and Table 4.
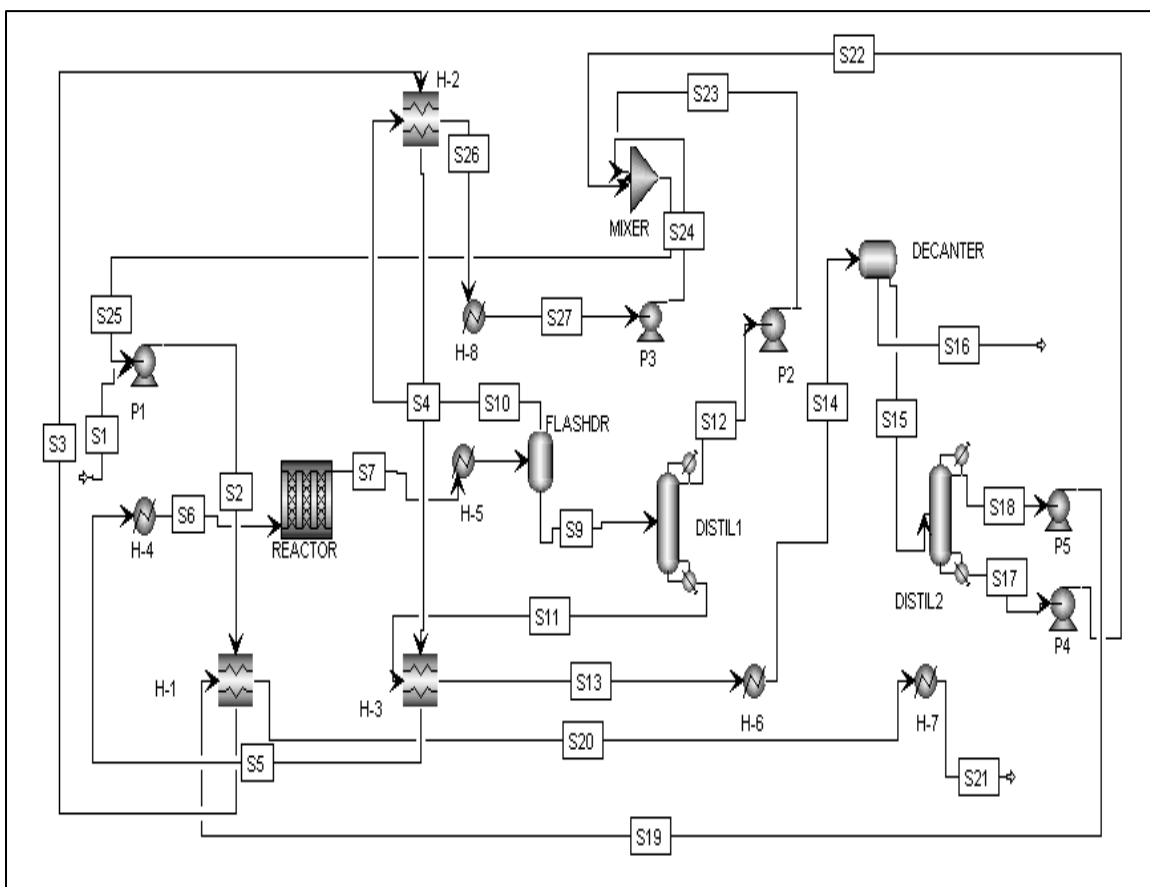
Figure 1 Process flowsheet for annual biodiesel production capacity of 10,600 tons
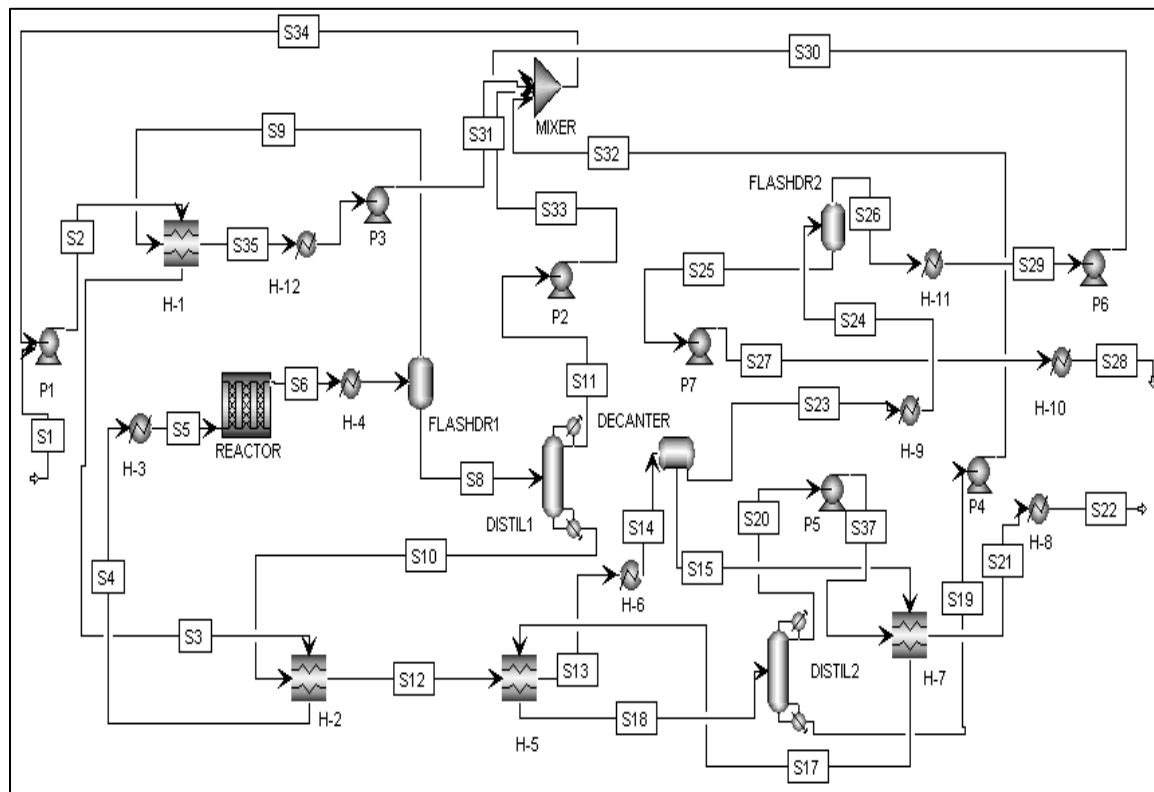
Figure 2 Process flowsheet for annual biodiesel production capacity of 128,000 tons

2.2.1. Methanolysis Section or Reactor Section. The transesterification reaction between triolein and methanol to produce methyl oleate and glycerol was carried out in an adiabatic plug flow reactor at 280 ^{0}C and 128 bar.

The molar ratios of oil to methanol and propane to methanol in the reactor were maintained at 1:24 and 1:20 respectively (as illustrated in Table 2). For the case of the 10,600 ton capacity plant, feed (S1) which consists of WCO and fresh methanol is mixed with the recycle stream (S25) consisting of propane and methanol. This mixed stream (S2) is then pumped to 128 bar via high pressure pump P1 before it gets heated through a series of heat exchangers (H-1, H-2, H-3, H-4) which raises its temperature to 280 ^{0}C. Since the methanolysis activity takes place at high temperature and pressure, the SRK

fluid package was necessary to model the reactor, heat exchangers (H-1, H-2, H-3, H-4) and the pump (P1).

Table 3 Mass and Energy balance for plant possessing annual biodiesel production of 10,600 tons

Stream no.	S1	S2	S3	S4	S5	S6	S7	S8	S9	S10	S11	S12	S13	S14
Temperature (°C)	25	72.61	98.76	128.9	216.8	280	280	286	212	212	319	60	143	32
Pressure (bar)	1	128	128	128	128	128	128	128	5	5	1	1	1	1
Mass fraction														
Triolein	0.9019	0.476	0.476	0.476	0.476	0.476	0.0105	0.0105	0.0176	0.0001	0.0183	0	0.0183	0.0183
Methanol	0.0980	0.4362	0.4362	0.4362	0.4362	0.4362	0.3857	0.3858	0.0347	0.9052	0.0003	0.8509	0.0003	0.0003
Methyl Oleate	0	0.0548	0.0548	0.0548	0.0548	0.0548	0.5225	0.5226	0.8634	0.0182	0.8968	0.0716	0.8968	0.8968
Glycerol	0	0.0044	0.0044	0.0044	0.0044	0.0044	0.0529	0.0529	0.0838	0.0072	0.0846	0.0650	0.0846	0.0846
Propane	0	0.0282	0.0282	0.0282	0.0282	0.0282	0.0282	0.0283	0.0005	0.0693	0	0.0126	0	0
Total mass flow rate (ton/hr)	1.405	2.717	2.717	2.717	2.717	2.717	2.717	2.717	1.621	1.095	1.555	0.0654	1.5555	1.5555
Vapor fraction	0	0	0	0	0	0.459	0	0	0	1	0	0	0	0
Liquid fraction	1	1	1	1	1	0.541	1	1	1	0	1	1	1	1
Enthalpy (MW)	-1.21	-3.43	-3.37	-3.31	-3.11	-2.89	-2.89	-2.876	-1.165	-1.710	-0.924	-0.125	-1.124	-1.234

Stream no.	S15	S16	S17	S18	S19	S20	S21	S22	S23	S24	S25	S26	S27
Temperature (°C)	35	35	197	148	155	88	35	199	80	120	103	114	97
Pressure (bar)	1	1	0.01	0.01	10	10	1	10	10	10	10	5	5
Mass fraction													
Triolein	0.020	0	0.17	0.002	0.002	0.002	0.002	0.17	0	0	0.0194	0	0
Methanol	0.003	0.002	0	0	0	0	0	0	0.851	0.9052	0.7989	0.905	0.905
Methyl Oleate	0.977	0	0.83	0.994	0.994	0.994	0.994	0.83	0.072	0.0181	0.1137	0.018	0.018
Glycerol	0.003	0.998	0	0.003	0.003	0.003	0.003	0	0.065	0.0072	0.0092	0.007	0.007
Propane	0	0	0	0	0	0	0	0	0.012	0.0693	0.0585	0.07	0.07
Total mass flow rate (ton/hr)	1.427	0.128	0.150	1.277	1.277	1.277	1.277	0.150	0.065	1.095	1.311	1.0956	1.0956
Vapor fraction	0	0	0	0	0	0	0	0	0	0	0	0.9598	0.0011
Liquid fraction	1	1	1	1	1	1	1	1	1	1	1	0.040	0.9988
Enthalpy (MW)	-981.071	-0.253	-0.085	-0.783	-0.782	-0.837	-0.877	-0.084	-0.125	-2.056	-2.267	-1.775	-2.057

Table 4 Mass and Energy balance of a 128,000 ton capacity biodiesel production plant

Stream no.	S1	S2	S3	S4	S5	S6	S7	S8	S9	S10	S11	S12	S13	S14	S15	S17	S18	S19
Temperature (°C)	25	55	134	185	280	279	295	225	225	257	57.5	153	93	32	35	67	135	198
Pressure (bar)	1	128	128	128	128	128	128	5	5	1	1	1	1	1	1	1	1	0.01
Mass fraction																		

Table 4 Mass and Energy balance of a 128,000 ton capacity biodiesel production plant (cont.)

Triolein	0.901	0.503	0.503	0.503	0.503	0.011	0.011	0.018	0	0.018	0.018	0	0.018	0.018	0.02	0.02	0.02	0.315
Methanol	0.099	0.429	0.429	0.429	0.429	0.375	0.375	0.027	0.883	0.003	0.981	0.003	0.003	0.003	0.002	0.002	0	0
Methyl Oleate	0	0.033	0.033	0.033	0.033	0.528	0.528	0.868	0.032	0.89	0	0.89	0.89	0.89	0.976	0.976	0.975	0.685
Glycerol	0.000	0.005	0.005	0.005	0.005	0.056	0.056	0.087	0.012	0.089	0	0.089	0.089	0.089	0.003	0.003	0.002	0
Propane	0	0.03	0.03	0.03	0.03	0.03	0.03	0	0.072	0	0.019	0	0	0	0	0	0	0
Total mass flow rate (ton/hr)	16.96	30.91	30.91	30.91	30.91	30.91	30.91	18.33	12.59	17.88	0.451	17.88	17.88	17.88	16.31	16.31	16.31	0.9
Vapor fraction	0	0	0	0	0.451	0	0	0	1	0	0	0	0	0	0	0	0	0
Liquid fraction	1	1	1	1	0.549	1	1	1	0	1	1	1	1	1	1	1	1	1
Enthalpy (MW)	-14.6	-39.2	-37.3	-36	-32.7	-32.7	-32.2	-12.9	-19.3	-11.6	-0.91	-12.9	-13.6	-14.3	-11.2	-10.9	-10.2	-0.50

Stream no.	S20	S21	S22	S23	S24	S25	S26	S27	S28	S29	S30	S31	S32	S33	S34	S35	S36	S37
Temperature (° C)	81	55	35	35	141	171	171	134	35	29	57	116	199	85	98	108	96	87
Pressure (bar)	0.01	5	1	1	1	0.2	0.2	1	0.2	0.2	10	10	10	10	10	5	5	5
Mass fraction																		
Triolein	0.002	0.002	0.002	0	0	0	0	0	0	0	0	0	0.315	0	0.02	0	0	0.002
Methanol	0.002	0.002	0.001	0.013	0.013	0.002	0.79	0.002	0.002	0.79	0.79	0.883	0	0.98	0.829	0.883	0.088	0.002
Methyl Oleate	0.992	0.992	0.992									0.323	0.684		0.073	0.032	0.032	0.994
Glycerol	0.002	0.986	0.986	0.997	0.207	0.998	0.207	0.997	0.997	0.208	0.208	0.012	0	0	0.011	0.012	0.012	0.002
Propane	0	0	0	0	0	0	0	0	0	0	0	0.072	0	0.018	0.065	0.072	0.072	0
Total mass flow rate (ton/hr)	15.41	15.41	15.41	1.567	1.567	1.545	0.022	1.545	1.545	0.022	0.022	12.58	0.9	0.45	13.95	12.58	12.58	15.41
Vapor fraction	0	0	0	0	0	0	1	0	0	0.001	0	0	0	0	0	0.669	0.001	0
Liquid fraction	1	1	1	1	1	1	0	1	1	0.999	1	1	1	1	1	0.331	0.999	1
Enthalpy (MW)	-10.14	-0.29	-10.6	-3.10	-3	-2.96	-0.03	-2.96	-3.10	-0.04	-0.04	-23.3	-0.50	-0.90	-24.8	-21.1	-23.3	-10.1

2.2.2. Methanol Recycling. Product stream (as shown in Figure 1 as S7) emanating from the reactor consisting of methyl oleate, propane, unreacted triolein and methanol is then flashed in a vertical drum (Flashdr) at 5 bar in which 95% of the unreacted methanol is evaporated. Instead of providing heat to a flash drum by means of heating coils, a heat exchanger (H-5) is used to heat the feed entering the flash drum so that only the process of flashing can take place in the vertical vessel. The vapor stream (S10) coming out from the flash drum is condensed by means of two heat exchangers (H-2 and H-8) and recycled back to the fresh feed through pump P3. The liquid stream (S9) exiting the flash drum is fed to the distillation column (Distil1) to remove the remaining amount of unreacted methanol.

This distillation column possesses three sieve trays and is operated at atmospheric pressure with a molar reflux ratio of 2. Distillate (S12) produced at the top of the column (Distil1) is then pressurized to 10 bar through pump P2 and then recycled back to the fresh feed. Thermodynamic fluid package, UNIQUAC, was used to model the flash drum (Flashdr1) and distillation column (Distil1) as their operating pressures are low (close to 5 bar).

2.2.3. Purification of Methyl Oleate (Biodiesel). The bottom product of distillation column (S11) consisting of methyl oleate and glycerol is cooled to 35 ^{0}C through a series of heat exchangers (H3, H6) before it gets introduced into the decanter.

The decanter separates glycerol and methyl oleate based on their density difference. Glycerol of 99.7% purity is obtained after separation via stream S16. The upper layer stream (S15) exiting the decanter, comprised mainly of Methyl Oleate, is fed to the distillation column (Distil2) which purifies it to 99.4%. The distillation column is

operated at 0.01 bar and possesses 15 stages along with a reflux ratio of 2.The main purpose of this distillation column is to separate unconverted triglycerides (triolein) from methyl oleate (biodiesel). The methyl oleate exiting from the top of distillation column (S12) adheres to US (ASTM D6751) and European (EN14214) fuel quality standards commonly called as B100. As the distillation column is operating under vacuum conditions, UNIQUAC is employed as a suitable thermodynamic fluid package.

2.2.4. Glycerol Purification. For the case of biodiesel plant with annual production of 10,600 ton, single decanter is sufficient to produce pharmaceutical grade glycerol (>99.5%) as shown in Figure 1. However, in the case of the larger plant (128,000 ton/yr) a decanter alone is not sufficient enough to produce pharmaceutical grade glycerol as trace amounts of methanol are still present in the glycerol rich decanter exiting stream (S23) as shown in Figure 2.

An additional vapor liquid separation stage is necessary to achieve the desired purity of glycerol. Hence, the stream S23 coming out from the decanter is heated via heat exchanger (H-9) prior to its introduction in the flash drum (Flashdr2) at a pressure and temperature of 0.2 bar and 172^0C respectively. The liquid stream (S25) consisting of pharmaceutical grade glycerol is then cooled by means of a water cooler (H10) to 35^0C. The top vapor stream (S26) emanating from the flash drum (Flashdr2) containing methanol vapors is condensed via a condenser (H-11) and subsequently pumped to 10 bar via P6 and is recycled back to the fresh methanol feed. As the flash drum was operated at a pressure of 0.2 bar, UNIQUAC fluid package was utilized to simulate the process conditions.

2.2.5. Heat Integration. Heat integration for the process was performed to reduce the utility costs and enhance energy efficiency for the biodiesel production process. Counter current heat exchangers were designed with a minimum logarithmic mean temperature difference (LMTD) of 15 ^{0}C which would allow a sufficient driving force for thermal energy transfer [28]. A proven 'from inside to outside' approach was used to design the heat integration network for the process [25].

In the first step, high temperature hot streams are used to heat high temperature cold streams in such a way that streams which are closest to each other in terms of thermal energy levels are coupled with each other in a countercurrent shell and tube heat exchanger. For instance, in the case of the 10,600 ton plant, a high temperature cold stream S2 at the temperature of 73 ^{0}C is heated by means of the next available high temperature hot stream S19 at 115 ^{0}C as they are closest to each other in terms of thermal energy levels.

After completing the energy analysis for the first pair of streams, a similar procedure is performed by coupling the next available high temperature hot stream with the closest available high temperature cold stream in a countercurrent heat exchanger. Such a procedure is carried out until all the available high temperature hot streams are paired with all the available high temperature cold streams, thereby designing a complete heat exchanger network.

Using this methodology, detailed heat integration analysis was performed to maximize the internal heat flow and minimize the external utility (steam and cooling water) usage.

2.2.6. Utility Design. The supercritical biodiesel production process occurs at elevated conditions of temperature and pressure. Therefore, it is imperative to accurately determine the use of steam and cooling water. In spite of its paramount importance to economic sustainability, previous studies on supercritical biodiesel production have not considered the detailed design of steam generation and cooling systems [29]. In this study, heating and cooling duties of heat exchanger units were acquired from simulation, and the utility usage was estimated based on those values.

The main usage of steam was to heat the reactor feed to 280 ^{0}C and to provide energy to distillation columns via reboilers. For instance, in the case of the 10,600 ton capacity plant, saturated steam was provided to the reactor feed heater – H4 and to the reboilers of both the distillation columns - Distil1 and Distil2. LMTD of at least 20^{0}C was maintained in these heat exchangers and reboilers [28]. Steam was assumed to be generated in a natural gas fired boiler operating at an efficiency of 85% with boiler feed water temperature at 100 ^{0}C. Steam distribution losses of 10% were also taken into account while performing steam calculations [30]. Cooling water was used to condense vapors (to facilitate transportation) and to cool the final products (biodiesel and glycerol) to 35^{0}C. As shown in Figure 1 cooling water is used for condensation purposes in distillation column condensers (Distil1 condenser and Distil2 condenser) and for product cooling purposes (in exchangers H6 and H7).

A minimum LMTD of 5^{0}C was maintained in these heat exchangers along with a cooling water supply and return temperatures of 25 ^{0}C and 40 ^{0}C respectively [28]. Cooling water requirements were then computed based on those values.

2.2.7. Process Economics. The Midwest region of the US is a major producer of biodiesel as it has accounted for over two-thirds of the total biodiesel produced in the United States in 2017. Approximately 39% of the total biodiesel producing plants in the US are located in the Midwest region [22]. Therefore, an economic evaluation of the supercritical biodiesel production process was conducted for plants situated in the Midwest region of the US. Following up on the technical design of supercritical biodiesel production, the economic feasibility study was conducted for two different plant capacities – 10,600 ton/yr and 128,000 ton/yr. Even though the block for filtration of WCO was not shown in the flowsheet (Figure 1 and Figure 2), it is assumed to be present for economic evaluation purposes. Mapping, sizing and costing of all the units shown in the flowsheet (Figure 1 and Figure 2) were performed using the economic evaluation tool available in Aspen Plus v10. All the equipment was assumed to be made up of carbon steel. The direct costs (equipment, materials, labor, etc.) and indirect costs (freight, overheads, insurance, etc.) for the purchased equipments were determined by the economic evaluation tool. Together, these costs are commonly known as bare module costs, or installed costs. However, these bare module costs which were determined by Aspen Plus corresponded to the equipment costs in February 2016. In order to determine the costs in today's value (December 2017) the effect of inflation must be taken into account. This is calculated by means of the following formula [28]:

$$Equipment\ costs\ in\ December\ 2017 = \frac{CEPCI\ in\ December\ 2017}{CEPCI\ in\ February\ 2016} \times Equipment\ costs\ in\ February\ 2016\ (1)$$

The value of CEPCI for December 2017 to perform this computation was taken to be 574 [31]. In this way, all the direct and indirect costs for the itemized equipments were computed by Aspen Plus and adjusted by means of inflationary indices (Chemical

Engineering Plant Cost Index - CEPCI) in terms of today's value. In addition to these costs, contingency costs and auxiliary costs were assumed to be 18% and 50% of the bare module costs [28]. The addition of bare module, contingency and auxiliary costs together constitute the grass roots costs or fixed capital investment of the plant. The number of operator (N_{OL}) required for running the plant in a single shift were estimated using the following formula [28]:

$$N_{OL} = \left(6.29 + 31.75\, P^2 + 0.23\, N_{np}\right)^{0.5} \tag{2}$$

In the above formula, the value of N_{np} is the number of non-particulate processing steps required and the value of P corresponds to the number of solid particle processing steps. The number of actual personnel hired for every operator in a single shift is assumed to be 4.5 and the annual salary of each individual is taken to be $60,000 [28]. Based on these assumptions the annual cost of labor (C_{OL}) is determined. Assuming the WCO feed as a fairly clean feedstock and does not necessitate any major solid processing step, the value of P in the above formula is taken as zero and filtration of WCO is counted as a non-particulate processing step.

The raw material (C_{RT}), product and utility costs are shown in Table 5. The costs of WCO, methanol, propane, and glycerol are obtained from product vendors. The selling cost of biodiesel is its average selling price in the Midwest region [35].

The operating costs for cooling water was the average cost calculated from two different studies [37,38].

The cost of natural gas and electricity shown in Table 5 is its average unit cost for the Midwest region in 2017 [40].

Table 5 Raw material, product and utility costs

Material	Cost
Methanol	$0.5 /kg [32]
WCO	$0.227 /kg [33]
Propane	$268 /kg [34]
Biodiesel	$1.04 /kg [35]
Pharmaceutical grade glycerol	$0.5 /kg [36]
Cooling water costs	$0.04/ton [37,38]
Electricity unit costs	$0.075 /kWh [39]
Cost of Natural gas	$4.66 /GJ [40]
Filtration unit operating costs	$1.07 /hr [28,41]

Operating costs for the filtration unit was the average cost estimated from two different studies [28,41]. Salvage value was estimated as 10% of the total fixed capital investment (FCI). Working capital was estimated 10% of the total costs for FCI, raw materials and labor [28]. Land size of 15 acres and 30 acres was assumed for 10,600 ton and 128,000 ton annual capacity respectively [42]. The cost of land in Midwest region in December of 2017 was determined by referring the online property dealers' online database [43]. The period of plant construction was assumed to be two years. The cost of land was invested at the start of the construction while the FCI was invested gradually in two installments. The share of FCI was spent at the end of the first year was 60% while the rest was spent at the end of the construction period. The annual cost of manufacturing (COM$_d$), excluding depreciation, was calculated using the following formula [28]:

$$COM_d = 0.180 \ FCI + 2.73 \ C_{OL} + 1.23 \ (C_{UT} + C_{WT} + C_{RM})$$

To calculate the annual cost of manufacturing (COM_d), FCI is the fixed capital investment, C_{OL} is the cost of labor, C_{UT} is the utility cost, C_{WT} is the waste treatment cost and C_{RM} is the raw material cost.

Modified accelerated cost recovery system (MACRS) method with a 9.5 year class life and a 5 year recovery period is used to determine the depreciation costs. MACRS technique was adopted because the current US federal tax law is based on that method [28].

The total annual total tax rate (federal plus state) is assumed to be 42%. Using all the assumptions stated above, a cash flow analysis was performed for the period of plant's operational life of 20 years.

In addition, a sensitivity analysis with respect to the price of WCO was also performed to determine the breakeven selling price of biodiesel.

3. RESULTS AND DISCUSSION

This section compiles simulation results and also compares them with similar findings focusing on biodiesel production processes in the literature.

3.1. TECHNICAL RESULTS

3.1.1. Methanolysis Reaction. One of the most important factors which determines the feasibility of the supercritical process is the conversion of triglycerides (WCO) to methyl oleate (biodiesel) in the reactor.

As shown in Table 3, the molar conversion achieved in the reactor for both the plant capacities was 97.8%.

The entire downstream process for biodiesel purification is designed based on the specific amount of conversion or the reactor exit composition.

Table 6 Comparison of reaction conditions with acid catalyzed, alkali catalyzed and conventional supercritical biodiesel production processes

	Supercritical process with co-solvent (this study)	Homogenous Alkali catalyzed process [29]	Acid catalyzed process [15]	Conventional Supercritical process [29]
Methanol to Oil molar ratio	24:1	6:1	50:1	42:1
Reaction time, mins	8.35	108	240	2-6.7
Temperature, º C	280	60	80	300
Pressure, bar	128	4	4	200
Molar Conversion %	97.8	95	97	97

The higher the purity of methyl oleate (or more precisely, the conversion to methyl oleate) fewer will be the number of downstream steps required for purification which will result in lower costs.

For instance, a simple sensitivity analysis for 10,600 ton capacity plant revealed that increasing the reactor conversion to 98.7% (increase by 1%) lowered the required number of distillation column (Distil2) stages from 15 to 9 for the same distillate concentration.

This translates into lower capital costs for the distillation tower.

Table 6 compares the reaction conditions of this supercritical process (with a co-solvent) to other biodiesel production routes, such as, homogenous alkali catalyzed process, acid catalyzed process and conventional supercritical process.

Comparing with other routes, the supercritical process with a co-solvent operates with a lower methanol to oil ratio, which results in a lower overall reactor feed rate.

The comparison also reveals that the residence time of reactants in the reactor is lower for supercritical processes.

This can be attributed to higher temperature conditions in the supercritical reactor which catalyzes the forward reaction for transesterification.

However, despite the differences in reaction conditions, the final molar conversion in the case of the supercritical route does not differ significantly from other pathways.

This suggests that even though carrying out the transesterification reaction under supercritical conditions may influence the transesterification reaction rate, it might not affect the final conversion.

Table 7 shows the comparison of energy classified by process sections for a 10,600 ton/yr biodiesel production plant.

Table 7 Comparison of energy consumption by process section for a 10,600 ton/yr biodiesel production plant

Process section	Supercritical process with co-solvent (this study)	Homogenous Alkali catalyzed process [29]	Conventional Supercritical process [29]
Feed preheater (kW)	534	30	1201
Reactor (kW)	0	0	0
Methanol recovery (kW)	202	167	1662
Methyl Oleate purification (kW)	536	679	553
Glycerol purification (kW)	0	492	19
Heat recovery (kW)	320	-	876
Net thermal power required (kW)	952	1368	2559
Net electrical power required (kW)	53	-	25

The reactor energy consumption is shown to be zero since an adiabatic reactor was employed in this study. The major portion of the heating duty is expended in preheating the feed to the required supercritical conditions. Specifically, for a 10,600

ton/yr biodiesel production plant, approximately 56% of the plant's total heating duty was spent to preheat the reactor feed, as illustrated in Table 7.

However, for the same plant capacity, the alkali catalyzed process expends only 2.2% of the plant's total heating energy to preheat the reactor feed as it operates at low temperature and pressure conditions (60^0C and 4 bar) as compared to supercritical conditions. The thermal energy expenditure for reactor feed heating in the supercritical process with a co-solvent is 44% less than that required for a conventional supercritical process (see Table 7). This is mainly because the supercritical process with a co-solvent operates with a lower methanol to oil ratio of 24:1 as compared to a conventional supercritical process which operates at a ratio of 42:1.

3.1.2. Methanol Separation. Methanol recovery for the supercritical process under study was performed in two steps as shown in the flowsheet (Figure 2). In the first step, a flash drum operating at a pressure of 5 bar and 212^0C removed 95% of the methanol present in the product stream exiting the reactor, while in the second step, a distillation column operating at atmospheric pressure removed the remaining quantity of methanol so as to keep the methanol mass fraction at 0.3% in the bottom stream (S11).

Table 8 Comparison of different biodiesel production pathways with respect to separation process sections for a 10,600 ton/yr production capacity

Separation process section		Supercritical process with co-solvent (this study)	Homogenous Alkali catalyzed process [29]	Conventional Supercritical process [29]	Alkali catalyzed process [24]

Table 8 Comparison of different biodiesel production pathways with respect to separation process sections for a 10,600 ton/yr production capacity (cont.)

Methanol recovery distillation column	**Temperature – Condenser/Reboiler (^{0} C)**	60/320	29/5	28/101	28/122
	Pressure - Condenser/Reboiler (bar)	1/1	0.02/0.03	0.02/0.03	0.02/0.03
	Number of Stages	2	5	4	NA
	Reboiler duty (MW)	0.18	0.16	1.56	0.5
	Condenser duty (MW)	0.07	0.10	1.72	0.4
	Diameter (m)	0.46	0.6	1	0.6
Methyl oleate purification distillation column	**Temperature – Condenser/Reboiler (^{0} C)**	148/197	172/311	220/299	194/415
	Pressure - Condenser/Reboiler (bar)	0.01/0.01	1/2	1/2	1/2
	Number of Stages	15	5	5	NA
	Reboiler duty (MW)	0.54	0.64	0.52	1.6
	Condenser duty (MW)	0.42	0.52	0.33	1.3
	Diameter (m)	2.74	1.1	1	1.2

Table 8 Comparison of different biodiesel production pathways with respect to separation process sections for a 10,600 ton/yr production capacity (cont.)

Glycerol recovery distillation column	**Temperature – Condenser/Reb oiler (^{0} C)**	NR	43/244	15/177	NA
	Pressure - Condenser/Reb oiler (bar)	NR	1/2	1/2	NA
	Number of Stages	NR	4	5	NA
	Reboiler duty (MW)	NR	0.46	0.02	NA
	Condenser duty (MW)	NR	0.46	0.01	NA
	Diameter (m)	NR	0.3	0.3	NA

Table 8 depicts the results for methanol separation and compares them with the

different studies found in the literature for the same biodiesel production capacity (10,600

ton/yr). The reboiler heating duty and condenser cooling duty of a methanol recovery

distillation column (in the case of conventional supercritical process) is correspondingly

8 times and 25 times as that of supercritical process with a co-solvent. These higher

values are expected since the conventional supercritical process employs a higher

methanol to oil ratio, which translates into a higher methanol feed rate to the distillation

column, which inevitably results in higher reboiler and condenser duties. Apart from the

energy usage, the results regarding the distillation column for methanol recovery are

similar to those for the conventional supercritical biodiesel production process. Also

shown in Table 7, the thermal energy expenditure for methanol recovery section constitutes about 16% of the total heating duty of the plant, as opposed to 48% which is the case for conventional supercritical biodiesel production process of similar plant capacity. The results also show that the number of stages required to recover methanol in a small capacity plant are the same as that required for larger plant (128,000 ton/yr).

3.1.3. Glycerol Purification. A decanter operating at atmospheric temperature and pressure was sufficient enough to obtain pharmaceutical grade glycerol in the case of the small capacity plant. However, an additional flash drum - Flashdr2 (one theoretical stage) was necessary for the scaled up plant capacity (128,000 ton/yr), as shown in Figure 2.

Before introducing the feed to flash drum (Flashdr2) it is slightly preheated in H-9 which is necessary to ensure that the feed has a sufficient amount of enthalpy that could be used by methanol for evaporation. The H-9 heat exchanger in the glycerol section consumes only a fraction of the total thermal energy in the plant (0.64%) as depicted in Table 7.

The glycerol purity obtained was 99.7% and adhered to pharmaceutical grade requirements. Comparing these results of the 10,600 ton plant capacity with published studies in the literature, both the conventional supercritical biodiesel production route and the homogenous alkali catalysis route necessitate the inclusion of a distillation column for glycerol purification (shown in Table 8) while the supercritical process with co-solvent does not.

As depicted in Table 7, the glycerol purification section consumes 36% of the total thermal energy use in a homogenous alkali catalyzed process while in both of the

supercritical biodiesel production pathways (with and without a co-solvent) it has a negligible thermal energy footprint.

3.1.4. Methyl Oleate Purification. As shown in flowsheet (Figures 1 and 2), the distillation column, Distil2 was able to remove approximately 87% of triolein from its input stream to achieve a 99.4% pure methyl oleate which adhered to the US (ASTM D6751) and European (EN14214) biodiesel quality standards.

As mentioned previously, the main objective of this column was to separate triolein from methyl oleate. Therefore, lowering the concentration of triolein in the distillation feed means fewer number of stages will be required for distillation. According to the simulation results, the number of theoretical stages required for biodiesel purification in a distillation column for a larger capacity plant (128,000 ton/yr) was 20 while that for a smaller plant capacity (10,600 ton/yr) was 15. Even though the thermodynamic fluid package used was the same, the increase in the number of stages was due to the slight increase in the methanol molar composition in feed stream, from 0.21% to 1.64%.

Results in Table 7 also indicate that 42% of total thermal energy used in the plant was spent on purifying methyl oleate. Certain studies available in the literature report that the energy spent in the biodiesel purification distillation column for a 10,600 ton per year production capacity was in the range of 200-250 kW which is approximately half of the energy that is estimated in this work [18,26]. This is mainly because the researchers assumed an almost complete conversion of triglyceride to biodiesel (>99.5%). This results in lower concentration of triglycerides in the distillation column feed by

approximately 3.5 times compared to feed concentration of the corresponding distillation column (Distil2) in this work.

3.1.5. Heat Integration and Energy Consumption. Even though the philosophy used to design a heat integration network for a 10,600 ton production capacity plant was same as that used for a 128,000 ton capacity plant, the final outcome differed considerably.

For instance, 8 heat exchanger units (H-1 to H-8) were deployed in the smaller plant while 12 heat exchanger units (H-1 to H-12) were installed in the larger plant, as illustrated in Figures 1 and 2 respectively. Table 9 below shows the thermal energy consumption for every heat exchanger in both plants.

For both plant capacities, the detailed design of heat integration network revealed that the maximum thermal energy that could be recovered from the process was approximately 27% of the total thermal energy required in the entire process. The obtained result was similar to studies available in the literature which stated that 25% of the total thermal energy in a supercritical biodiesel production plant was captured through heat integration [27].

In Figure 3 the numbers at the top of the illustrative bars denote the absolute value of energy consumption for that respective plant section, while the numbers in the parenthesis denote the percentage share of the plant's net heating duty. The maximum thermal energy was consumed in the feed preheating section and methyl oleate purification section, whereas minimum energy was expended in the glycerol purification section.

Table 9 Thermal power consumption for supercritical biodiesel production process

ID	Thermal power consumption (kW)		Recovered thermal power (kW)	
	10,600 ton/yr	128,000 ton/yr	10,600 ton/yr	128,000 ton/yr
Heat Exchangers				
H-1	-	-	55	1900
H-2	-	-	65	1300
H-3	-	3303	200	-
H-4	214	503	-	-
H-5	17	-	-	700
H-6	-110	-697	-	-
H-7	-39	-	-	300
H-8	-282	-178	-	-
H-9	-	103	-	-
H-10	-	-137	-	-
H-11	-	-8	-	-
H-12	-	-2156	-	-
Distil1 condenser	-70	-420	-	-
Distil1 reboiler	185	740	-	-
Distil2 condenser	-423	-7079	-	-
Distil2 reboiler	536	6676	-	-

These results were expected because raising reactants to supercritical conditions and purifying methyl oleate in a distillation column would consume maximum energy, as compared to purification of glycerol which is carried out in a simple decanter operating at atmospheric temperature and pressure.
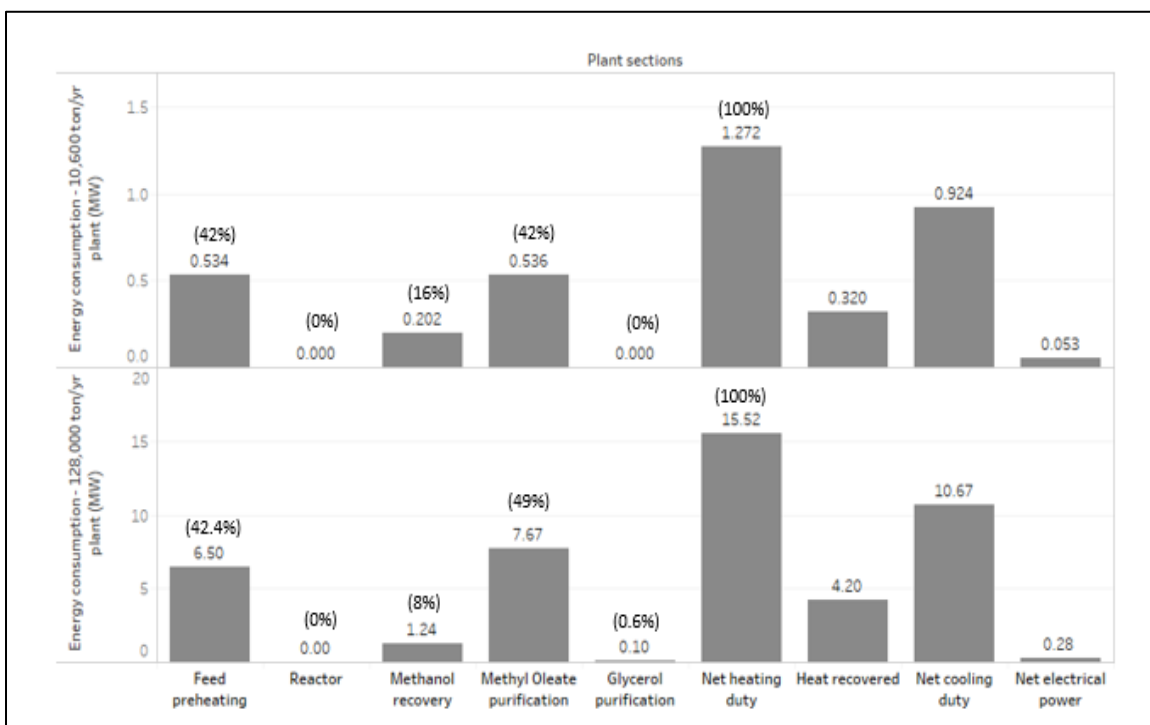
Figure 3 Section wise energy consumption of plants of annual capacity - 10,600 ton and 128,000 ton

3.2. ECONOMIC RESULTS

This section contains the results of the detailed economic analysis of the supercritical biodiesel production process for plants of two different capacities (10,600 ton/yr and 128,000 ton/yr) located in the Midwest region of the US. An estimation of direct, indirect, fixed capital, utility, working, depreciation, utility, labor, and

manufacturing costs was made in this economic assessment. A cash flow analysis was also performed to determine the economic feasibility of the plants. Furthermore, a sensitivity analysis was conducted with respect to the purchase price of WCO in order to determine the breakeven selling price of biodiesel.

3.2.1. Main Characteristics of Equipments and their Costs. Based on technical design, the sizing and cost estimations for all the units were performed using Aspen Plus v10.

For both plant capacities (10,600 ton/yr and 128,000 ton/yr), the main design characteristics and purchase equipment costs (PEC) for all the units shown in the flowsheet (Figures 1 and 2) are displayed in Table 10.

Table 10 Main characteristics of equipments and their purchase equipment costs

Equipment Name	10,600 ton/year capacity		128,000 ton/year capacity	
	Design Characteristics	Purchase Equipment Cost ($)	Design Characteristics	Purchase Equipment Cost ($)
Centrifugal Pumps				
P1	P_{in}:1 bar, P_{out}:128 bar, 48 kW$_e$	51,002	P_{in}:1 bar, P_{out}:128 bar, 159 kW$_e$	425,300
P2	P_{in}:1 bar, P_{out}:10 bar, 0.07 kW$_e$	49,959	P_{in}: 1 bar, P_{out}:10 bar,0.55 kW$_e$	15,600
P3	P_{in}:5 bar, P_{out}:10 bar, 0.83 kW$_e$	48,082	P_{in}: 5 bar, P_{out}:10 bar, 5.37 kW$_e$	6,000
P4	P_{in}:0.01 bar, P_{out}:10 bar, 0.2 kW$_e$	50,794	P_{in}:0.01 bar, P_{out}:10 bar, 1.25 kW$_e$	15,700
P5	P_{in}:0.01 bar, P_{out}:10 bar, 1.5 kW$_e$	4,798	P_{in}:0.01 bar, P_{out}:10 bar, 10 kW$_e$	5,800
P6	-	-	P_{in}: bar, P_{out}:10 bar, 0.02 kW$_e$	15,800
P7	-	-	P_{in}:0.01 bar, P_{out}:1 bar, 0.01 kW$_e$	4,100

Table 10 Main characteristics of equipments and their purchase equipment costs (cont.)

Distil1 reflux pump	P_{in}:1 bar, P_{out}:2 bar, 0.75 kW$_e$	4,798	P_{in}: 1 bar, P_{out}:2 bar, 5 kW$_e$	4,798
Distil2 reflux pump	P_{in}:0.01 bar, P_{out}:1 bar, 0.75 kW$_e$	5,528	P_{in}: 0.01 bar, P_{out}: 1 bar, 5 kW$_e$	4,798
Total Pump costs ($)		214,961		497,896
Shell and Tube Heat Exchangers, Material of construction: Carbon Steel.				
H-1	Area:2.58 m^2, UA=1.71 kW/K	10,743	Area:110 m^2, UA=55 kW/K	80,000
H-2	Area:0.38 m^2, UA=1.68 kW/K	8,344	Area:72 m^2, UA=32 kW/K	66,200
H-3	Area:3.81 m^2, UA=4.37 kW/K	14,080	Area:84 m^2, UA= 52.23 kW/K	80,500
H-4	Area:1.38 m^2, UA=4.9 kW/K	9,804	Area:26 m^2, UA=18.48 kW/K	29,500
H-5	Area:3.07 m^2, UA=1 kW/K	9,178	Area:146 m^2, UA=32.6 kW/K	33,600
H-6	Area:6.50 m^2, UA=2.53 kW/K	10,534	Area:70 m^2, UA=27 kW/K	22,200
H-7	Area:17.27 m^2, UA=1.65 kW/K	24,302	Area:21 m^2, UA=14.62 kW/K	12,900
H-8	Area:4 m^2, UA=3.83 kW/K	10,221	Area:83 m^2, UA=14.51 kW/K	25,300
H-9	-	-	Area:1.73 m^2, UA= 1.39 kW/K	8,700
H-10	-	-	Area:7.45 m^2, UA=3.65 kW/K	10,200
H-11	-	-	Area:0.38 m^2, UA=0.215 kW/K	8,000
H-12	-	-	Area:38 m^2, UA=30.8 kW/K	16,400
Distil1 condenser	Area:1 m^2, UA=0.82 kW/K	8,865	Area:18 m^2, UA=13 kW/K	13,246
Distil1 reboiler	Area:5 m^2, UA=3.47 kW/K	21,903	Area:14.7 m^2, UA=9.69 kW/K	21,277
Distil2 condenser	Area:4.17 m^2, UA=3.04 kW/K	10,326	Area:104 m^2, UA=72 kW/K	28,682
Distil2 reboiler	Area:32.65 m^2, UA=23 kW/K	23,989	Area:454 m^2, UA=318 kW/K	152,590
Total costs for Heat Exchangers ($)		162,289		609,925
Distillation Columns, Material Of Construction – Carbon Steel, Sieve Trays,				
Distil1	D:0.45m, H:4.87m, Trays:2	15,749	D:1 m, H:4.87 m, Trays:2	39,100
Distil2	D:2.17 m, H:4.87m, Trays:15	236,237	D:10 m, H:21 m, Trays:20	1,648,200
Tanks, Drums and Vessels, Material Of Construction – Carbon Steel.				
Flashdr1	V:2.4 m^3 , D:0.91m, H=3.6m	52,358	V:6 m^3, D:1.37m, H=4.11m	94,300

Table 10 Main characteristics of equipments and their purchase equipment costs (cont.)

Flashdr2	-	-	V:2.4 m^3, D:0.91m, H=3.6m	16,100
Distil1 condenser accumulator	V:1.8 m^3 , D:0.91m, H=2.74 m	16,479	V:1.8 m^3, D:0.91m, H=2.7m	15,800
Distil2 condenser accumulator	V:1.8 m^3, D:0.91m, H=2.74 m	16,479	V:6.3 m^3, D:1.37m, H=4.26m	25,800
Decanter	V:2.4 m^3, D:0.91m, H=3.6m	16,792	V:4.45 m^3, D:1.22m, H=3.81m	20,300
Total costs for Tanks, Drums and Vessels		102,108		172,300
Plug flow reactors, Material of construction – Carbon Steel				
Plug flow reactor	V:0.863 m^3, D: 0.1m , L:55 m, 2 tubes	90,063	V:9.89 m^3, D: 0.1m , L:60 m, 21 tubes	466,284
Utility and other facilities				
Forced draft cooling tower	Cooling capacity- 53 ton/hr	22,598	Cooling capacity- 611 ton/hr	312,955
Water tube boiler	Steam generation Capacity- 2.25 ton/hr	53,032	Steam generation Capacity- 24 ton/hr	522,244
Plate and frame filter press	Area: 30 m^2	43,953	Area: 358 m^2	210,586
Total utility and other facilities cost ($)		119,583		1,045,785
Total Purchase Equipment cost ($)		940,632		4,768,233

Cost estimation of pumps is an important step in determining the capital cost of a plant and its value depends on type of pump selected. Owing to its low capital and maintenance costs centrifugal pumps were chosen as the type of equipment for pumps. The selected material of construction for the pumps was Carbon Steel. Along with purchase equipment costs, the information regarding the incoming fluid pressure, discharge pressure and the power consumption for all the pumps in the plants is shown in Table 10. For the case of the small plant (10,600 ton/yr) the pumps together accounted

for 23% of total PEC while for the larger plant (128,000 ton/yr) they accounted for 10% of the total PEC. Raw material feed pump P1 is the most capital intensive of all the pumps within the plant as its function is to increase the feed stream pressure from 1 bar to 128 bar.

Countercurrent shell and tube heat exchangers were chosen for heat exchangers (H-1 to H-12) and distillation condensers owing to their high thermal efficiency and their ability to handle diverse classes of fluids. Kettle type reboilers were selected for distillation column reboilers (DC1 reboiler and DC2 reboiler). The shell and tube heat exchangers and reboilers were sized by Aspen Plus according to Tubular Exchangers Manufacturers Association's (TEMA) guidelines. The results of sizing and economic evaluation for heat exchangers in the form of heat transfer area and overall heat transfer coefficient (UA) are shown in Table 10. The cost of heat exchangers amounted to 17% and 13% of the total PEC for 10,000 ton and 128,000 ton plant capacity respectively.

In terms of PECs, distillation columns have the largest share by type of equipments (Table 10) together comprising of 27% of total PEC for small plant and 35% for the large plant. Distillation columns were sized assuming that they were comprised of sieve trays with 0.6m of tray spacing. Based on the calculated diameter and height of the column, the purchase and installation costs were estimated assuming that the material of construction employed is carbon steel. Approximately, more than 95% of the PEC cost for distillation columns is attributed to methyl oleate distillation tower (Distil2). This is expected as the number of trays in this column are approximately 7 times greater than what is present in the methanol recovery distillation column (Distil2). In addition, compared to the methanol recovery column, which operates under atmospheric pressure,

the methyl oleate distillation column operates under vacuum which further increases its fabrication costs.

Based on their function, tanks, drums and vessels were first classified into two types, namely, horizontal vessels and vertical vessels. Flash drums and decanters were classified as vertical vessels while condenser accumulators were categorized as horizontal vessels. After this, they were sized according to TEMA guidelines using the sizing tool in Aspen Plus. The tanks, drums and vessels had a minor share of capital costs as they only comprised of 11% and 4% of the total PECs for the case of 10,600 ton and 128,000 ton capacity respectively.

The cost of the reactor was calculated by using Aspen Plus sizing tool and also by referring to supercritical reactor design studies which focus on biodiesel production [18,21]. The average of both values was chosen in this analysis. This procedure was adopted to get the best estimate of the reactor cost, which is one of the most critical pieces of equipments in this process. The reactor cost is approximately 10% of the total PECs for both of the plant capacities under study.

The accurate capital cost estimation of utilities is of paramount importance in the economic assessment of supercritical process as it can be a decisive factor for commercial implementation. Despite its pivotal role in determining economic feasibility, some of the prior studies focusing on supercritical biodiesel production processes did not perform a comprehensive calculation regarding capital cost of boilers and cooling towers. For instance, instead of calculating separately the boiler and cooling tower costs, West et al. assumed the capital cost of utilities cost as 30% of direct costs [15]. A similar assumption was made by Ortiz et al. in which the authors calculated the capital cost of

cooling tower as a simple percentage of direct costs [21]. However, in this study based on quantity of cooling water and steam required, capital costs for forced draft cooling tower and water tube boiler were determined by following two different methodologies [30,41]. An average value of those capital costs was chosen to get the best possible estimate for both plant capacities. The boiler and cooling tower costs together were determined to be approximately 10% and 17% of the total PECs for 10,600 ton and 128,000 ton plant capacities respectively. In addition to cooling towers and boilers, costs were also estimated for procuring a plate and frame filter press for filtering WCO [41]. Although the plate and frame filter press is not shown in the process flowsheet, it is needed for filtering WCO as the oil feed might contain certain solid impurities when procured from the vendor. The filter press costs comprised of small portion of the total PEC and were calculated to be 5% for both plant capacities.
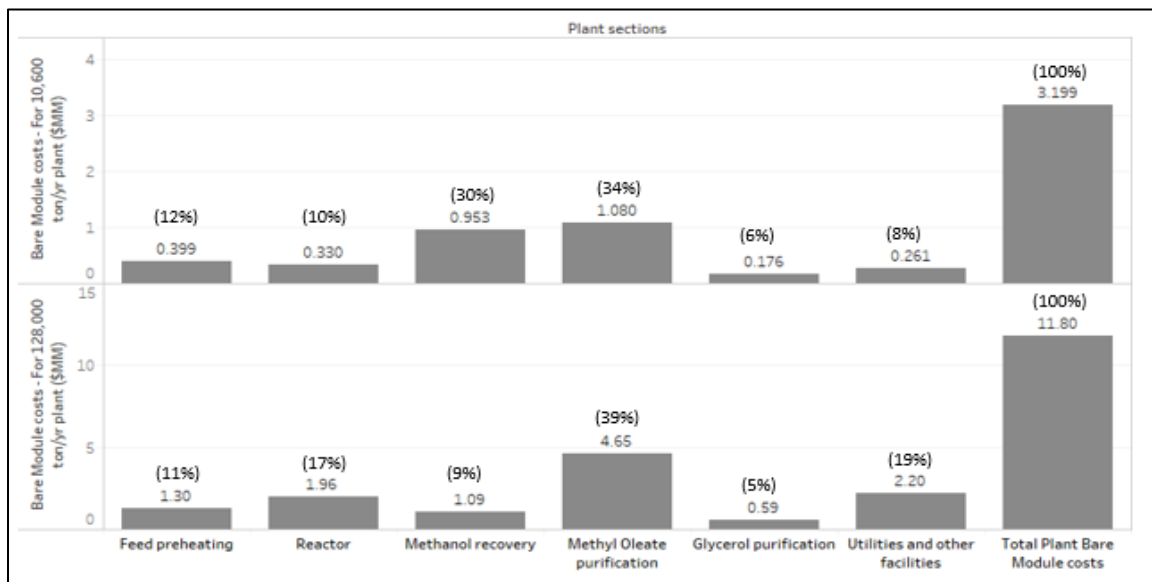
Figure 4 Plant section wise breakdown of bare module costs (installed costs) for 10,600 ton plant capacity and 128,000 ton plant capacity

Figure 4 illustrates the breakdown per section for bare module costs (Installed costs) for both plant capacities. In Figure 4 the numbers at the top of the illustrative bars denote the absolute value of bare module costs while the numbers in the parenthesis denote the percentage of total plant bare module costs. For both plant capacities, Figure 4 shows that the costs for methyl oleate purification section accounts for over one third of the entire bare module costs of the plant. As stated previously, this is due to the high capital costs attributed of the distillation column (Distil2). Figure 4 also shows that as the capacity of the biodiesel plant increases, the share of methanol recovery section as a portion of total plant costs decreases by a factor of three while the share of 'Utilities and other facilities' costs doubles. Furthermore, the share of reactor costs as a percentage of total plant costs also increases by a factor of 1.7. All of the other plant section costs as a share of total plant costs remain approximately the same as the capacity of the plant increases.
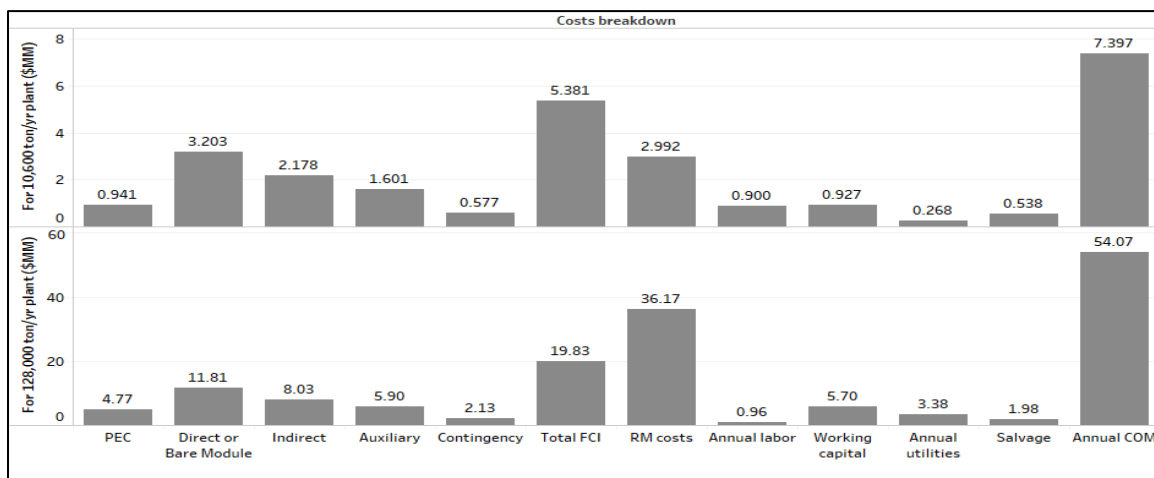
Figure 5 Breakdown of costs for 10,600 ton/yr capacity plant and 128,000 ton/yr capacity plant

After the calculation of PEC, the direct, indirect costs, fixed capital investment (FCI), and working capital along with annual costs for utility, raw material (RM), labor and manufacturing were calculated and are illustrated in Figure 5 for both plant capacities. The results reveal that 40% and 66% of the annual cost of manufacturing (COM) is attributed to raw material expenditure while utilities constitute only 4% and 6% of annual COM for 10,600 ton and 128,000 ton plant capacities respectively.

This suggests that annual COM is extremely sensitive to variation in WCO and methanol prices but is relatively insensitive to variation in natural gas price ($/GJ) or electricity prices ($/kWh).

3.2.2. Cash Flow Analysis. A cash flow analysis was conducted for both plant capacities with respect to raw material, product and utility costs specified in Table 5.
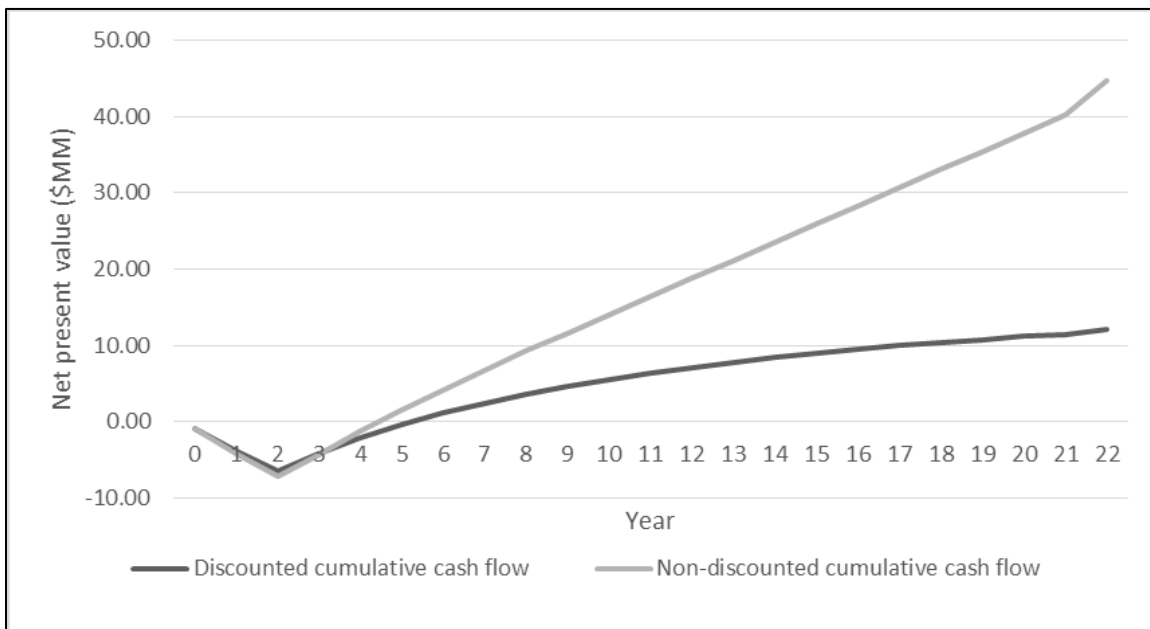
Figure 6 Cash flow analysis of a supercritical biodiesel production plant of annual capacity of 10,600 ton

Figure 6 and Figure 7 illustrate the variation of discounted and non-discounted cash flow over the lifetime of the plant of annual biodiesel production capacities 10,600 ton and 128,000 ton situated in the Midwest region of the US. As opposed to non-discounted cash flow, the discounted cash flow incorporates the effect of time on the value of money.
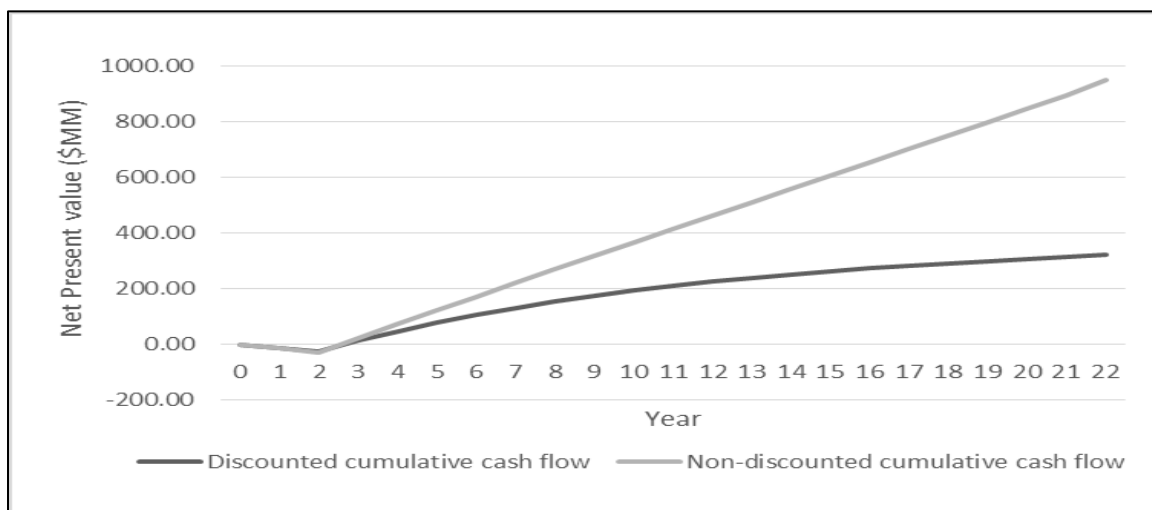
Figure 7 Cash flow analysis of a supercritical biodiesel production plant of annual capacity of 128,000 ton

At the start of the project (year zero), the cash flow is negative due to investment costs incurred from land purchases. Subsequently, over the next two years the cash flow plunges further in the negative direction because the entire FCI required to construct the plant is spent in two installments over that period. In the first installment 60% of FCI is spent at the end of year one while the rest is spent at the end of the second year. The plant becomes operational at the beginning of the third year. At the end of the third year, due to manufacturing costs (COM), the cash flow curve further tends to drift in the negative

direction. However, the revenue generated due to the sale of biodiesel and glycerol pushes the curve in the positive direction. The net outcome of both these effects is that the cash flow curve drifts in the positive direction because the annual revenue of a single year exceeds the COM. In the subsequent years, due to this positive effect the net trend of non-discounted and discounted cash flow is in the positive direction, as is evident in Figure 6 and Figure 7.

The entire FCI is depreciated over a period of five years using MACRS method as stated earlier. For tax purposes, the depreciation of plant infrastructure (or FCI) is assumed to occur immediately after the plant becomes operational, that is, from the start of the third year. This is done to reduce taxes and conserve more cash in the earlier stages of the project. According to the discounted cash flow analysis results, the values for net present value (NPV), payback period and the rate of return on investment (ROI) for 10,600 ton plant capacity are $12 million, 2.3 years and 30% respectively, while for 128,000 ton capacity the corresponding values are $321 million, 0.5 years and 108%. These results suggest that the project becomes more profitable as plant production capacity increases, thereby exhibiting the economies of scale effect. Furthermore, the breakeven selling price of biodiesel for 10,600 ton/yr plant and 128,000 ton/yr plant was calculated to be $2.47 and $1.33 per gallon respectively.

A comparison of these economic results for produced from WCO is made with published reports available in the literature and is shown in Table 11.

A study of supercritical biodiesel production process reported that the NPV and payback period for a 125,000 ton/yr plant was $11 million and 5 years respectively while for 8,000 ton/yr plant was $3 million and 5 years respectively [18]. However, the authors

of that study assumed a discount factor of 20% and a project life of 17 years which differ

considerably from the values used in this study which are 10% and a project life of 20

years.

West et al. also deemed the biodiesel production via alkali catalyzed, acid

catalyzed and supercritical processes to be economically unfeasible with a negative rate

of return on investment while also reporting that the heterogeneous acid catalyzed

process to be the only profitable pathway with a rate of return on investment of 58% [15].

All these studies imply that the economic feasibility of a supercritical biodiesel

production not only depends on technical design of the process but also on economic

assumptions made during the analysis.

Table 11 Comparison of economic analysis results for biodiesel produced from WCO

Process type	Supercritical process (this study)		Alkali catalyzed process [44]	Heterogeneous acid catalyzed [44]	Supercritical process [18]		Supercritical process [21]
Plant capacity (ton/yr)	10,600	128,000	8,000	8,000	8,000	125,000	10,000
Rate of Return on investment (%)	30%	108%	-52%	-16%	20%	20%	10
Breakeven selling price of biodiesel ($/gallon)	2.47	1.33	2.9	2.3	1.35	1.15	1.93
Payback period (years)	2.3	0.5	-	-	5	5	15

3.2.3. Sensitivity Analysis. As shown earlier, the raw material costs (WCO and methanol) could comprise up to 66% of the costs of manufacturing (COM). The raw material cost calculations reveal that the cost of WCO constitutes approximately 80% of the total costs. According to one study, the WCO costs could constitute 92% of the total costs of raw material [21].

A different study also reported that the costs attributed to purchase of oil were 90% of the total raw material costs required for supercritical biodiesel production process [15]. Therefore, the ability of the biodiesel production plant to generate profits and thereby become economically sustainable is strongly dependent on the purchase price of WCO. Any fluctuation in the market price of WCO will significantly impact the earnings. To quantify this risk, a sensitivity analysis was performed to study the effect of WCO purchase price on the breakeven selling price of biodiesel. Breakeven price of biodiesel is defined as the selling price at which the NPV of the plant at the end of project life (20 years) just rises above zero [28].

From its base price of $0.227 per kg, the purchase price of WCO varied between -50% and 50%. The breakeven selling price of biodiesel ($/gallon) is recorded for both plant capacities (10,600 ton/yr and 128,000 ton/yr) and is shown in Figure 8. For a fixed plant capacity, a linear dependence between breakeven selling price of biodiesel and purchase price of WCO was observed. For every 10% increase in WCO price, the breakeven biodiesel price increased by 7% and 4% for 128,000 ton plant and 10,600 ton plant respectively. This trend suggests that as compared to a small biodiesel plant, the breakeven selling price of biodiesel is more sensitive to fluctuation in WCO purchase price for a larger capacity plant. Additionally, the breakeven selling price of biodiesel for

a 128,000 ton/yr plant is approximately half of the breakeven value of a 10,600 ton/yr

plant demonstrating the economies of scale effect. The breakeven selling price of

biodiesel is similar to the values reported in published literature as shown in Table 11.
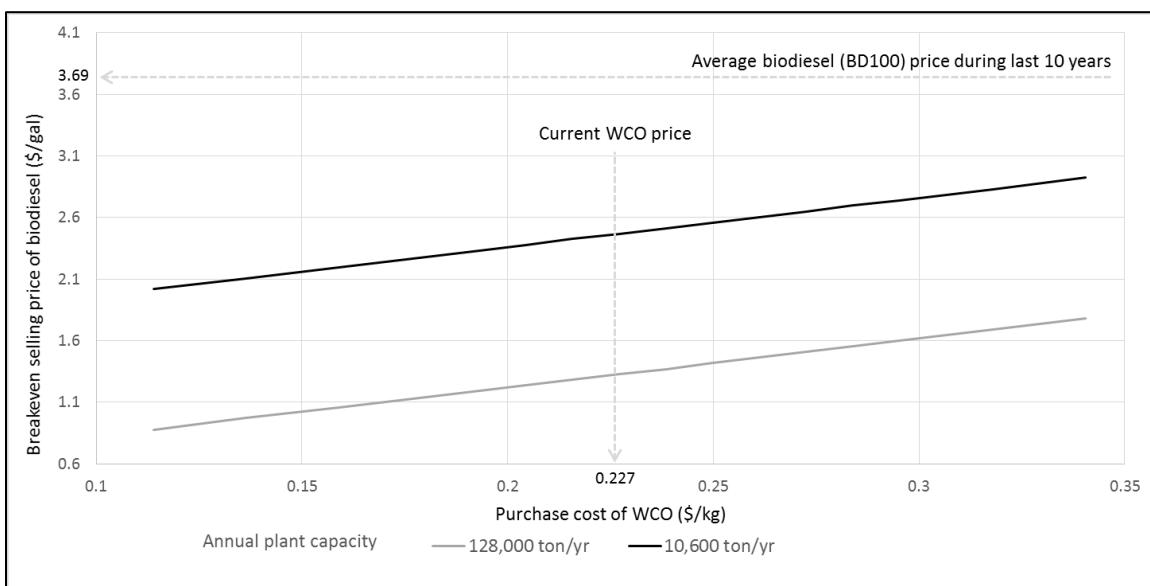
Figure 8 Breakeven selling price of biodiesel as a function of WCO purchase price

As depicted in Figure 8, a notable observation regarding the breakeven price of

biodiesel is that it remains well below the last ten years' average biodiesel price

exhibiting the ability of the supercritical process to thrive when the selling price of

biodiesel fluctuates. At the current prices of WCO ($0.227 per kg), the breakeven selling

price for biodiesel is 64% and 32% less than the last ten years' average biodiesel price.

A previous study has techno-economically evaluated a small scale supercritical

biodiesel production plant and then expanded it to a larger scale plant by adjusting the

capacity of all equipment to a larger scale plant [18]. The main assumption in adopting

this technique is that the larger plant will possess the same number of units arranged in the same sequential manner as that for a small plant.

This assumption is not accurate even though the reactor conversion was the same in both plant capacities. For instance, as shown in earlier sections of this work, the technical design of a larger plant (128,000 ton/yr) contains four more heat exchangers, two more pumps and one more flash drum than a smaller biodiesel plant (10,600 ton/yr). Furthermore, the larger plant (128,000 ton/yr) requires five more stages in methyl oleate distillation column than the smaller plant (10,600 ton/yr). This assumption would not accurately estimate the equipment costs and utilities cost. Therefore, to accurately capture the technical requirements of a small scale and a large scale biodiesel plant and study its impact on economics, two independent techno-economic evaluations were performed which established the viability of the process.

4. CONCLUSIONS

A supercritical biodiesel production process using supercritical methanol in the presence of propane as a co-solvent has been technically designed using Aspen Plus software. Appropriate thermodynamic fluid packages such as SRK and UNIQUAC have been utilized. The presence of the co-solvent propane reduced the temperature and pressure conditions required for transesterification reaction. The reaction was carried out at 280 ^{0}C and 128 bar with a residence time of 8.35 minutes with a realistic oil to biodiesel molar conversion rate of 97.8%. The biodiesel obtained was then purified with the help of flash drums and distillation columns to 99.4%, which adhered to US (ASTM D6751) and European (EN14214) fuel quality standards. As a by-product, glycerol was also obtained with a pharmaceutical grade purity of 99.7%. A detailed integrated design

of heat exchanger networks was performed to optimize energy consumption of the process. The supercritical biodiesel production process was technically designed and analyzed for a small production capacity plant (10,600 ton/yr) as well as for a large capacity plant (128,000 ton/yr) in order to accurately capture the effect of economies of scale.

Based on the technical results, a detailed economic assessment of the supercritical process was carried out. A breakdown of capital costs and energy costs was also presented to identify the financial hotspots of the process. A cash flow analysis was also conducted to determine the economic feasibility which revealed the supercritical process as a profitable venture with a payback period of 2.3 years and 0.5 years for 10,600 ton and 128,000 ton plant capacity respectively. The breakeven cost was also determined to be $2.47 and $1.33 for a gallon of diesel respectively deeming the process to be profitable venture at the current biodiesel price of $3.38 per gallon. These financial metrics were compared to other supercritical biodiesel production studies available in the literature and also with alkali and acid catalyzed pathways. Realizing the strong influence of the WCO purchase price on the breakeven selling price of biodiesel, a sensitivity analysis was carried out to assess its impact. This analysis proved the ability of the supercritical biodiesel production process to thrive even when the purchase price of WCO increased or decreased by 50%.

The technical and economic assessment results of this work exhibit the techno-economic sustainability of the supercritical biodiesel production process. Future work must be carried out to assess the carbon footprint of this process using commercial environmental life cycle assessment (LCA) software such as Gabi, Simapro or GREET.

An environmental LCA study will supplement this techno-economic evaluation which will enable researchers to make an informed decision about the overall sustainability of the supercritical biodiesel production process. Furthermore, pilot plant investigations must be conducted before implementation of this process can be made on a commercial scale.

ACKNOWLEDGEMENT

REFERENCES

1. Sheehan J., Camobreco V, Duffield J, Graboski M, Shapouri M. Life cycle inventory of biodiesel and petroleum diesel for use in an urban bus. US DOE report; May 1998.

2. Can O. Combustion characteristics, performance and exhaust emissions of a diesel engine fueled with a waste cooking oil biodiesel mixture. Energy Convers Manag 2014 ; 87:676-86 https://doi.org/10.1016/j.enconman.2014.07.066.

3. L.C. Meher, D. Vidya Sagar, S.N. Naik. Technical aspects of biodiesel production by transesterification a review, Renew. Sust. Energy Rev. 3 2004; 1–21. https://doi.org/10.1016/j.rser.2004.09.002

4. F. Ma, Hanna M.A., Biodiesel production: a review, Bioresour Technol 1999; 70: 1–15. https://doi.org/10.1016/S0960-8524(99)00025-5

5. O. Farobie, Y Matsumura. State of the art biodiesel production under supercritical conditions. Prog in Energy and Combust Sc 2017; 63: 173-203. https://doi.org/10.1016/j.pecs.2017.08.001

6. D.G.B. Boocock, S.K. Konar, V. Mao, C. Lee, S. Buligan Fast formation of high-purity methyl esters from vegetable oils. J of the Amer Oil Chem Soc 1998; 75:1558-9331. https://doi.org/10.1007/s11746-998-0130-8

7. Saka S, Kusdiana D .Biodiesel fuel from rapeseed oil as prepared in supercritical methanol .Fuel 2001;80:225–31.doi:10.1016/S0016-2361(00)00083-1.

8. GlisicSB, SkalaDU.Phase transition at subcritical and supercritical conditions of triglycerides methanolysis . J Supercrit Fluids 2010; 54:71–80 .doi:10.1016/j.supflu.2010.03.005.

9. Deslandes N, Bellenger V, Jaffiol F, Verdu J. Solubility parameters of a polyester composite material. J Appl Polym Sci 1998; 69:2663–71. https://doi.org/10.1002/(SICI)1097-4628(19980926)69:13<2663::AID-APP17>3.0.CO;2-V

10. Ma F, Clements LD, Hanna MA. Biodiesel fuel from animal fat. Ancillary studies on transesterification of beef tallow. Ind Eng Chem Res 1998;37:3768–71. https://doi.org/10.1021/ie980162s

11. S. Ngamprasertsith, R. Sawangkeaw, Margarita Stoytcheva (Ed.),Transesterification in Supercritical Conditions Biodiesel—Feedstocks and Processing Technologies, In Tech Ed., 2011, pp. 247–268. https://doi.org/10.5772/26239

12. Imahara H, Xin J, SakaS. Effect of CO2/N2 addition to supercritical methanol on reactivities and fuel qualities in biodiesel production.Fuel 2009; 88:1329–32. https://doi.org/10.1016/j.fuel.2009.01.002.

13. Trentin CM,Lima AP,Alkimim IP,DaSilva C,DeCastilhos F, Mazutti MA.Continuous catalyst-free production of fatty acid ethyl esters from soybean oil in microtube reactor using supercritical carbondioxide as co-solvent. J Supercrit Fluids 2011;56:283–91. https://doi.org/ 10.1021/ie070310r

14. Muppaneni T,Reddy HK,Patil PD,Dailey P,Aday C,Deng S.Ethanolysis of cam-elina oil under supercritical condition with hexane as a co-solvent.Appl Energy 2012;94:84–8. https://doi.org/10.1016/j.apenergy.2012.01.023.

15. A.H. West, D. Posarac, N. Ellis, Assessment of four biodiesel production processes using HYSYS Plant, Bioresour. Technol. 2008; 99:6587–6601. https://doi.org/10.1016/j.biortech.2007.11.046

16. J.M. Marchetti, A.F. Errazu, Technoeconomic study of supercritical biodiesel production plant, Energy Convers. Manage. 2008; 49:2160–2164. https://doi.org/10.1016/j.enconman.2008.02.002

17. S. Morais, T. Mata, A. Martins, G. Pinto, C. Costa, Simulation and life cycle assessment of process design alternatives for biodiesel production from waste vegetable oils, J. Clean. Prod. 2010; 18:1251–1259. https://doi.org/10.1016/j.jclepro.2010.04.014

18. J.M.N. Kasteren, A.P. Nisworo, A process model to estimate the cost of industrial scale biodiesel production from waste cooking oil by supercriticaltransesterification, Resour. Conserv. Recycl. 2007; 50:442–458. https://doi.org/10.1016/j.resconrec.2006.07.005

19. S. Lee, D. Posarac, N. Ellis, Process simulation and economic analysis ofbiodiesel production processes using fresh and waste vegetable oil and supercritical methanol, Chem. Eng. Res. Des. 2011; 89:2626–2642. https://doi.org/10.1016/j.cherd.2011.05.011

20. https://ycharts.com/indicators/europe_natural_gas_price [Accessed 15 February 2018]

21. F.J.Z Ortiz, P. Santa-Ana, Techno-economic assessment of an energy self-sufficient process to produce biodiesel under supercritical conditions, J. of Supercritical Fluids 2017,128:349-358. https://doi.org/10.1016/j.supflu.2017.03.010

22. https://www.eia.gov/biofuels/biodiesel/production/ [Accessed 15 February 2018]

23. Cao W, Han H, Zhang J.Preparation of biodiesel from soybean oil using supercritical methanol and co-solvent.Fuel 2005; 84:347–51. https://doi.org/10.1016/j.fuel.2004.10.001.

24. Y. Zhang, M.A. Dube, D.D. McLean, M. Kates, Biodiesel production from waste cooking oil: 1. Process design and technology assessment, Bioresour. Technol. 2003; 89:1–16. https://doi.org/10.1016/S0960-8524(03)00040-3

25. F.J. Gutiérrez Ortiz, P. Ollero, A. Serrera, S. Galera, Optimization of power and hydrogen production from glycerol by supercritical water reforming, Chem.Eng. J. 2013; 218:309–318. https://doi.org/10.1016/j.cej.2012.12.035

26. V.F. Marulanda, Biodiesel production by supercritical methanol transesterification: process simulation and potential environmental impactassessment, J. Clean. Prod. 2012; 33:109–116. https://doi.org/10.1016/j.jclepro.2012.04.022

27. S. Glisic, D. Skala, The problems in design and detailed analyses of energy consumption for biodiesel synthesis at supercritical conditions, J. Supercrit.Fluids 2009; 49:293–301. https://doi.org/10.1016/j.supflu.2008.12.011

28. R. Turton, R.C. Bailie, W.B. Whiting, J.A. Shaeiwitz, Analysis, Synthesis and Design of Chemical Processes, 3rd ed., Prentice Hall, 2017

29. S. Glisic, D. Skala, The problems in design and detailed analyses of energyconsumption for biodiesel synthesis at supercritical conditions, J. Supercrit.Fluids 2009; 49:293–301. https://doi.org/10.1016/j.supflu.2008.12.011

30. R Smith, Chemical Process design and Integration, 2nd edition, McGraw Hill, 2005

31. http://www.chemengonline.com/pci-home [Accessed 15 February 2018]

32. https://www.methanex.com/our-business/pricing [Accessed 15 February 2018]

33. https://www.alibaba.com/showroom/used-cooking-oil.html [Accessed 15 February 2018]

34. https://www.eia.gov/dnav/pet/pet_pri_wfr_a_EPLLPA_PRS_dpgal_w.html [Accessed 15 February 2018]

35. https://www.afdc.energy.gov/fuels/prices.html [Accessed 15 February 2018]

36. https://www.alibaba.com/showroom/price-of-glycerol.html [Accessed 15 February 2018]

37. A Boulamanti, J Moya, Production costs of chemical industry in the EU and other countries: Ammonia, methanol and light olefins, Renewable and Sustainable Energy Reviews 2017,68:1205–1212. https://doi.org/10.1016/j.rser.2016.02.021

38. GD Ulrich, PT Vasudevan, How to estimate utility costs, Chemical Engineering, 2006, 66-69

39. https://www.eia.gov/electricity/data/state/ [Accessed 15 February 2018]

40. https://www.eia.gov/dnav/ng/ng_pri_sum_dcu_nus_m.htm [Accessed 15 February 2018]

41. DE Garrett, Chemical Engineering Economics, Springer, 1989.

42. Petroleum Refining Technology and Economics, James H. Gary & Glenn E., Handwerk, 5th ed., Marcel Dekker, 1994

43. https://www.landandfarm.com/search/Missouri/Industrial-Land-for-sale/ [Accessed 15 February 2018]

44. Y. Zhang, M.A. Dube, D.D. McLean, M. Kates, Biodiesel production from waste cooking oil: 2 Economic assessment and sensitivity analysis, Bioresource technology 2003, 90:229-240. https://doi.org/10.1016/S0960-8524(03)00150-0

IV. IMPROVING PROCESS SUSTAINABILITY AND PROFITABILITY FOR A LARGE US GRAY IRON FOUNDRY

Prashant Nagapurkar, Shyam Paudel and Joseph D. Smith, PhD.

Missouri University of Science and Technology, Rolla, Missouri, USA

ABSTRACT

Energy savings and sustainability have been an important topic in many industrial processes. Limited energy resources and increasing electricity prices make foundry processes less competitive in today's market. For foundry processes, the energy costs represent 5-7% of total sales. Most of the energy used in a foundry is directly related to melting and heat treatment operations. Integrating heat and power systems in a foundry through waste heat recovery techniques can lead to energy reutilization that improves process sustainability and profitability. The average metal caster has a 2.4% pre-tax operating profit on sales. These thin profit margins are susceptible to fluctuating utility costs and energy inefficiencies. The work presented in this paper is an in-depth energy management analysis using the framework of system dynamics to identify potential energy savings through process optimization and waste heat recovery techniques.

Initially, an energy audit of the gray iron foundry situated in Mapleton, IL was carried out. A system dynamics model of the existing foundry process was developed in Powersim[TM] software which investigates the complex interactions among the major energy intensive variables. This base case model was validated with the actual energy data consumption of a foundry in Mapleton, IL. Based on its results, and literature

review, energy saving recommendations through techniques such as waste heat recovery techniques, installation of variable flow drives on fans, etc. were made which has a potential to reduce the annual energy consumption by nearly 26% or $2.6 Million. An upgraded simulation model incorporating all energy saving recommendations was subsequently developed to evaluate the energy saving benefits. The results of the base case model were compared with the upgraded model to comprehend the annual savings.

1. INTRODUCTION

The metal casting industry supplies finished components to a variety of industries in the manufacturing sector. These industries include automotive, railroad, aerospace, transportation, electronics, plumbing, defense, etc. In 2011, the US metal casting industry exported finished castings valued in excess of $29.45 billion [1]. The average metal caster has a pre-tax operating profit of 2.4% of sales volume. Furthermore, the energy costs of the metal casting industry were approximately 5-7% of sales [2]. These values indicate that the net profit margins are sensitive to any fluctuation in commodity prices and energy usage. Therefore, it is essential to conduct the metal casting process at the optimum energy efficiency levels. Any decrease in energy efficiency of the metal casting process has a detrimental impact on the overall energy usage thereby impeding sustainability and profitability. Also, volatile energy prices and uncertainty concerning the future prices have amplified the focus on energy efficiency issues in the metal casting industry. Due to increased globalization, the manufacturing industries in general are facing stiffer competition forcing them to reduce utility costs in order to stay competitive. Increasing energy efficiency is an imperative need for the future and finding ways to

optimize the energy usage is of paramount significance. Furthermore, the threat of global

warming is closely associated with energy use [3]. Increasing energy efficiency possesses

a potential to decrease the global warming.

Table 1 Profit margin increase of energy savings when energy costs are reduced by 35% [4].

Original profit margin	If plant's energy cost percentage is					
	3%	4%	5%	6%	7%	8%
	And energy costs are reduced by 35%, The profit margin will increase by					
1%	104%	139%	173%	208%	242%	277%
2%	51%	69%	86%	103%	120%	137%
5%	20%	27%	33%	40%	46%	53%
10%	9%	13%	16%	19%	22%	25%
20%	4%	6%	7%	8%	9%	11%
30%	3%	4%	5%	6%	7%	18%

   According to Table 1, if a plant has 2% profit margin initially, its energy costs are

3% of total costs and it accomplishes a 35% energy saving then it has a potential to

increase the profit margin by 104%. The prime assumption of 35% energy savings is not

far-fetched and is achievable by implementing stringent energy saving measures [4]. It

should be noted that worldwide experience has proven that mere improvement of

housekeeping practices like monitoring daily energy usage, switching off energy

equipment when not in use, etc. typically produces 10-15% in energy savings [4]. These

are the proven results of numerous energy audits of Canadian foundries undertaken in

previous years by CANMET (Canada Center for Mineral and Energy Technology) [4].

However, there are many barriers to carry out the energy efficiency measures [5]. In

order to achieve energy savings it is essential to mathematically model the physics of the

melting process and comprehend the complex interaction of the energy intensive variables in the system.

Figure 1 shows the energy cost distribution in a typical foundry. Melting represents more than half of the energy costs. Prime focus of this research work was to address the energy efficiency issues associated with the melting process and its auxiliary processes.
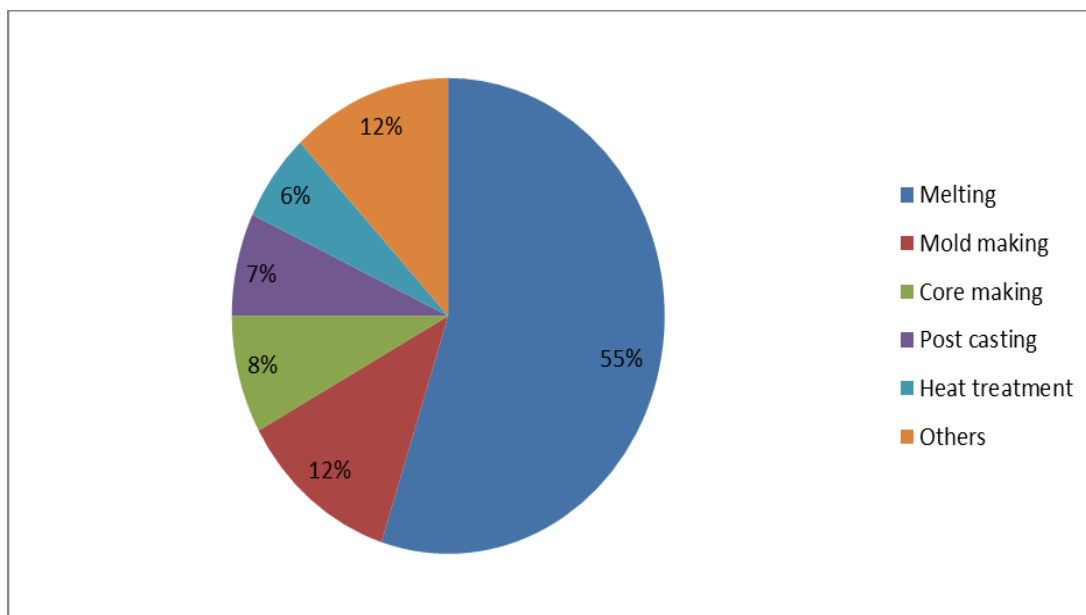
Figure 1 Process energy costs in metal casting [6]

2. METHODOLOGY

2.1. CAUSAL LOOP DIAGRAM

Causal loop diagrams (CLDs) which were developed in the 1960s were primarily used for communication of dynamic simulation models and served an integral part in the system dynamics approach. Development of CLDs is based on the concept that a causal

chain of effects can be tracked through a set of mutually interacting variables which together constitute a dynamic problem. This implies that they present a hypothesis of what would happen if a certain change occurs rather than predicting what will actually take place [7].
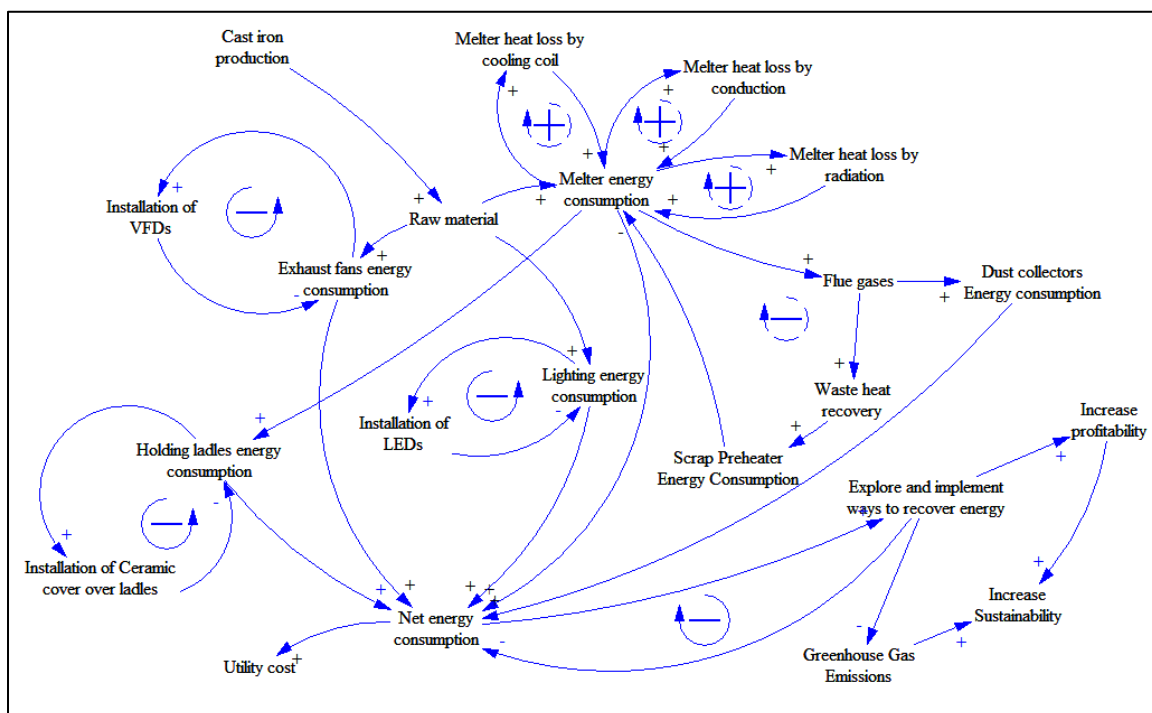
Figure 2 Causal loop diagram of energy intensive variables in the foundry

In the initial part of this research work, specifically step 2, a CLD of the metal casting process encompassing all the energy intensive variables was developed. This diagram was the founding stone for the comprehensive construction of dynamic stock and flow energy model. A detailed study of these interacting variables was carried out at the Mapleton foundry to gain an insight in the energy consumption process. Loops R0, R1 and R2 represent the reinforcing (or positive feedback) loops which denotes that the

increased energy consumption of the induction melter translates into increased energy losses through cooling coils, conduction, radiation respectively. Loops R3, R4, R5, R6, R7 are the balancing loops (or negative feedback) which indicates that the increase in the melter energy consumption will actually decrease the energy requirement by recapturing and recycling the waste energy. These balancing loops are self correcting in a way that they possess a potential to recapture excess melter energy. This research paper precisely addresses these negative feedback loops and attempts to model this foundry process using system dynamics. The ultimate aim of this research work is to make the process more profitable and sustainable by recapturing spent energy. The causal loop diagram shown in Figure 2 is a precursor to the energy flow model that is developed later on Powersim[TM] software.

2.2. SYSTEM DYNAMICS MODEL OF ENERGY CONSUMPTION VARIABLES IN THE FOUNDRY

System dynamics (SD) is an effective tool to tackle temporal behavior of complex interacting systems. SD is a computer simulation tool used to solve complex real-world problems through system feedbacks with a focus to understand actual behavior. SD is based on the concept that our world is made up of stocks, flows and feedback loops and entities in it are connected in intricate patterns [8].

In this paper an effort to use Powersim[TM] to map the energy flow during melting operation in a gray iron foundry. Initially, the metal casting phenomena was mathematically modeled. This mathematical model was then plugged into Powersim[TM] simulation software. In the first phase, a base case model of the existing process of the

Mapleton foundry was developed. In the next phase, this base model was then upgraded

by incorporating all the energy saving recommendations as illustrated in Figure 3. Figure

3 shows a snapshot of the upgraded Powersim^{TM} model. Utmost care has been taken to

match the actual foundry data inputs like melting time in a day, dimensions of melters,

flow rates of the raw metals to melters, ambient temperature, etc to the simulated

mathematical model. These data inputs have been recorded during initial data collection

phase at the foundry.
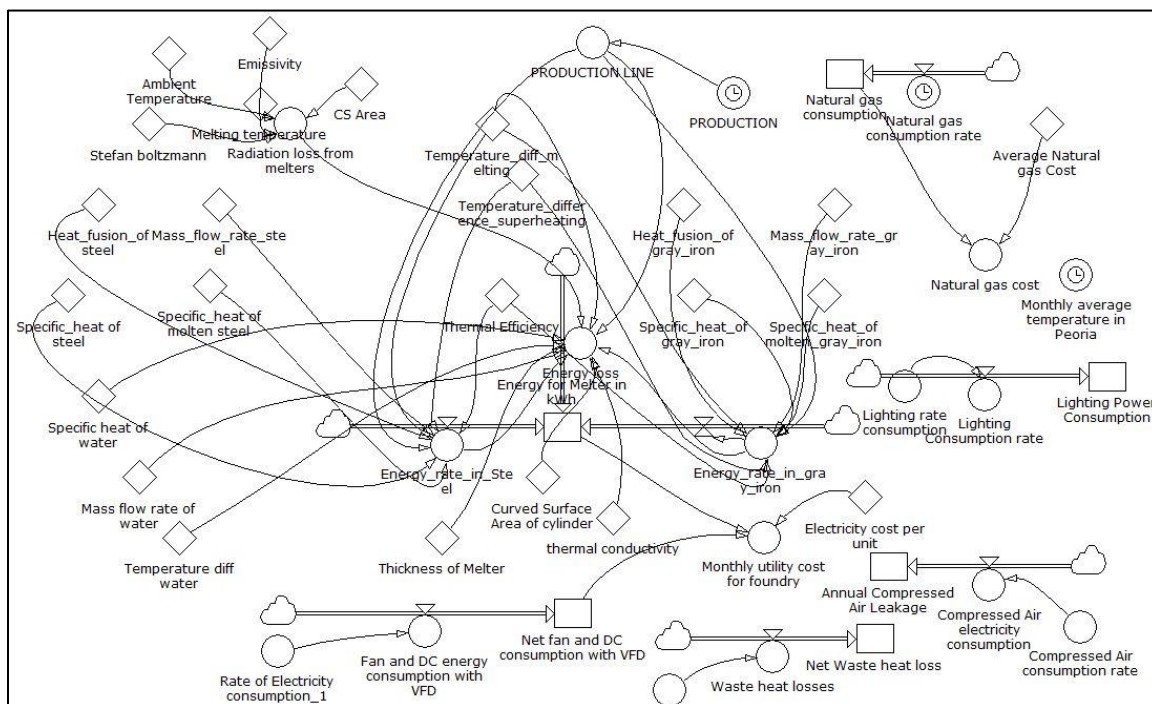
Figure 3 Snapshot of Powersim model of the foundry

2.3. FOUNDRY UNDER STUDY

The analyzed facility is a 30 year old foundry located in Mapleton, Illinois. This

facility occupies 440 acres of land and possesses approximately 20.2 acres of space. This

foundry is one of the largest foundry in the US has an annual capacity of 150,000 tons of finished castings per year. The castings range in size from 7 kg liners to 10,000 kg engine blocks [9].

The melting process at the Mapleton foundry is not a continuous process, but a batch one. The batch process is carried out intermittently only during 6 hours of the day. This intermittent operation imparts the simulation model a dynamic nature. The primary aim of this research work is to identify and recommend ways to Mapleton foundry which can reduce their energy consumption and thereby increase the overall energy efficiency of the facility.

Energy usage data gathered from the foundry indicates that during 2013-14, the melting and its auxiliary processes consumed a net energy of 177.92 GWh in the form of electricity and Natural gas thereby incurring operating expenditures of $10 million on utilities alone.

2.4. MODEL ASSUMPTIONS

All the assumptions are based on the data collected at the foundry. The main assumptions for the development of the models are as follows:

- Two metal constituents are selected for the melting process, namely steel and gray iron with the mass flow rate ratio of 1.26. This is the same ratio that is being used in the Mapleton foundry.

- Melting process is assumed to occur at 2534˚F with subsequent superheating of 176˚F.

- Melting process is carried out only during 6 hours of the day. Specifically, between 1:00 A.M. and 7:00 A.M every day for an entire year.

- The thermal efficiency of the induction melter was assumed to be 70% [6].

- Energy losses such as heat loss through cooling coil, through conduction, radiation and 3% slag loss were considered [6].

- Based on the fan specifications provided by the Mapleton foundry professionals, energy calculations were made for 96 fans and 3 dust collectors separately and inserted into the model. To calculate energy saving with variable flow drives only those fans were considered whose power exceeded 25 HP.

2.5. METHODOLOGY DESCRIPTION

This section describes the step-by-step methodology adopted for dynamic energy systems modelling. A comprehensive dynamic energy model and its analysis has been carried out using the work flow methodology illustrated in Figure 4. The outputs of the model include the annual utility cost incurred to operate the melting section in the plant.

2.5.1. Step 1- Energy Usage Data Collection and Analysis of the Mapleton Foundry. In the first step all the available energy usage data at the facility was collected and analyzed. This data included the energy consumption by the melter, dust collectors as well as the total energy usage by some of the auxiliary equipments in the melting facility. The facility had recorded hourly electrical energy consumed by their melters and their respective dust collectors.

The facility had three induction melters and three dust collectors. For the sake of simulation purposes, all the three induction melters were integrated into one.
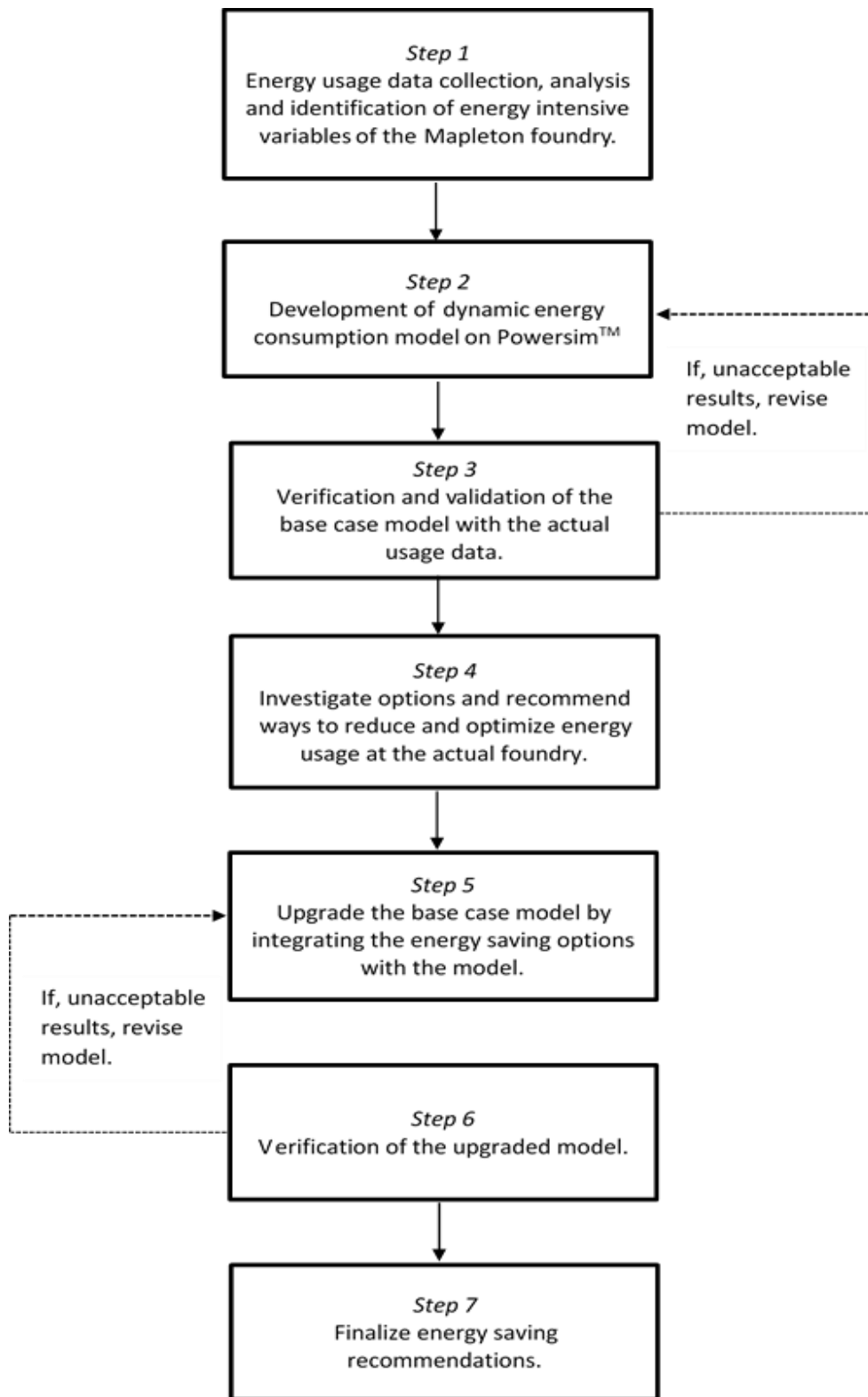
Figure 4 Step by step methodology adopted

The operating time of all the melters was also recorded.

The observations and suggestions of the operators and plant managers were taken into consideration and were incorporated in the simulation so as to make the model a close fit to the actual process.

Based on the analyzed data, energy intensive variables were identified which would be the only variables assumed in the simulation model.

Maximum effort was directed to optimize the energy usage of these variables in the subsequent steps.

2.5.2. Step 2- Development of Dynamic Energy Consumption Model on Powersim. After the identification of key energy intensive variables, the melting process was mathematically modeled and simulated on commercial system dynamic software called Powersim^TM. This model is called as the base case model of the existing Mapleton process.

With the consultation of Mapleton foundry professionals and literature review, maximum effort was directed to create a model of the as-is-process. Care was taken that this base case model would be an accurate representation of the existing process at Mapleton.

2.5.3. Step 3- Validation of the Base Case Model with Actual Data. The simulated model was run for an entire year and the results were compared with the actual energy usage data of the Mapleton foundry's melting facility during the year 2013-14.

The results of the simulation were also discussed and verified with the Mapleton foundry professionals to get an accurate representation of the actual process.

Suggestions from the Mapleton foundry professionals were assimilated into the simulation model by revisiting step 2. Furthermore, the calculated energy consumption was also compared with the data available in the literature. Any inconsistencies, if found, were corrected by modifying the simulation parameters and mathematical equations.

A critical point that needs to be noted that while running a simulation on PowersimTM the mathematical equations and energy flows have to be dimensionally consistent.

The simulation model will fail to converge if the inserted equations are dimensionally incorrect.

2.5.4. Step 4 – Recommend Ways to Reduce and Optimize Energy Usage. With extensive literature review consisting of technical reports issued by government research institutions, [4,6] credible case studies, [4,6,10] energy saving options were explored and evaluated.

This techno-feasibility review was performed with the consultation of Mapleton foundry managers and operators. Energy saving options that were explored and evaluated are as follows:

- Installation of waste heat recovery devices like scrap preheaters, recuperators.

- Installation of ceramic cover for holding ladles.

- Installation of variable flow drives on dust collectors and fans which consume power greater than 25 HP.

- Installation of light emitting diodes (LEDs) in the foundry in place of halogen bulbs.

Conservative estimations on the energy savings were made by exercising above options on the basis of thorough literature review and foundry managers' consultation.

2.5.5. Step 5- Upgrade Base Case Model by Incorporating Energy Saving Options. In this step, the base case model is upgraded by incorporating all the five energy saving options considered in step 4.

Prior to the models upgradation, these recommendations were deliberated with the foundry managers to make the simulation model practically implementable in the future.

The idea behind the development of the upgraded simulation model was to make this model a reality at the Mapleton foundry.

2.5.6. Step 6 -Comparison of Upgraded Model with Literature. The upgraded model was verified and evaluated exhaustively with available literature [4,6,11] to check if it meets the energy saving objectives. The results of the simulations were analyzed to narrow down an optimum and practically attainable solution. The errors, if encountered, were corrected by reverting to step 5 and modifying the simulation constraints and inputs. This step targeted successful convergence and realistic results of the simulation run.

2.5.7. Step 7 - Finalize Upgraded Model and Energy Saving Recommendations. The results obtained in step 6 were discussed with the Mapleton foundry professionals and simultaneously compared with literature review. Subsequently, the energy saving recommendations were finalized. Throughout this process the models were aimed to incorporate an industry oriented as well as a research perspective.

3. RESULTS

For the purpose of this work extensive literature review was carried out to comprehend the iron casting process, technical reports and case studies and to come up with energy saving ways, and eventually model it on Powersim^{TM}. Step 3 of the

workflow methodology (Figure 4) comprises of the validating the base case model with the actual energy usage data of the Mapleton foundry. Figure 5 compares the actual Mapleton foundry during 2013-14, with the estimated data predicted by the base case model. This chart suggests that that there is a mean difference of 15% from the actual values and the predicted ones. This may be due to the fact that for the case of modelling, the foundry is assumed to have an average annual capacity of 150,000 tons, whereas the actual foundry production is fluctuating and exists as a function of orders received. The foundry ramps up the production rate if the casting sales orders are high and decreases the production when the demand is weak.
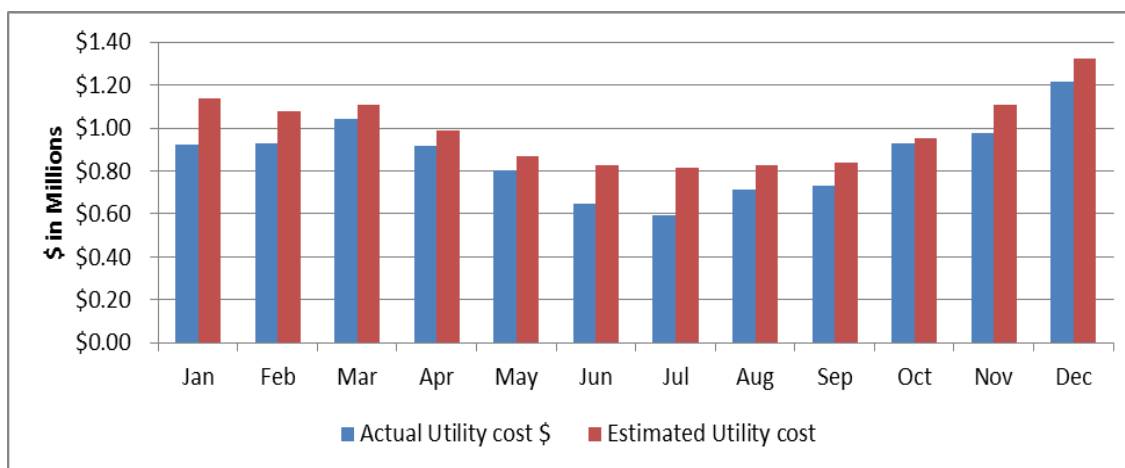
Figure 5 Validation of base case model with the actual energy usage data from Mapleton foundry

The utility costs of the foundry include the electricity usage as well as the Natural gas usage of the facility. The Mapleton foundry uses Natural gas primarily for indoor heating purpose. Therefore, when the ambient temperature is low the Natural gas usage is high, which explains the reason behind high utility costs during October to February.

Analysis of the energy usage data from the foundry also revealed that 71% of annual costs of Natural gas consumption is incurred during the 5 months only (i.e. from November to March). There is a strong dependency of the Natural gas usage with the actual ambient temperatures in Mapleton which the Figure 6 reveals. It specifies the average monthly temperatures in Mapleton during 2013-14. As Peoria, IL is only 12.6 miles away from Mapleton, IL, the temperatures in Peoria were assumed to be equal to the temperatures in Mapleton due to lack temperature data for Mapleton, IL.
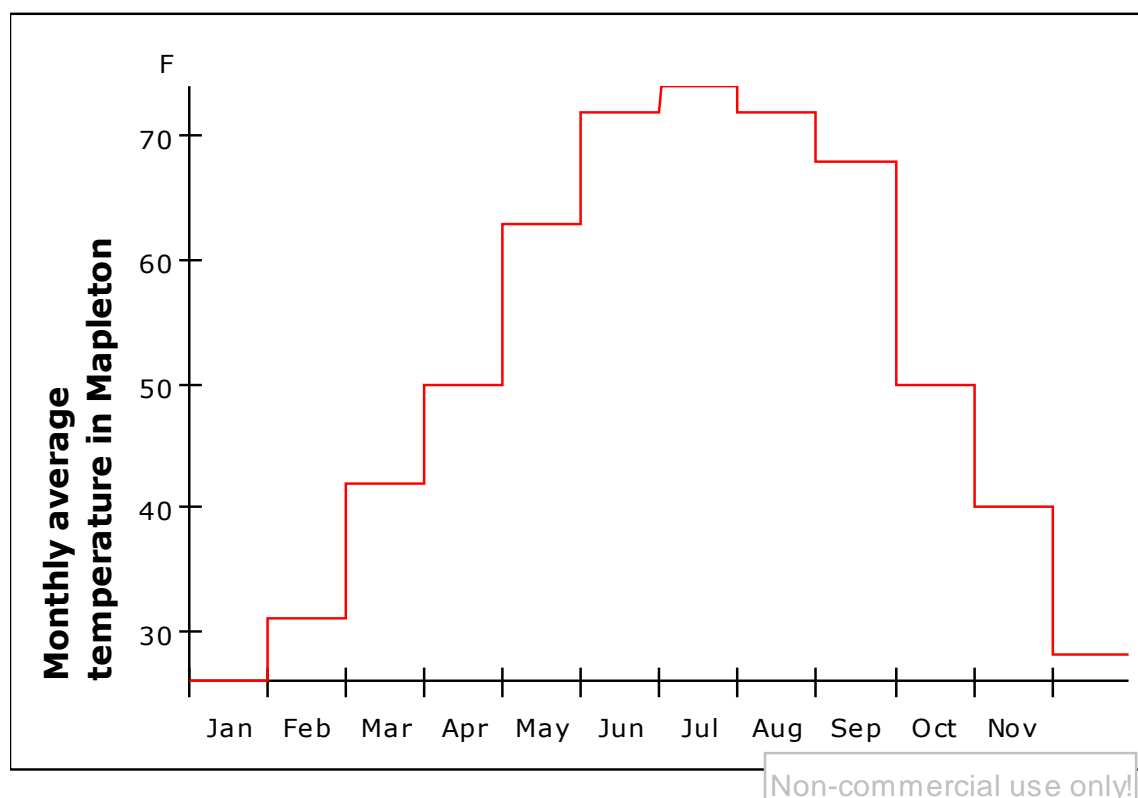
Figure 6 Average Monthly ambient temperatures in Mapleton during 2013-14 [10].
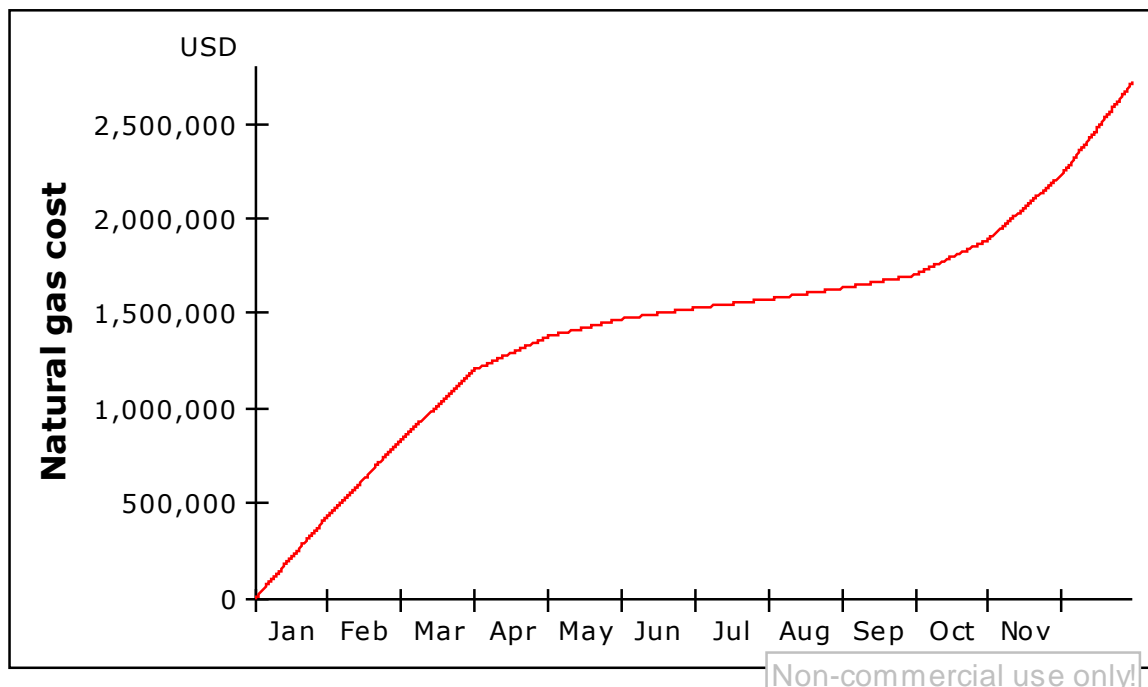
Figure 7 Actual Natural gas usage costs in the foundry during 2013-14.

As shown in Figure 7, the slope of the natural gas cost curve is high at the beginning of the year when the temperatures are around 25^0F and then, subsequently, the curve assumes a flat profile during summer months when the temperature is around 70^0F. Eventually, the Natural gas cost curve reverts back to the higher slopes at the end of year.

This research work revealed that 96 fans and 3 dust collectors were consuming approximately $1.10 Million worth of electrical energy at nominal costs. Actual costs would be much higher taking into account the peak demand costs. According to fan affinity laws, if a fan runs on 60% of its full capacity, it will only consume 22% of the rated HP. This is because fan power consumption is directly proportional to the third power of fan speed. Our detailed analysis also showed that Mapleton foundry has a

potential to reduce these costs by approximately $0.67 million by installing variable flow drives (VFDs) on these fans.

The option of installing variable flow drives on these fans is capital sensitive and therefore in this analysis, VFDs was considered to be installed only for those fans exceeding rated power of 25 HP. 16 exhaust fans and 3 dust collectors were specifically analyzed for this cost saving analysis.

For a medium-sized induction furnace melting iron, the average radiation loss will be equivalent to 10-15 kWh for every minute the cover is open [4]. This melted iron is then poured into holding ladles. Installing ceramic covers on the holding ladles will significantly reduce the radiative losses from the molten iron.

From our estimates, radiative losses worth $0.36 million could be reduced by installing these ceramic covers on holding ladles with a payback period of 6 months.

Table 2 illustrates the problem along with its remedy and its impact in terms of cost. Figure 8 shows the comparison of the base case simulation model with the upgraded model. The upgraded model is the base case model along with the energy saving recommendations implemented in the foundry process.

According to the simulation results, the mean difference between the annual utility cost of the base case model and the upgraded model is 26%, which means by implementing the energy saving recommendations, the Mapleton foundry has a potential to reduce its energy usage by 26%. This indicates a cost saving of nearly $2.6 Million. These recommendations will make the Mapleton foundry process more profitable and sustainable.

Table 2 Energy saving recommendations and their economic impact

#	Problem	Remedy	Impact	Annual savings in $MM	Annual savings in % of utility cost
1.	Compressed air leakage in a foundry	Detect and seal leakage	1. Consistent air pressure, increased service life, reduced maintenance. 2. Reduction in utility costs.	0.65	6.5
2.	Wastage of heat through flue gases.	Installation of recuperators, absorption chillers, regenerators.	1. Can be used to preheat air. 2. Reduction of utility cost, emissions. 3. Improve process efficiency.	0.61	6.1

Table 2 Energy saving recommendations and their economic impact (cont.)

3.	Non heating of metal charge in foundry and waste heat recovery.	Scrap preheater, metal charge preheater.	1. Reduction in melting time, utility cost. 2. Reduction of moisture content of scrap. 3. Improve productivity and process efficiency.	0.53	5.3
4.	Fans, dust collectors constantly operating at full capacity.	Installation of VFDs to control speed of motors.	1. Reduction in utility cost.	0.38	3.8
5.	Radiation energy losses through ladle.	Installation of ceramic cover.	1. Reduction in radiative heat losses, utility cost.	0.36	3.6
6.	High utility costs due to halogen lighting	Install LED lights with sensors.	1. Reduction in utility costs.	0.038	0.38
Total estimated savings				2.568	25.68
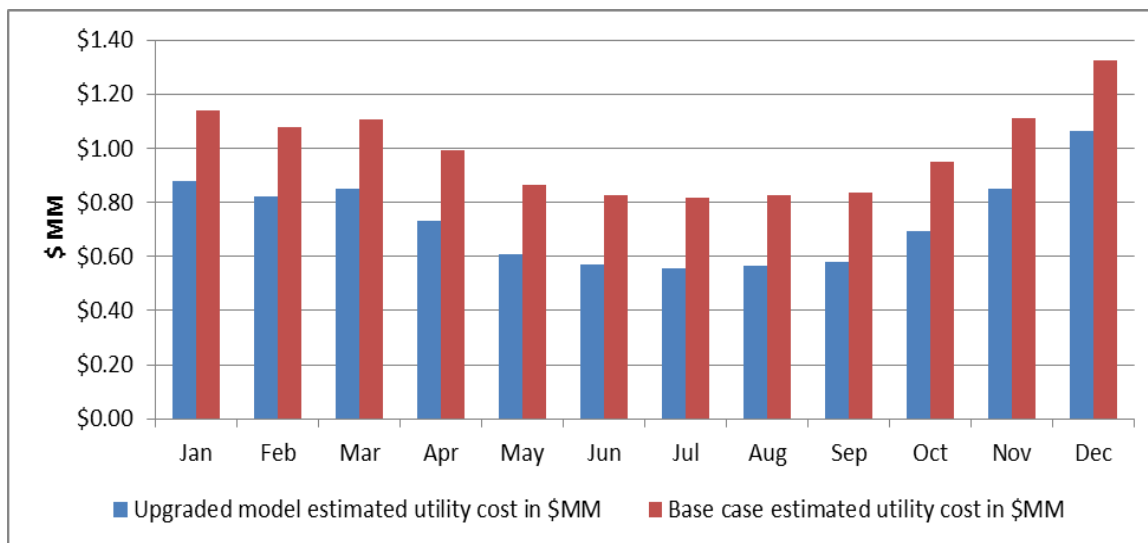
Figure 8 Comparison of base case model with the upgraded model of the Mapleton foundry

4. CONCLUSIONS

The foundry process at Mapleton is a 30 year old process. After careful energy audit and a technical review of the process at the facility, this research work has concluded that it has great potential to reduce and optimize their utility usage. The entire goal of this research work was to make their process more profitable and sustainable. During a technical review of the process, it was found that the fans and dust collectors in the foundry were constantly being operated at 100% capacity, even when the foundry has no production taking place. Furthermore, when the mold making, core making, and sand operations were not in operation, the exhaust fans were running at full capacity. There was no process control existing over the fans and dust collectors. Simultaneously, this research work also explored the Environmental Protection Agency's (EPA) regulations for installing VFDs on dust collectors and fans. This revealed that the EPA does not have any restrictions on the operation capacity of the fans. It has restrictions only on the final

pollutant emissions. EPA does not have the requirement of keeping the fans running at full capacity [12]. Subsequently, installing VFDs on fans and dust collectors will not violate any requirement with the EPA.

ACKNOWLEDGEMENT

REFERENCES

1. American Foundry Society, AFS Metal casting forecast and trends, 2011, pg 5-7.

2. American Foundry Society, Confidential Metal casting Operational Cost Survey, 2005, pg. 1.

3. Intergovernmental Panel on Climate Change, climate change 2007 synthesis report, Robust findings key uncertainties, 2008,6, pg 80-81.

4. Canadian foundry association, Guide to energy efficiency opportunities in Canadian foundries, Setting up an energy management program,2003, 1,pg 8.

5. Nawzad, M.; Roger, K., Energy, Combining optimization and simulation in an energy systems analysis of a Swedish iron foundry, 2012,44,pg 410-419.

6. US Department of Energy-Office of Industrial technologies, Energy and Environmental Profile of the US Metal Casting Industry, Overview, 1999,1, pg-10.

7. Nuno V; Francois S; Filka S; Giorgos K. , Futures, Improving understanding on degrowth pathways: An exploratory study using collaborative causal model,2014,55,58-77.

8. Meadows D.H., System dynamics review, System dynamics meets the press, 1989, 5(1), pg 69-80.

9. http://www.cat.com/en_US/articles/solutions/castings.html. [date accessed: 06.20.2015].

10. http://www.waupacafoundry.com/SiteCollectionDocuments/Sustainability/08171 2-Green%20Heat%20Recovery%20WF%20FINAL-mkt.pdf [date accessed: 06.20.2015].

11. http://www.usclimatedata.com/climate/peoria/illinois/united-states/usil0935 [date accessed: 06.20.2015].

12. US Environmental Protection Agency, 40 CFR art 63, 2008, pg 8-10.

V. AN ASSESSMENT OF THE THREATS TO THE AQUATIC RESOURCES DUE TO RAPID GROWTH IN THE EXTRACTION OF SHALE GAS IN THE USA: AN APPLICATION TO THE KURDISTAN REGION OF IRAQ

Prashant Nagapurkar[a], Joseph D. Smith[a]

[a]Chemical and Biochemical Engineering department, Missouri University of Science and

Technology, Rolla-65401,MO, USA

ABSTRACT

As of 2015 only four countries in the world are producing Shale gas on a commercial scale which are Argentina, China, Canada and the US. Amongst these the production share of US is about 90%. Even though the economic benefits of Shale gas extraction have been substantial for the US, there exists considerably uncertainty in determining its environmental sustainability which is the main motivation behind this work. This effort is accomplished in three steps. In the first step, based on the literature available in the US, a comprehensive assessment of the threats to aquatic resources due to rapid growth in the extraction of Shale gas is carried out. Secondly, to address those identified risks recommendations are proposed to mitigate the adverse impacts. And in the third step, its applicability to Kurdistan region is assessed. Although at present Kurdistan is not producing any Shale gas commercially, the environmental impact studies

conducted in the US will aid the Kurdistan government in shaping the future energy policies pertaining to sustainable Shale gas development.

Keywords—Shale gas; Hydraulic fracturing; Environmental impacts; Greenhouse gas emissions; Water contamination; Iraq.

1. INTRODUCTION

Iraq holds the second position among the Organization of Petroleum Countries' in producing oil and possesses the world's fifth largest proved crude oil reserves. Natural gas reserves in the province of Kurdistan, which is situated in the northern region of Iraq amounts to 112 trillion cubic feet (tcf) [1].

The human race is witnessing a soaring energy demand to fulfill its day to day needs. Global energy demand is expected to rise by 25% through 2040 with oil, natural gas and coal together satisfying 80% of that demand. Natural gas owing to its lower emissions than coal in generating electricity, is considered as a "transition or bridge fuel" indicating that it will serve as a bridge to transition from fossil fuel energy sources to renewable sources. Due to abundance in the supply of Natural gas, from 2014 to 2040 the global demand for natural gas is estimated to rise by 50%, more than twice as fast as oil, with the unconventional gas sources accounting for nearly 90% of North America's gas production [2]. Natural gas can be classified into two types - conventional gas and unconventional gas depending on their source of extraction. Conventional natural gas is typically found in highly permeable rock formations such as sandstone and can be

extracted via traditional drilling methods such as vertical drilling, while unconventional gas is found in low permeable rock formations such as Shale and can be extracted via modern technology drilling methods such as horizontal drilling and hydraulic fracturing.
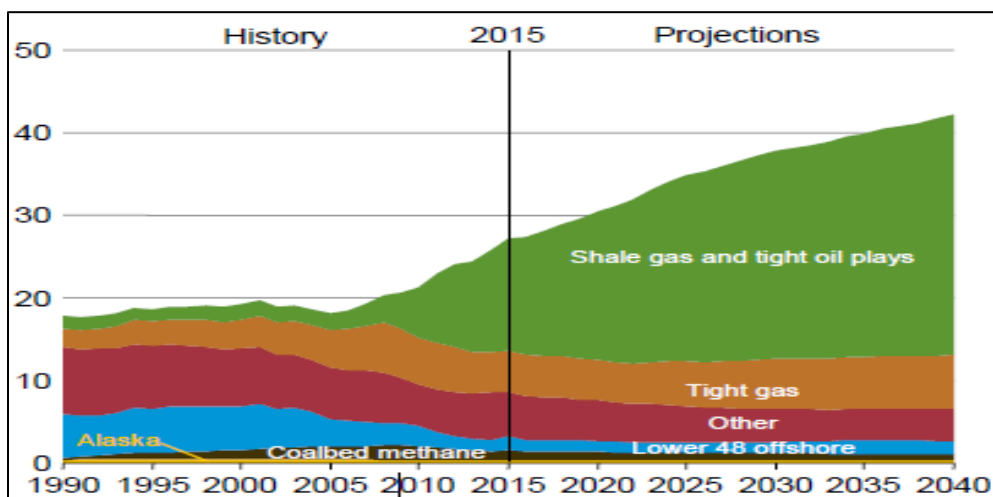
Figure 1 Annual US natural gas production by source in tcf from 1990-2040

Shale gas, tight gas and coal bed methane are three most important sources of unconventional gas in the US. Shale is a fine grained sedimentary rock comprised of a compressed structure of silt and clay size mineral particles. The organic material trapped inside the pores of the Shale rock is known as 'Shale oil or shale gas'. Owing to the recent technological advances due to horizontal drilling and hydraulic fracturing, it is now economically feasible to recover natural gas from low permeability geological formations composed of shale, sandstone and carbonate (limestone). Even though to drill a horizontal shale well is 2-3 times more expensive than a conventional vertical well, the extraction of natural gas from a horizontal well makes a strong economic case because its initial gas production is 3-4 times higher than a conventional vertical well [3]. Due to the

abundance and economic feasibility of unconventional Shale gas it is now expected to play an important role in fueling tomorrow's energy needs.
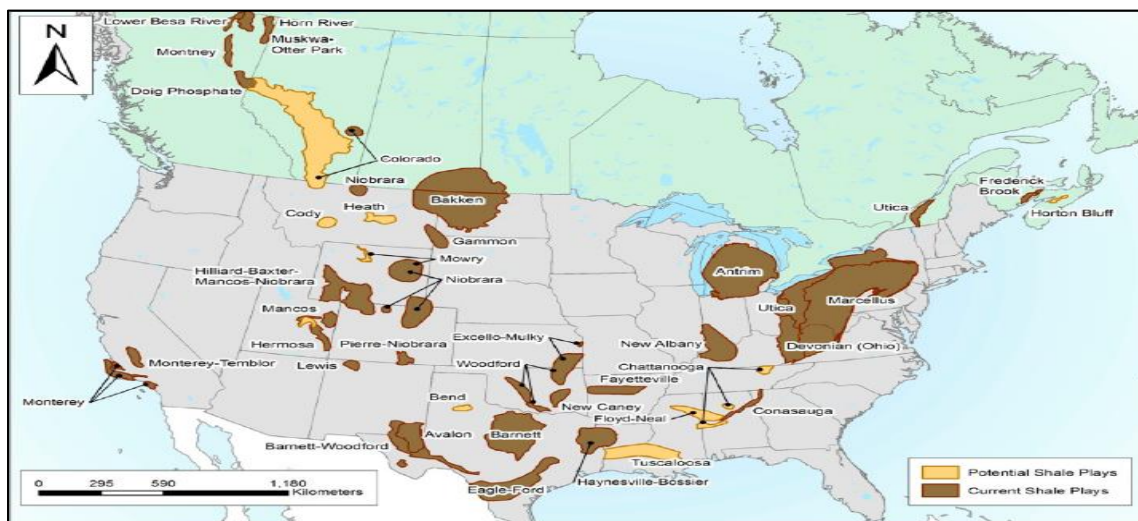
Figure 2 Distribution of Shale resources across the US and Canada [5]

In 2015, the production of natural gas from Shale rock deposits accounted for more than half of the total dry natural gas produced in the US. By 2040, this quantity is projected to double from 13 to 29 tcf per year as illustrated in Figure 1. On a global scale, the natural gas production from shale deposits is estimated to quadruple from 15 to 61 tcf per year, thereby accounting for 30% of the total natural gas generated by 2040 [1].

Figure 2 illustrates the distribution of unconventional Shale plays across the US and Canada indicating that unconventional shale plays are unevenly distributed across the US terrain. In 2015, bulk of the Natural gas in the US was produced from Marcellus Shale (38%), Eagle ford (13%), Barnett (10%) and Haynesville (10%) while the rest contributing the remaining 29% of natural gas produced [4].

1.1. HYDRAULIC FRACTURING BASICS

Hydraulic fracturing is a well stimulation technique in which, the flow of natural gas is enhanced by cracking or fracturing the shale rock by injecting large quantities of fluids at high pressure down a wellbore. In the first step, a horizontal well is drilled below the land surface in the shale rock zone. Then, in the second step, fissures are created in shale formations with the help of fracturing fluids with an intent to increase the permeability of shale rock thereby facilitating the passage of natural gas. Typically, hydraulic fracturing fluids are composed of water (90%), sand (9%), and chemical additives (1%) [6]. The role of water in this process is to primarily enlarge the cracks within the shale formation, while the sand holds open the newly formed cracks to enable the flow of oil and gas trapped within the sediments. In the final step, natural gas or oil is recovered from these wells along with "flowback" or "produced water" which consists of injected chemicals and naturally occurring materials which are found below the earth's surface such as brines, metals and radionuclides [7].

2. ECONOMIC AND SOCIAL IMPACT

The rapid development of unconventional Shale gas resources has generated more than half a million jobs (equivalent to 0.38% of total US labor force) in the US and its contribution to the Gross Development Product (GDP) was more than US $76 billion (equivalent to 0.5% of total US GDP) in 2010.

In addition, Shale gas production has generated over US$18 billion in federal and tax revenues (equivalent to 0.4% of total tax revenue) for the US in 2010 as shown in Table 1 [8]. One study also found that, on an average in Marcellus shale play, land

owners receive $5000 per acre along with royalties amounting to 12-20% of income

generated by the wells [9].These statistics together suggest that the economic and social

impact of the Shale gas production to the US has been significant.

Table 1 Economic and employment contributions of Shale gas production to US economy in 2010 [8]

Contributing factor	Direct	Indirect	Induced	Total
Employment (No. of Jobs)	148 143	193 710	259 494	601 347
GDP (in billion US$)	29.18	22.28	25.28	76.74
Tax revenue (in billion US$)	9.62 [a]	8.82 [b]	0.16 [c]	18.6
[a] – Federal tax revenue, [b] – State and local tax revenue, [c] – Federal royalties				

3. ENVIRONMENTAL IMPACT

Although there are significant economic benefits due to the Shale gas

development in the US, there are several health and environmental concerns associated

with it. Specifically, concerns relating to air pollution, greenhouse gas emissions (GHG),

radiations, and ground-water and surface-water contamination [10-12]. Depending on

their medium of transmission, the environmental impacts are broadly classified into two

categories namely, impact due to air and water emissions.

3.1. IMPACT DUE TO AIR EMISSIONS

A study found that, for an average Shale gas well, there exists a net methane loss of 3.6-7.9% of the total natural gas produced from that well. Methane loss estimates in this study were attributed to well completion, venting, improper installation of equipments, storage, processing, transportation and distribution. These estimates are almost twice as great as those of conventional gas emissions which are in the range of 1.7- 6%. Finally the study concludes that the GHG emissions for Shale gas per mega joule (MJ) of fuel produced are 33% higher, while for coal, the emissions are 24% higher than the conventional Natural gas for a 20 year horizon. Even after taking into account the efficiency of electricity production, GHG footprint of Shale gas exceeds coal over its complete life cycle [10]. However, another study carried out at Argonne National Laboratory concluded that for the same basis of per MJ of fuel produced for a 20 year horizon, Shale gas has 12% lower while coal has 13% higher GHG emissions than conventional Natural gas [13]. These contrasting results indicate that there is considerable variation in computing the GHG emissions associated with unconventional Shale gas development. This variation is mainly attributed to GHG emitted during natural gas extraction. Apart from the GHG emissions, various pollutants such as volatile organic compounds (VOCs), Nitrogen oxides (NOx), alkanes, alkenes, and silica particles also get emitted during Shale gas extraction [10-12].

3.2. IMPACT DUE TO WATER EMISSIONS

In 2010, according to the United States Geological Survey (USGS) agency, the US used about 355,000 million gallons of water per day out of which, water withdrawn

from freshwater sources amounted to 86% while the rest was withdrawn from saline

sources. 51% of the total fresh surface water was utilized for thermoelectric power

generation while 29% was used for irrigation purposes [14]. For Shale gas, when

compared with other fuel sources like conventional natural gas, conventional oil, coal, oil

sands, biomass and uranium, the water footprint and the water intensity (ratio of net water

consumption to net energy recovery) is low [15-17]. Although the water footprint of

Shale gas is low on a relative scale, its extraction consumes significant amount of

resources on an absolute scale. For instance, on an average, drilling a well situated in

Marcellus Shale play consumes about 80,000 gallons of water, while hydraulically

fracturing it needs another 3.8 million gallons. According to a study conducted by

National Energy Technology Laboratory (NETL) in 2009, the drilling and hydraulic

fracturing operations in the Barnett Shale, Fayetteville Shale and Haynesville Shale

consume about 2.7, 3.06 and 3.7 million gallons of water respectively [18]. The water

resource impacts due to Shale gas development are also substantial and have widely been

studied by scientific community and also has been a major focus by the media [19-21].

Despite the fracking industry's economic benefits, the media's negative portrayal of

fracking is mainly due to its impact to the water resources in the surrounding areas of

Shale gas development due to radiation, groundwater and surface water contamination

[10-12]. Together, these constitute some of the main reasons for public opposition to

Shale gas development and is the motivation behind the effort carried out in this work.

4. RESULTS AND MAIN CONTRIBUTION

The commercial extraction of Shale gas through hydraulic fracturing and

horizontal drilling is a relatively new technique. Therefore, earliest of its studies

concerning environmental impacts to local communities date back to 2009. As of 2015 currently only four countries in the world are producing Shale gas on a commercial scale. These are Argentina, China, Canada and the US, with the latter producing approximately 90% of total share. Consequently, most of the environmental impact studies have been conducted mostly in the US. Even though for the case of US, the economic benefits of Shale gas extraction have been substantial, there exists considerably uncertainty in determining its environmental sustainability which is the main motivation behind this work. The work outlined in this manuscript is carried out in three steps as mentioned below.

4.1. COMPREHENSIVE AND CRITICAL REVIEW OF THE LITERATURE FOCUSING ON ASSESSING RISKS TO WATER RESOURCES DUE TO SHALE GAS DEVELOPMENT IN THE US

In this section, a review of water resource degradation through the following pathways along with their key results are considered.

4.1.1. Contamination of Shallow Aquifers Due to Fugitive Natural Gas Emissions, Brines and Hydraulic Fracturing Fluids. The leakage of natural gas in a well could be attributed to leakage around casings or well annulus, abandoned wells, along artificially generated fractures, or adjacent stratigraphic formations.

Methane formed beneath the earth's surface are of two types – thermogenic and biogenic. Breakdown of large organic molecules results in the creation of thermogenic methane, while the biogenic methane is generated as a consequence of metabolic activity of methanogenic microorganisms under anoxic conditions [22].

Biogenic and thermogenic methane gases have unique stable hydrogen and carbon isotope compositions and can be distinguished from each other using gas identification and geochemical finger printing methods. Additionally, the source of these gases could also be ascertained by determining the quantity of methane gas to other hydrocarbon gases (for instance C1/C2 ratios) [23-25].

The analytical methods used to determine the isotopic composition are IRMS (Isotope ratio mass spectrometry) and GC-IRMS (Gas Chromatography - Isotope ratio mass spectrometry) [26].

Some studies referenced in this paper found traces of thermogenic methane in the shallow aquifers located in Appalachian basin in Pennsylvania [27,28]. By using analytical methods such as stable isotope fingerprinting, molecular hydrogen ratios and noble gas data, stray gas composition, source of methane gas (rock formations) can be successfully determined. This paper, after reviewing evidence hypothesizes that groundwater contamination could occur due to the following pathways:

- Stray methane gas could have leaked through faulty casings or improper installations of equipment in the vicinity of hydraulically fractured wells [28,29].

- As a result of natural processes facilitated by natural conduits, methane could have diffused to the shallow aquifers through geologic time extending from intermediate formations (and not shale formations) to the aquifers [30].

- The flow of saline water (present in deep saline formations) and fracturing fluids to the shallow aquifers could result in contamination. However, due to insufficient evidence, this cause could not be accurately established [28,29].

- Naturally occurring microorganisms existing in the soil in the presence of stray methane gas could initiate reactions that could liberate elements like Arsenic, Manganese and Iron from the surrounding areas of aquifers [31].

- Within the aquifers in the presence of halogen atoms (Cl,Br or I) and the organic matter (stray gas methane), there is a possibility that toxic trihalomethanes could get formed paving the way towards groundwater contamination [32].

- The fractures induced to hydraulic fracturing could provide conductive pathway for the migration of formation brines or fracturing fluids [33]. This mechanism is under a lot of dispute with some studies supporting it [33] while others refuting it [34,35] owing to some deterring factors such as low permeability of Shale rock formations and steep hydraulic gradients. Despite these factors, there exists some studies which suggests evidence that fluid has migrated from deep water saline formations (situated in rock formations below shale formations) to shallow water formations [36-38].

Thus, the likelihood of methane migration not only depends on improper installation of well equipments but also the topography of the subsurface rock formations.

4.1.2. Contamination of Surface Water Due to Improperly Treated Wastewater, Hydraulic Fracturing Fluids, Stray Gas Leaks and Spills. As stated earlier, hydraulic fracturing fluids are typically composed of water (90%), sand (9%), and chemical additives (1%).

Table 2 Functions and hazards of chemicals used during hydraulic fracturing

Hydraulic fracturing chemical	Function	Hazard
Hydrochloric acid	Dissolve minerals and instigate rock fracture	Toxic and corrosive
Polyacrylamide	Friction reducer	Toxic
Ethylene glycol	Friction reducer	Carcinogenic and toxic
Ammonium persulfate	Viscosity reducer	Toxic and strong oxidizing agent
Sodium chloride	Prevent clay swelling and adjourn the fluid breakdown process	Irritant
Methanol	Protect the pipe from corrosion and friction reducer	Flammable and toxic
Formic acid	Protects the pipe from corrosion	Flammable and corrosive
Glutaraldehyde	Biocide	Toxic and corrosive
Quaternary ammonium chloride	Biocide	Corrosive

The chemical constituents in these fluids are toxic and carcinogenic and therefore pose a health hazard. Table 2 lists some of the chemicals used in along with their function

and health hazard [12]. The entire composition of the fractured fluids prior to well injection, is not revealed by the corporations because, in the US disclosure of this information is voluntary. However, the voluntarily disclosed data is stored in the national chemical registry for fracturing fluids. The registry lists the specific ingredients and their maximum (not exact) concentration in the fracturing fluid for every well in every county and state across the US [39]. Although some information regarding the composition of chemicals is revealed, the well operators do not disclose information regarding the patented chemicals used during hydraulic fracturing, citing this information as proprietary information [40]. The fluids in a hydraulically fractured well are categorized into two types – flowback waters and produced waters. Flowback waters are the fluids that come back to the surface after the completion of hydraulic fracturing process while produced waters are the fluids that get extracted during the natural gas production.

Flowback waters are typically composed of injected hydraulic fracturing chemicals and shale rock formation brines. Produced waters contain all the components existing in the flowback waters, along with the toxic elements such as barium, strontium, and radioactive radium found below the surface of the earth [41-43]. Due to the presence of these toxic elements and injected chemicals, there are three possible modes of surface water contamination and their impacts. These are as follows:

- According to one study, spills and leakages of flowback and produced waters occur in the vicinity of drilling sites, and the frequency of reported violations per shale gas well increases two fold in the highly dense drilling areas [44]. Another study revealed that these spills not only result in the increase of concentrations of organic compounds like benzene, toluene, xylene in the

surface water but also result in the increase of concentration of salts (Cl,Br),

alkaline earth metals (Ba, Sr), metalloids (Se, As)and radionuclides (Ra) [45].

- An experimental study concluded that discharge of untreated hydraulic fracking

  fluids to Acorn Creek in Kentucky, US caused distress to aquatic species

  residing in the creek and finally resulting in its depletion [46].

- The analysis of effluent streams from waste water treatment facilities in

  Pennsylvania suggested that certain parameters such as high total dissolved

  solids (TDS), low SO_4/Cl ratio and distinctive Br/Cl, $^{228}Ra/^{226}Ra$, $^{87}Sr/^{86}Sr$

  showed resemblance to Marcellus Shale characteristics indicating the

  ineffectiveness of treatment plants in handling effluent streams originating from

  shale gas drilling sites [47].

4.1.3. Buildup of Metals, Radioactive Materials on Sediments of Water

Bodies. The analysis of the stream sediments downstream to waste treatment facilities

indicated high ratios of 228Ra/226Ra characteristic to Marcellus brines which failed to

meet regulatory standards for a licensed radioactive facility [47].

High amounts of radioactive materials were also found in the sediments present at

the bottom of the pond as a result of oil spill due to hydraulic fracturing activities [48].

A different study revealed that the sludge from reserve pits (active and vacated

pits) of hydraulic fracturing fluids showed elevated amounts of radionuclides such as

228Ra, 226Ra, 208Tl, 214Pb, 214Bi, 210Pb.

The total beta radiation from those radionuclides exceeded the regulatory

guidelines by 8 times [49].

4.2. SOLUTIONS TO MITIGATE RISKS

After stating all the possible threats to water resources due to hydraulic fracturing activities, some steps could be taken to minimize the risks. The possible solutions to minimize water impacts are as follows:

- Incorporate mandatory baseline monitoring of water resources using advanced geochemical fingerprinting techniques to determine accurate chemical and isotopic compositions. This data should be accessible to citizens.

- There exists evidence for migration of stray gas to water well situated at a distance of less than 0.6 miles [28,29]. The likelihood of contamination risk could be minimized by creating regulations that could prohibit companies from drilling within half a mi le of drinking water wells.

- Accurate composition of the chemicals used in hydraulic fracturing should be disclosed by the companies. This data should be available to the general public.

- Currently, the Clean Water Act of 2005 exempts drilling sites in the vicinity of aquifers from any regulation. This exemption should be revoked as hydraulic fracturing contain toxic and carcinogenic compounds.

- Waste water management strategies such as zero discharge and recycling of fracturing fluids should be adopted to reduce environmental impact of these fluids. A study showed that the experimental blending of Marcellus flowback waters with acid mine discharge could reduce the concentration of contaminants present in each of them [50].

- Presently, waste water treatment technologies such as chemical precipitation and water filtration by means of thermal distillation are deployed to treat

sewage exiting from drill sites [51,52]. However, these technologies fail to eliminate halogens such as chloride and bromide resulting into the formation of toxic trihalomethanes. New technologies should be adopted to address this gaps.

4.3. APPLICABILITY TO KURDISTAN REGION OF IRAQ

- The US Geological Survey recently assessed the potential for unconventional oil and gas resources within the Jurassic Sargelu formation of Iraq (located in central region of Iraq). According to their estimates, the formation holds 1,606 million barrels of oil and 0.96 tcf of Natural gas indicating immense potential for future commercialization [53].

- Although at present Kurdistan is not producing any Shale gas commercially, the environmental impact studies conducted in the US will aid the Kurdistan government in shaping the energy policies of the future pertaining to sustainable Shale gas development.

REFERENCES

1. US Energy Information Administration, Annual Energy Outlook 2016, 2016

2. Exxonmobil, The Outlook of Energy:A view to 2040, 2016

3. Engelder, T., Lash, G.G., Marcellus Shale play's vast resource potential creating stir in Appalachia, The American Oil and Gas Reporter, 2008

4. https://www.eia.gov/energy_in_brief/article/shale_in_the_united_states.cfm [accessed 12 November 2016]

5. US Energy Information Administration, Annual Energy Outlook 2013, 2013

6. Daniel A., Bohm B., Coughlin B.J., Layne M., Evaluating Implications of Hydraulic Fracturing in Shale gas reservoirs, SPE Americas E&P Environmental safety conference, 2009, San Antonio, TX, USA

7. https://www.epa.gov/hydraulicfracturing/process-hydraulic-fracturing [accessed 12 November 2016]

8. R.F. Fullenbaum, J.W. Larson, J. Dorsey, The economic and employment contributions of Shale gas in the US, HIS Global Insight, Washington DC, 2011

9. Collier, C.R. Potential impact of Marcellus Shale Drilling on Water resources in the Delaware, Presentations of American Water Resources Associations, Philadelphia Metropolitan Area, 2009.

10. Howarth, R., Santoro, R., Ingraffea, A, Methane and the greenhouse-gas footprint of natural gas from shale formations Climate Change 2011, vol. 106 (4), 2011, pp. 679−690.

11. Howarth, R. W.; Ingraffea, A.; Engelder, T. Natural gas: Should fracking stop? Nature 2011, 477 (7364), 271−275

12. Cooper J., Stamford L., Azapagic A., Shale gas: A review of the economic, environmental, and social sustainability, Energy Technology, 2016,4, 772-792

13. Burnham A.,Han J.,Clark C., Wang M., Dunn J.,Paulo-Rivera I., Life cycle greenhouse emissions of Shale gas, Natural Gas, Coal and Petroleum, Environmental Science Technology, vol. 46, 2012, pp. 619-627.

14. http://water.usgs.gov/edu/wateruse-total.html [accessed 11/30/2016]

15. Laurenzi I., Jersey G., Life cycle greenhouse gas emissions and freshwater consumption of Marcellus Shale gas, Environmental Science Technology, 2013

16. Clark, C., Horner, R., Harto, C., Life cycle water consumption for shale gas and conventional natural gas, Environmental Science Technology, 2013,47, 11829-11836

17. Mekonnen, M., Gerbens-Leenes, P.W., Hoekstra, A., The consumptive footprint of electricity and heat: a global assessment, Environmental Science: Water Resource Technology, 2015, 1, 285

18. Modern Shale Gas Development in the United States: A Primer Technical Report, US Department of Energy, National Energy Technology Laboratory, 2009, Washington, DC

19. http://www.independent.ie/irish-news/news/ban-on-fracking-expected-to-be-extended-after-reports-revealed-major-environmental-risks-35257419.html [accessed 11/30/16]

20. http://www.vice.com/read/standing-rock-fort-berthold-how-oil-can-transform-and-damage-native-reservations [accessed 11/30/16]

21. http://breakingenergy.com/2016/11/08/the-negative-impacts-of-restricting-fracking/ [accessed 11/30/16]

22. Wuebbles, D.J., Hayhoe, K., Atmospheric methane and global change, Earth-Science Reviews, 2002, 57, 177-210

23. Schoell, M., Genetic characterization of natural gases, AAPG Bulletin, 1983, 67, 2225-2238

24. Whiticar, M.J., Faber, E., Schoell, M., Biogenic methane formation in marine and freshwater environments: CO_2 reduction vs acetate fermentation—Isotope evidence, Geochimica et Cosmochimica Acta, 1986, 50, 693-709.

25. Chung, H., Gormly, J., Squires, R., Origin of gaseous hydrocarbons in subsurface environments: Theoretical considerations of carbon isotope distribution, Chemical Geology, 1988, 71, 97-104.

26. Ferrer I., Thurman M., Advanced Techniques in Gas Chromatography- Mass Spectrometry (GC-MS-MS and GC-TOF-MS) for Environmental Chemistry,2013, 61, 355-356.

27. Osborn, S. G.; Vengosh, A.; Warner, N. R.; Jackson, R. B. Methane contamination of drinking water accompanying gas-well drilling and hydraulic fracturing, Proceedings of National Academy of Sciences of USA, 2011, 108 (37).

28. Jackson, R. B.; Vengosh, A.; Darrah, T. H.; Warner, N. R.; Down, A.; Poreda, R. J.; Osborn, S. G.; Zhao, K.; Karr, J. D. Increased stray gas abundance in a subset of drinking water wells near Marcellus shale gas extraction. Proc. Natl. Acad. Sci. US.A. 2013, 110 (28), 11250−11255.

29. Osborn, S. G.; Vengosh, A.; Warner, N. R.; Jackson, R. B. Methane contamination of drinking water accompanying gas-well drilling and hydraulic fracturing. Proc. Natl. Acad. Sci. U. S. A. 2011, 108, 8172−8176.

30. Rowe, D.; Muehlenbachs, K. Isotopic fingerprints of shallow gases in the Western Canadian sedimentary basin: tools for remediation of leaking heavy oil wells. Org. Geochem. 1999, 30 (8A), 861−871.

31. Van Stempvoort, D.; Maathuis, H.; Jaworski, E.; Mayer, B.; Rich, K. Oxidation of fugitive methane in ground water linked to bacterial sulfate reduction. Ground Water. 2005, 43 (2), 187−199.

32. Harkness S., Dwyer G., Warner N., Parker K., Mitch W., Avner V., Iodide , bromide, and ammonium in hydraulic fracturing and oil and gas waste waters: Environmental implications, 2015, Environ Sci. Technol., 49, 1955-1963.

33. Myers, T. Potential contaminant pathways from hydraulically fractured shale to aquifers. Ground Water. 2012, 50 (6), 872−882.

34. Cohen, H. A.; Parratt, T.; Andrews, C. B. Potential contaminant pathways from hydraulically fractured shale to aquifers. Ground Water. 2013, 51 (3), 317−319.

35. Myers, T. Potential contaminant pathways from hydraulically fractured shale to aquifers author's reply. Ground Water. 2013, 51 (3), 319−321.

36. Long, D. T.; Wilson, T. P.; Takacs, M. J.; Rezabek, D. H. Stableisotope geochemistry of saline near-surface ground water: East-central Michigan basin. Geol. Soc. Am. Bull. 1988, 100 (10), 1568−1577.

37. Mehta, S.; Fryar, A. E.; Banner, J. L. Controls on the regional scale salinization of the Ogallala aquifer, Southern High Plains, Texas, USA. Appl. Geochem. 2000, 15 (6), 849−864.

38. Mehta, S.; Fryar, A. E.; Brady, R. M.; Morin, R. H. Modeling regional salinization of the Ogallala aquifer, Southern High Plains, TX, USA. J. Hydrol. 2000, 238 (1−2), 44−64.

39. fracfocus, http://www.fracfocusdata.org/dsiclosuresearch/, [accessed 23 November 2016.

40. S. Gamper, Rabindran, Energy Technology, 2014, 979.

41. Barbot, E.; Vidic, N. S.; Gregory, K. B.; Vidic, R. D. Spatial and temporal correlation of water quality parameters of produced waters from devonian-age shale following hydraulic fracturing. Environ. Sci. Technol. 2013, 47 (6), 2562−2569.

42. Haluszczak, L. O.; Rose, A. W.; Kump, L. R. Geochemical Evaluation of flowback brine from Marcellus gas wells in Pennsylvania, USA. Appl. Geochem. 2013, 28, 55−61.

43. Chapman, E. C.; Capo, R. C.; Stewart, B. W.; Kirby, C. S.; Hammack, R. W.; Schroeder, K. T.; Edenborn, H. M. Geochemical and strontium isotope characterization of produced waters from marcellus shale natural gas extraction. Environ. Sci. Technol. 2012, 46, 6, 3545−3553.

44. Carnegie Museum of Natural History Pennsylvania Unconventional Natural Gas Wells Geodatabase; Pittsburgh, PA: Carnegie Museum of Natural History, 2000−2013.

45. DiGiulio, D. C.; Wilkin, R. T.; Miller, C.; Oberley, G. Investigation of Ground Water Contamination near Pavillion, Wyoming Draft Report, U.S. Environmental Protection Agency, 2011.

46. Papoulias, D. M.; Velasco, A. L. Histopathological analysis of fish from Acorn Fork Creek, Kentucky exposed to hydraulic fracturing fluid releases, Southeastern Naturalist 2013, 12, 90−111.

47. Warner, N. R.; Christie, C. A.; Jackson, R. B.; Vengosh, A. Impacts of shale gas wastewater disposal on water quality in western Pennsylvania. Environ. Sci. Technol. 2013, 47 (20), 11849−11857.

48. Warner, N. R.; Jackson, R. B.; Vengosh, A., Tracing the Legacy of Accidental Spills and Releases of Marcellus Wastewater in Pennsylvania, Geological Society of America: Denver, CO, 27−30 October 2013.

49. Rich, A. L., Crosby, E. C. Analysis of reserve pit sludge from unconventional natural gas hydraulic fracturing and drilling operations for the presence of technologically enhanced naturally occurring radioactive material (TENORM). New Solutions 2013, 23 (1), 117− 135.

50. Kondash, A. J.; Warner, N. R.; Lahav, O.; Vengosh, A. Radium and barium removal through blending hydraulic fracturing fluids with acid mine drainage. Environ. Sci. Technol. 2014, 48 (2), 1334−1342.

51. Veil, J. A. Water Management Technologies Used by Marcellus Shale Gas Producers; prepared for US Department of Energy Office of Fossil Fuel Energy, National Energy Technology Laboratory, 2010.

52. Veil, J. A. White Paper on SPE Summit on Hydraulic Fracturing; Society of Petroleum Engineers: Houston TX, 2011.

53. Schenk, C.J., Pitman, J.K., Charpentier, R.R., Klett, T.R., Gaswirth, S.B., Brownfield, M.E., Leathers, H.M., Mercier, T.J., and Tennyson, M.E., 2015, Assessment of unconventional oil and gas resources in the Jurassic Sargelu Formation of Iraq, 2014: U.S. Geological Survey Fact Sheet 2015–3006.

SECTION

2. OVERALL CONCLUSIONS

Based on the regional electricity load profile and availability of renewable sources, an optimum configuration of a standalone microgrid was determined that had the lowest LCOE using a stochastic optimization algorithm known as GA. The results of the GA for a single home microgrid were verified using a brute force method (ESA) for the case of single home. Scaling up the microgrid size (1 to 10 homes) reduced the LCOE by 7-12% thereby demonstrating the economies of scale effect. Neglecting financial subsidies, the LCOEs were in the range of $0.32 - 0.42 /kWh and were approximately 3.5 - 4.5 times as that of their local retail electricity cost. The environmental footprint of microgrid was found to be extremely low as they were found to be approximately 1/10th as those emitted by an equivalent conventional electric grid.

Artificial Neural Networks were able to successfully predict energy demand of the two US cities, Fargo and Phoenix. The incorporation of carbon taxes barely affected the electricity cost of microgrid ($/kWh) but increased the conventional grid's rate by 7-33% as CO_2 emissions of microgrid were observed to be 5 times as that of conventional grid.

Techno-economic analysis of supercritical biodiesel production from waste cooking oil with co-solvent was successfully conducted which revealed the supercritical process as a profitable venture with a payback period of 2.3 years and 0.5 years for 10,600 ton and 128,000 ton plant capacity respectively. The breakeven cost was also determined to be $2.47 and $1.33 for a gallon of diesel respectively deeming the process

to be profitable venture at the current biodiesel price of $3.38 per gallon. This analysis proved the ability of the supercritical biodiesel production process to thrive even when the purchase price of WCO increased or decreased by 50%.

A system dynamics model of the existing foundry process was developed using Powersim software which investigated complex interactions among the energy intensive variables. This base case model of the process was validated with the actual energy data consumption procured from a foundry located in Mapleton, IL. An upgraded model was also developed that incorporated all the proposed energy saving recommendations such as waste heat recovery techniques, installation of variable flow drives on fans, etc. The upgraded model revealed that the foundry had a potential to reduce its annual energy consumption by nearly 26% or $2.6 Million.

A comprehensive assessment and review of the threats to aquatic resources due to rapid growth in the extraction of Shale gas was carried out based on actual development in the US. Furthermore, its future applicability to Kurdistan region of Iraq was also evaluated which could aid researchers and local policy makers in shaping the energy policies pertaining to sustainable Shale gas development.

VITA

Prashant Suresh Nagapurkar attained his bachelor's degree in Chemical Engineering in 2011 from University of Pune, India. During his undergraduate education, he pursued an internship at National Chemical Laboratory where he was involved in generating value added chemicals from agricultural waste (sugarcane bagasse). This experience sparked his interest in sustainable energy as a result of which he started working as a Process Engineer in Praj Industries where he was designing and developing innovative technologies related to production of bioethanol.

With a professional objective of forging a career in the domain of sustainable energy, Mr. Nagapurkar embarked on a quest to attain a Masters degree in Chemical Engineering at Missouri S&T in the fall of 2013. Consequently, he ended up working with Dr. Joseph Smith as his interests aligned well with Dr. Smith's research areas. Mr. Nagapurkar completed his Masters degree in 2015 and enrolled in the doctoral program at Missouri S&T.

While pursuing his doctoral degree in Chemical Engineering, Mr. Nagapurkar pursued an internship in the Materials and Corrosion department at Shell in 2016. He also served as a tutor for undergraduate and graduate courses in the Chemical Engineering department at Missouri S&T. Mr. Nagapurkar received his doctorate degree in Chemical Engineering from Missouri University of Science and Technology in May 2019.